SEISMIC PERFORMANCE ASSESSMENT OF DUCTILE REINFORCED CONCRETE BLOCK STRUCTURAL WALLS

SEISMIC PERFORMANCE ASSESSMENT OF DUCTILE REINFORCED CONCRETE BLOCK STRUCTURAL WALLS

By

MUSTAFA ABDEL-MAGID MOHAMMED SIYAM

B. Eng. & Mgmt.

A Thesis Submitted to the School of Graduate Studies in Partial Fulfillment of the Requirements for the Degree of Doctorate of Philosophy

McMaster University

October 2015

Doctor of Philosophy (2015)	McMaster University
(Civil Engineering)	Hamilton, Ontario

TITLE:	Seismic Performance Assessment of Ductile Reinforced Concrete Blocks Structural Walls
AUTHOR:	Mustafa Siyam
	B.Eng. & Mgmt. (McMaster University)
SUPERVISORS:	Dr. Wael W. El-Dakhakhni
	Dr. Robert Drysdale (Co-Supervisor)
NUMBER OF PAGES:	xvii, 190

ABSTRACT

Reinforced masonry (RM) has been gaining a wide acceptance in the low- and mid-rise construction market as an economic and durable structural system. However, challenges still exist in the area of seismic design because of the poor performance of unreinforced masonry during recent earthquake events in Iran 2003, Haiti 2010, Japan 2011, New Zealand 2011 and Nepal 2015. The dissertation investigated the seismic performance of six concrete block structural walls in an effort to evaluate their force-, displacement- and performance- based seismic design parameters. The walls fall under the *ductile shear wall/special reinforced wall* seismic force resisting system (SFRS) classification according to the current North American masonry design standards. More specifically, the dissertation is focused on evaluating if such walls, designed under the same prescriptive design provisions, having different cross-section configurations would possess similar seismic performance parameters. This was established through an experimental and analytical program by subjecting the walls to a displacement controlled quasi-static cyclic analysis. Different wall configurations were tested including, rectangular, flanged and slab-coupled walls. Test results confirmed that walls designed under the same SFRS classification, but with different configurations, have different seismic performance parameters that included ductility capacity; yield and post yield displacement; stiffness degradation; period elongation and equivalent viscous damping. The current North American masonry design provisions do not account for such difference in the ductility capacities between the walls. The thesis analyses were concluded by quantifying the seismic vulnerability of a RM SFRS comprised of shear walls similar to those tested, through the development of collapse fragility curves and the assignment of an adjusted collapse margin ratio, *ACMR* following the FEMA P-58 and P-695 guidelines. The system were deemed acceptable since the *ACMR* was greater than $ACMR_{10\%}$ (2.35 > 2.31). Therefore, the selected RM SFRS which was designed to meet the prescriptive requirements of the *ductile masonry walls* classification of the CSA S304 (CSA 2014), shows potential capacity against collapse under high intensity earthquakes in one of the highest seismic zones in western Canada and it should be considered as a viable SFRS in seismic design of structures. The procedure described in the chapter can be adopted to investigate the collapse fragility of other SFRS in different seismic regions through careful selection and scaling of the ground motion records associated with such region's seismicity.

ACKNOWLEDGEMENTS

First of all, I want to begin by praising and thanking, the creator of the Heavens and the Earth, Allah, for his ultimate grace and mercy and giving me the capability to complete this work. Secondly, I owe gratitude to my parents and siblings who supported me throughout my life. Thirdly, I want to thank my wife who sacrificed her time, was patient with me throughout this journey and was extremely helpful with her support, which helped me complete my PhD dissertation.

I was very fortunate and privileged to work under the supervision of Dr. Wael W. El-Dakhakhni. He was my mentor rather than a supervisor who helped me gain significant interpersonal skills far beyond the technical skills I learned from conducting my research under him. I am grateful for his support, encouragement and advice. This research would not have been successfully completed without his guidance.

Furthermore I would also like to acknowledge with much appreciation the crucial role of my co-supervisor Dr. Robert Drysdale and my committee members, Drs. Dieter Stolle and Ng Eu-gene who offered guidance and support during the development of this work. Special thanks go to Drs. Dimitrios Konstantinidis and Lydell Weibe who gave me insights in challenging areas of my research including numerical modelling.

I also owe special thanks to the manager of the Applied Dynamics Laboratory, Kent Wheeler and the lab technicians Dave Parret and Paul Heerema of McMaster University, who assisted me tremendously in completing my experimental phase of this study. Financial support to this research has been provided by the McMaster University Centre for Effective Design of Structures (CEDS) funded through the Ontario Research and Development Challenge Fund

(ORDCF), as well as the Natural Sciences and Engineering Research Council (NSERC) of Canada Industrial Postgraduate Scholarship IPS-2 in collaboration with the Canada Masonry Design Centre (CMDC). Provision of mason time by Ontario Masonry Contractors Association (OMCA) and the CMDC under the supervision of Mr. David Stubbs is much appreciated. The supply of the scaled blocks by the Canadian Concrete Masonry Producers Association (CCMPA) is gratefully acknowledged. Finally, this research would not be possible without the help of my peers and colleagues starting with Omar El-Azizy, Paul Heerema, Bennett Banting, Mostafa El-Sayed, Ahmed Ashour, Barry Foster, Mohammed Sayed, Ahmad Sabry, Anna-Krystyna Rzezniczak, Carly Connor, Miqdad Khalfan, Yasser Khalifa and Yasser Anany.

CO-AUTHORSHIP

This dissertation has been prepared and written in accordance to the rules of a sandwich thesis format required by the faculty of graduate studies at McMaster University. The thesis consists of the following chapters:

Chapter 2

Siyam, M., El-Dakhakhni, W., Shedid, M., and Drysdale, R. (2015a). "***Seismic Response Evaluation of Ductile Reinforced Concrete Block Structural Walls. I: Experimental Results and Forced-Based Design Parameters***". ASCE Journal of Performance of Constructed Facilities, published in 29th of July 2015.

Design of Experimental program and analysis of experimental data were performed by Mustafa Siyam. Chapter 2 consists of the design of experimental program and analysis of experimental data. The chapter was written by Mustafa Siyam under the supervision of Dr. Wael El-Dakhakhni, as well as Dr. Marwan Shedid and Dr. Robert Drysdale who provided editorial and several comments on the chapter.

Chapter 3

Siyam, M., El-Dakhakhni, W., Banting, B., and Drysdale, R. (2015b). "***Seismic Response Evaluation of Ductile Reinforced Concrete Block Structural Walls. II: Displacement- and Performance-Based Design Parameters***". ASCE Journal of Performance of Constructed Facilities, published in 29th of July 2015.

Analysis performed on the experimental data was done by Mustafa Siyam. Chapter 3 contains further analysis on experimental work conducted at McMaster University. The chapter was written by Mustafa Siyam under the supervision of Dr. Wael El-Dakhakhni, as well as Dr. Bennett Banting and Dr. Robert Drysdale who provided editorial and technical comments on the chapter.

Chapter 4

Siyam, M., Konstantinidis, D. and El-Dakhakhni, W., (2015). "***Collapse Fragility Evaluation of Ductile Reinforced Concrete Block Walls Systems for Seismic Risk Assessment***". ASCE Journal of Performance of Constructed Facilities, submitted for review in June 2015. Chapter 4 consists of numerical modelling and collapse fragility assessment. The chapter was written by Mustafa Siyam under the supervision of Drs. Dimitrios Konstantinidis and Wael El-Dakhakhni who provided editorial and technical comments on the chapter. Moreover, Dr. Konstantinidis checked the results of the numerical model and IDA.

TABLE OF CONTENT

LIST OF TABLES

LIST OF FIGURES

LIST OF ABBREVIATIONS AND ACRONYMS

ACI –	American Concrete Institute
ACMR–	Adjusted Collapse Margin Ratio
ASCE –	American Society of Civil Engineers
ASTM –	American Society for Testing and Materials
ATC –	Applied Technology Council
CMR–	Collapse Margin Ratio
CSA –	Canadian Standards Association
DBSD –	Displacement-Based Seismic Design
DM –	Damage Measure
DOC –	Degree of Coupling
DS –	Damage State
DSW –	Ductile Shear Walls
FBSD –	Force-Based Seismic Design
FEMA –	Federal Emergency Management Agency
IDA –	Incremental Dynamic Analysis
IDR –	Inter-storey Drift Ratio
IM –	Intensity Measure
MSJC –	Masonry Standards Joint Committee
NBCC –	National Building Code of Canada
NLTHA –	Non-linear Time History Analysis
NRCC –	National Research Council of Canada
PBSD –	Performance-Based Seismic Design
RC –	Reinforced Concrete
RM –	Reinforced Masonry
RMSW –	Reinforced Masonry Shear Wall
RMSWS –	Reinforced Masonry Shear Wall System
SC –	Slab-Coupled
SSF –	Spectral Shape Factor
SFRS –	Seismic Force Resisting System
SRA –	Seismic Risk Assessment
TMS –	The Masonry Society

DECLARATION OF ACADEMIC ACHIEVEMENT

This thesis presents experimental and analytical work carried out by Mustafa Siyam, herein referred to as "the author" with advice and guidance provided by the academic supervisors Drs. Wael W. El-Dakhakhni and Robert Drysdale. Information used from outside sources towards analysis or discussion is cited appropriately in the dissertation.

CHAPTER 1: INTRODUCTION

1.1 STATEMENT OF THE PROBLEM

Masonry structures have been one of the preferred choices for low to mid-rise construction worldwide. This can be attributed to the ease of handling and inexpensive construction costs of masonry; making it economically competitive when compared to concrete and steel buildings. However, recent earthquakes such as the ones in Iran 2003, Haiti 2010, China 2010, New Zealand 2011, Japan 2011 and in Nepal 2015 continue to expose the seismic vulnerabilities that *unreinforced* masonry structures are prone to have. On the national level, a very recent incident occurred, where a 5.0 magnitude earthquake hit a large portion of Ontario on June 23rd 2010, raising the need to be precautious in designing and analyzing structures. This justifies the ongoing shift in Canada and the USA towards reinforced masonry (RM) construction due to enhanced performance such structures exhibit in regions of moderate to high seismicity.

RM shear wall buildings are one type of effective Seismic Force Resisting System (SFRS) that can be used in moderate- and high seismic regions. In such buildings the walls are designed to resist both gravity loads and lateral loads such as earthquakes. Following *capacity design* philosophy, in such regions the walls must be designed to form plastic hinges near the base of walls to acquire enough ductility to meet the drift demands imposed on the structure during a seismic event. The main idea in *capacity design* philosophy is that certain components of the lateral force resisting systems are specifically designed and detailed for energy dissipation under large imposed displacements. As outlined in Paulay and Priestley's seminal work in 1992, the procedures involve:

1. Identifying the critical locations in the component designated as the *plastic hinges.* These members are designed to exhibit large inelastic flexural action by detailing it to ensure the estimated ductility demands are met.
2. Inhibiting undesired modes of failures such as shear and anchorage failure within the plastic hinges. This is done by ensuring that the strength of these modes exceeds the capacity of plastic hinges regions including it's over strength.
3. Other members, which are susceptible to brittle failure, are designed to remain elastic by ensuring their capacity exceeds that of plastic regions at over strength.

Normally in a typical building, the use of different wall configurations is common to suit different architectural requirements and the walls in the building are designed according to prescriptive detailing requirement set by code provisions. A large scale research effort was established at McMaster University for the purpose of evaluating the seismic performance of RM SFRS realizing the complex seismic behaviour of RM. The research was split into three phases to reach the ultimate objective. The first phase focused on evaluating the seismic performance of shear wall components with cross-sectional configurations that exist in RM building design. The second phase investigated the seismic performance of shear wall building with no wall-slab coupling. Finally in the third phase, the seismic performance of shear wall buildings with wall-slab coupling was examined. The latter sheds some light on understanding the RM SFRS performance and its relationship with component-level seismic behaviour that is currently used in design code standards. The walls in the building were detailed to meet the *ductile shear walls* (DSW) or *special reinforced masonry walls* (RMWs) SFRS shear wall classification according to the Canadian Standards Association S304-14 (CSA 2014) or TMS 402-13/ACI 530-13/ASCE 5-13 Masonry Standard Joint Committee (MSJC 2013) North American design provisions.

The goal of this dissertation is *seismic performance assessment of shear wall components with cross-sectional configurations that might exist in typical RM buildings*. This was established by considering a holistic approach for the seismic evaluation of RM masonry components within the context of force-, displacement- and performance-based design. Finally the lateral load and the maximum inter-storey drift capacities of the walls were connected together by conducting a seismic risk assessment (SRA) of a RM SFRS through developing collapse fragility curves, following FEMA P-58 and P-695 guidelines (ATC 2009 and ATC 2012), to examine the seismic vulnerability of that RM SFRS.

1.2 MOTIVATION

Review of available literature indicates that few experimental research programs have been carried out to quantify the seismic performance of RM buildings as a whole. As mentioned previously, in an effort to quantify the seismic performance of such structures, McMaster University has initiated a research team to acquire this goal. The team is comprised of the author and two other candidates, Paul Heerema and Ahmed Ashour. Figure 1.1 shows the different research phases, outlining the focus of each researcher to reach the ultimate goal mentioned earlier. In typical building designs, due to architectural requirements, the walls might possess the same overall aspect ratio but have different cross-section configurations. The ductility capacity of the masonry SFRS and, therefore, its components (i.e. the structural walls) depends on the reinforcement ratios, axial load and the component cross-section (Priestley, 2000). As such, assigning the same displacement ductility capacity values for each SFRS classification, as is currently implied in North American codes using ductility-related force reduction factors, might result in inconsistent response predictions (Priestley et al., 2007). This was the motivation to examine the seismic design parameters in general which is comprised of force-based, displacement-based and performance-based design parameters, of the highest SFRS shear wall classification according to North American design provisions.

The numerical analysis was needed considering the fact that after the 2011 Christchurch earthquake in New Zealand, a significant number of reinforced masonry low-rise buildings were deemed unusable, although the damage was repairable. This raised a concern for investigating the seismic collapse performance of a RM SFRS following the FEMA P-58 (ATC 2012) methodology to evaluate its seismic vulnerability. Incremental dynamic analysis (IDA) was used to develop collapse fragility curves of a RM SFRS as part of seismic risk assessment (SRA) of RM structures.

1.3 OBJECTIVES

The objectives of this research are outlined as follows:

1. Experimentally investigate the seismic performance of ductile reinforced concrete block structural walls that are detailed following the same prescriptive code requirements from the North American masonry design provisions, CSA S304-14 (CSA 2014) and TMS 402-13/ACI 530-13/ASCE 5-13 (MSJC 2013), respectively.
2. Investigate force-, displacement- and performance-based seismic design parameters of ductile shear walls or special reinforced walls, SFRS shear wall classification according to the CSA S304-14 and MSJC-13 code provisions, respectively.
3. Examine the effect of in-plane slab-coupling in RM shear walls.
4. Develop a simplified analytical model that is capable of estimating the in-plane dynamic response of RM SFRS due to seismic loading.

5. Utilize the analytical model to conduct an incremental dynamic analysis (IDA) for a typical RM SFRS.
6. Evaluate the seismic performance of a typical RM SFRS through a collapse fragility assessment to know where it stands in terms of seismic vulnerability. This was done using the most current Canadian design provisions, the NBCC 2010 (NRCC, 2010) and the CSA S304-14 which contributes to the seismic risk assessment of RM shear wall buildings.

1.4 SCOPE

The research objectives mentioned above were met by conducting an experimental testing program comprising six fully grouted reinforced concrete block structural walls subjected to quasi-static displacement controlled loading. The walls in the test matrix had various cross-sectional configurations that exist in the design of RM buildings. The walls were designed and detailed to meet the *ductile shear walls/special reinforced walls* SFRS shear wall classification according to CSA S304-14 and the TMS 402-13/ACI 530-13/ASCE 5-13 (MSJC-13), respectively. The research focused on quantifying key force-based, displacement-based and performance-based seismic design parameters to evaluate the seismic performance of such shear wall classification, with different cross section configurations. Moreover, the research examined the difference in seismic parameters within the same shear walls classification group. The experimental results are then used to calibrate a numerical model created in OpenSees (McKenna et al., 2000) interface to represent a typical RM SFRS. The calibrated model was subsequently used to conduct a collapse fragility assessment to evaluate the seismic vulnerability of this type of SFRS.

1.5 Thesis Organization And Background Information

The dissertation was written in a sandwich thesis format consisting of three journal articles, two of which have been published (Chapters 2 and 3) and one has been submitted for review (Chapter 4). Due to such format, there is some overlap that exists between the chapters particularly in the introduction, literature review and description of the experimental program. To begin with, Chapter 2 contains the work presented in the following published journal article:

Siyam, M., El-Dakhakhni, W., Shedid, M., and Drysdale, R. (2015). "Seismic Response Evaluation of Ductile Reinforced Concrete Block Structural Walls. I: Experimental Results and Force-Based Design Parameters." *J. Perform. Constr. Facil.* ,10.1061/(ASCE)CF.1943-5509.0000794 , 04015066.

The chapter focused on evaluating the force-based seismic design parameters since the current Canadian code provisions use a force-based approach to calculate the seismic demand also known as the equivalent static force procedure. This method is used when dynamic analysis of the structure is not required as specified in the National Building Code of Canada, NBCC 2010 (NRCC, 2010).The method evaluates the lateral base shear denoted as (V) which is a function of the design spectral acceleration corresponding to the fundamental period of the structure (T_a), the higher mode effects (M_v), the importance category of the structure (I_E), the weight of structure (W) and finally the force modification factors which consist of a ductility-related factor (R_d) and an over-strength related factor (R_o). The relation is illustrated in Eq. (1.1):

$$V = \frac{S_a(T) \cdot W \cdot I_e \cdot M_v}{R_d R_o} \tag{1.1}$$

It is intuitive from equation (1.1) that, by increasing the response modification factors, one can reduce the seismic demand imposed on the structure and thereby provide a more economical SFRS system. Until recently, the use of R_d and R_o factors was mostly based on engineering judgment which caused the great variability in the numbers when compared between different international codes. The current Canadian Standards Association (CSA) S304-14, "Design of Masonry Structures" sets an R_d factor (ductility-related force modification factor) of 3.0 for ductile shear walls (DSW) (R = 4.5 if R_d is multiplied by R_o of 1.5) while MSJC sets an R value of 5 (the R here includes the over strength component as well) for special reinforced walls. Results from this research shed some light on the difference in the approaches adopted for essentially the same classes of SFRS, which reflects the difference in modification factor used in various North American codes.

Chapter 3 contains the work presented in the following published journal article:

Siyam, M., El-Dakhakhni, W., Banting, B., and Drysdale, R. (2015). "Seismic Response Evaluation of Ductile Reinforced Concrete Block Structural Walls. II: Displacement and Performance–Based Design Parameters." *J. Perform. Constr. Facil.* ,10.1061/(ASCE)CF.1943-5509.0000804 , 04015067

Chapter 3 included an evaluation of the displacement-based and performance-based seismic design parameters. These parameters such as the wall yield and ultimate curvatures, wall displacements at yield and at the post-yield stages, stiffness degradation, period elongation and equivalent viscous damping, are crucial components of displacement-based design. Displacement-based design has gained wide acceptance in the research community as a reliable method in seismic design of structures. Unlike the force-based approach, the method characterizes the structure by the secant stiffness (K_e) at the maximum target displacement Δ_d and equivalent viscous damping (ζ_{eq}) appropriate to the hysteretic energy absorbed during inelastic response. The design base shear at maximum response is calculated by multiplying the effective stiffness K_e by Δ_d .The maximum target displacement is first acquired from code drift limits. For the certain displacement ductility and specific type of structure, the damping ratio (ζ_{eq}) can be estimated. Then by using the design displacement spectra the effective period of the structure can be approximated by knowing the damping ratio and for a given target displacement. Finally the effective stiffness can be calculated using Equation (1.2).

$$K_e = \frac{4\pi^2 m_e}{T_e} \tag{1.2}$$

Where m_e denotes the effective mass of the substitute SDOF system.

Chapter 4 comprises the work presented in the following submitted journal paper:

Siyam, M., Konstantinidis, D. and El-Dakhakhni, W., (2015). “Collapse Fragility Evaluation of Ductile Reinforced Concrete Block Walls Systems for Seismic Risk Assessment”. *ASCE Journal of Performance of Constructed Facilities*, submitted for review in June 2015.

Chapter 4 discussed the seismic performance assessment process as outlined by FEMA P-58 (ATC 2012) for a typical RM SFRS. Performance based design as defined in FEMA 461 (ATC 2007) in Section 1.2 is a process that permits the design of buildings with a realistic and reliable understanding of the risk of life, occupancy and economic loss that may occur as a result of future earthquakes. The steps involved in the process include the following:

1. Establishment of appropriate performance objectives that define expected building performance in future earthquakes.
2. Development of a preliminary design capable of providing the desired performance.
3. Assessment of whether the design is actually capable of providing this performance through evaluation of the probability of experiencing losses of different types.
4. Adjustment of the design until the performance assessment process indicates a risk of loss that is acceptable.

The chapter described the whole process of performance assessment as outlined in the FEMA P-58 document with the exception of loss function estimation. Each section in this chapter discussed one step of the process starting with, developing an analytical model to describe RM SFRS seismic behaviour, defining the earthquake hazards, analyzing the building response through incremental dynamic analysis (IDA) and developing collapse fragility curves. The collapse fragility curves were then used to quantify an adjusted collapse median ratio (*ACMR),* a ratio that defines if the seismic performance of a SFRS is acceptable against collapse prevention. As outlined by Hamburger et al. 2004, the seismic performance of the structure can only be expressed with probabilistic functions, because of the uncertainties existing in the seismic demand and capacity which directly affect the performance of the structure. The uncertainties in seismic demand comes from uncertainties in the prediction of the level of future ground motions. On the other hand, uncertainties in seismic capacity arise from uncertainties in the material behaviour, modelling assumptions and structural response. Therefore, the Next Generation PBSD aims to develop procedures to communicate the performance levels to the decision-making authorities, considering uncertainties that exist in the engineering analyses of structures. Therefore, it is crucial to employ probabilistic functions to relate the uncertainties involved in each of the parameters affecting the performance of the structure. In this context, fragility functions are one of the main probabilistic functions required to express the performance of the structures.

Finally Chapter 5 summarized the main conclusions from the experimental and numerical analyses followed by recommendations from this research and suggestions for future work.

1.6 CHAPTER 1 NOTATION

The following symbols are used in this chapter:

K_e = effective stiffness of substitute structure (KN/mm);
I_e = importance category of a structure;
M_v = Higher mode effects;
m_e = effective mass of substitute structure (kg);
R= response modification factor;
R_d = ductility related force modification factor;
R_o = over-strength modification factor;
$S_a\,(T_a)$ = design spectral acceleration at fundamental period T_a (g)
T_a = fundamental period of structure (s);
T_e = effective period of structure (s);
V = lateral base shear (kN)
W = weight of the building (g);
Δ_d = maximum target displacement (mm);
ζ_{eq} = equivalent viscous damping (%);

1.7 Chapter 1 References

Applied Technology Council (ATC). (2007). “Interim Testing Protocols for Determining the Seismic Performance Characteristics of Structural and Non-structural Components” *Federal Emergency Management Agency* (*FEMA) 461*, Washington D.C., USA.

Applied Technology Council (ATC). (2009). “Quantification of Building Seismic Performance Factors.” *Federal Emergency Management Agency (FEMA)* P-695, Washington, DC.

Applied Technology Council (ATC). (2012). “Seismic Performance Assessment of Buildings: Volume 1- Methodology” *Federal Emergency Management Agency* (*FEMA) P-58-1*, Washington D.C., USA.

Canadian Standards Association (CSA). (2014) “Design of masonry structures.” CSA S304-14, Mississauga, Canada.

Ezzeledin, M., Lydell, W., Shedid, M., El-Dakhakhni, W. (2014) “Numerical modelling of reinforced concrete block structural walls under seismic loading”, *9th International Masonry Conference*, Guimarães, Portugal.

Hamburger, R., Rojahn, C., Meohle, J., Bachman, R., Comartin, C., and Whittaker, A. (2004). “The ATC-58 Project: Development of Next-Generation Performance-Based Earthquake Design Criteria for Buildings.” *13th World Conference on Earthquake Engineering*, Vancouver, BC, Canada, CD-ROM.

Masonry Standards Joint Committee of the American Concrete Institute, American Society of Civil Engineers, and The Masonry Society (MSJC). (2013). “Building code requirements for Masonry Structures.” TMS 402-13/ASCE 5-13/ACI 530-13, Detroit, MI, New York, and Boulder, CO.

McKenna, F., Fenves, G. L., Scott, M. H., and Jeremic, B., (2000). Open System for Earthquake Engineering Simulation (OpenSees). Pacific Earthquake Engineering Research Center, University of California, Berkeley, CA.

National Building Code of Canada (NBCC). (2010). “National Building Code of Canada 2010.” *NRCC-10*, Ottawa, Canada.

Paulay T., and Priestly, M. (1992). *Seismic design of reinforced concrete and masonry buildings*, Wiley, New York.

Priestley, M. J. N. (2000). “Performance-based seismic design” Keynote Address, *Proceedings of the Twelfth World Conference on Earthquake Engineering.* Earthquake Engineering Research Institute, Auckland, New Zealand, Paper #2831.

Priestley, N., Calvi, G., and Kowalsky, M. (2007). *Displacement-based seismic design of structures*, IUSS Press, Pavia, Italy.

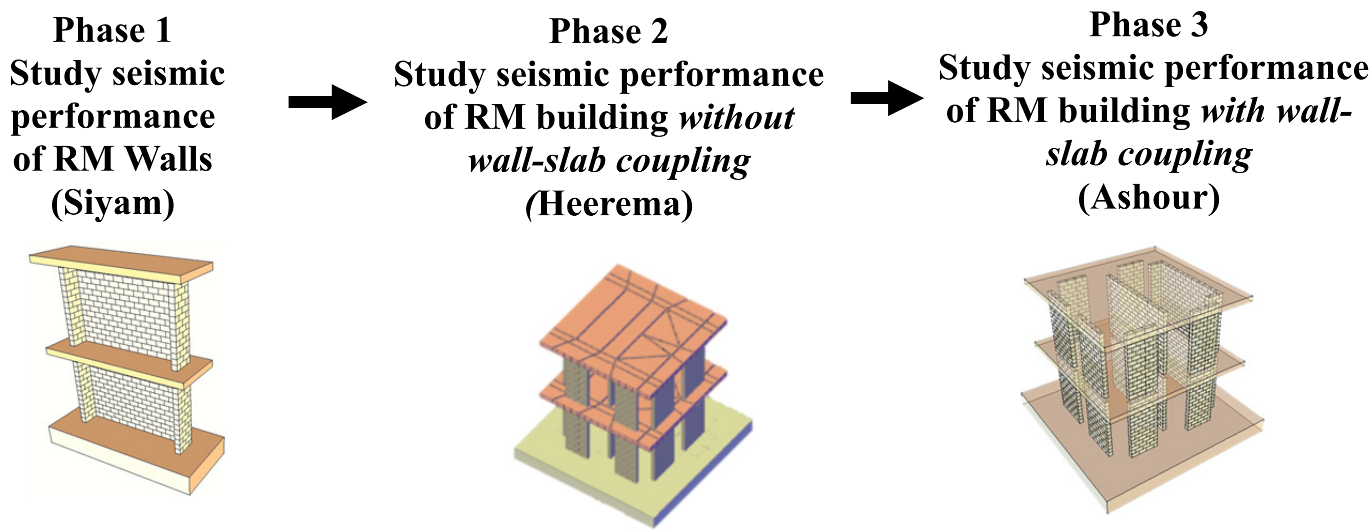

Fig. 1.1 McMaster research program phases

CHAPTER 2: SEISMIC RESPONSE EVALUATION OF DUCTILE REINFORCED CONCRETE BLOCK STRUCTURAL WALLS. I: EXPERIMENTAL RESULTS AND FORCED-BASED DESIGN PARAMETERS

ABSTRACT: The reported experimental study documented the performance of six fully grouted reinforced concrete block structural walls tested under quasi-static cyclic loading. The walls are classified as *ductile shear walls* and the *special reinforced masonry walls* seismic force resisting system (SFRS) classification of the CSA S304-14 and the TMS 402-13/ACI 530-13/ASCE 5-13 (MSJC-13) Canadian and American standards, respectively. Such classification prescribes the highest detailing requirements for seismic design of RM walls. The test matrix comprised one rectangular, one flanged, and two slab-coupled walls, all with an overall aspect ratio of 1.4. In addition, two rectangular walls, representing the individual components of the slab-coupled wall systems, were tested to quantify the wall slab coupling effects. In addition to discussing the experimental results, the study also presented key force-based seismic design (FBSD) parameters, such as the wall lateral load capacity, plastic hinge length, wall failure modes, and displacement ductility capacities. Moreover, the effects of wall cross sectional configuration and slab coupling on the cyclic response and deformation capabilities of the walls were discussed. In general, the yield and ultimate loads were found to be accurately predicted using the CSA S304-14 and MSJC-13 formulations. The wall experimental displacement ductility values (calculated at 20% strength degradation) ranged between 5.4 and 7.6 whereas the idealized displacement ductility values at the same strength degradation level ranged between 3.4 and 5.4. The idealized displacement ductility is directly related to the ductility related force modification factor, R_d which is crucial in seismic design of structures using the equivalent static lateral force method. The analysis results reported in the chapter highlight the fact that walls designed and detailed within the same SFRS classification possess significantly different FBSD parameters. The results also indicated that slab-coupling, although not recognized as a wall coupling mechanism in the current editions of the CSA S304 and MSJC, can have significant influence on the seismic response of ductile/special reinforced masonry wall systems.

Keywords: Cyclic loading, Ductility, Plastic hinge length, Reinforced Masonry, Structural wall, Seismic performance, Slab-coupling.

2.1 INTRODUCTION

The seismic performance of reinforced masonry (RM) structural walls has been under investigation for more than four decades (Priestley 1976, Priestley and Elder 1982, Fattal 1991, Leiva 1991, Shing et al. 1990-a and -b, Eikanas et al. 2003, Shedid 2009, Shedid et al 2010a, Vasconcelos and Lourenço 2009, Voon and Ingham 2006 and 2008, Haach et al. 2010, Banting and El-Dakhakhni 2012, El-Dakhakhni et al. 2013, Ahmadi et al. 2014). These studies have shown that, by adopting the capacity design philosophy, cantilever walls can be designed to fail in a flexural manner whereby they can undergo high displacements through inelastic deformations in critical regions, referred to as plastic hinges, located in the vicinity of the wall bases. Shear capacity in such regions has to exceed the shear demand developed under the maximum flexural capacity of the wall in order to prevent brittle failure and to allow for a ductile wall response accompanied by significant energy dissipation (Paulay and Priestley 1992). However, the majority of reported studies focusing on quantifying the seismic response of RM wall systems have not explicitly considered the variation in the seismic response parameters between walls detailed within the same seismic force resisting system (SFRS) classification. In addition, although several research programs focused on quantifying the response of individual walls, studies focusing on evaluating the seismic response of slab-coupled RM walls, similar to the ones reported in the current chapter, are extremely scarce.

In North American codes, RM SFRS are classified based on their expected level of ductility under seismic loading. In the Canadian Standards Association “Design of Masonry Structures” S304-14 (CAN/CSA 2014-a) shear walls are classified into three categories, conventional (non-seismically detailed), moderately ductile, and ductile. Similarly, in the American TMS 402-13/ACI 530-13/ASCE 5-13 Masonry Standards Joint Committee code (MSJC 2013), RM SFRS are classified as ordinary, intermediate and special. The walls reported in the current study fall under the *ductile shear walls* and the *special reinforced masonry walls* SFRS classification according to the Canadian S304-14 (CAN/CSA 2014-a) and the American (MSJC 2013) masonry standards, respectively. The objective of the current chapter is to evaluate variations in key force-based seismic design (FBSD) parameters of individual and slab-coupled ductile/special RM walls with the same prescriptive detailing requirements, the same overall aspect ratio, but with different cross section configurations. The experimental results are also expected to contribute to the growing experimental seismic performance database of RM shear wall systems to facilitate benchmarking and future numerical model calibration. In the following sections, the observations from the experimental tests were documented and key FBSD parameters, including wall lateral load capacities, displacement ductility levels, and the different wall plastic hinge lengths, were quantified and related to the wall configurations.

2.2 Experimental Program

The experimental program was designed to investigate the flexural response of fully-grouted RM shear walls tested under quasi-static cyclic loading. The tested one-third scale walls had a height of 2.16 m (corresponding to 6.6 m in full-scale) with an inter-storey slab located at height of 1.04 m on center from foundation/wall interface, and a roof slab. In this respect, in their text, Harris and Sabnis (1999) discuss several experimental studies that focused on the performance of scaled reinforced masonry at the material-, assemblage-, component-, and system-levels. In addition, earlier research studies by Hamid and Aboud (1985) have indicated a good correlation between full-scale masonry prototypes and the corresponding scaled models. More recently, there has been a considerable number of research studies that focused on utilizing scaled reinforced masonry shear wall models to predict the response of their full-scale counterparts (Shedid et al. (2010a, 2010c), Shedid and El-Dakhakhni (2014), Banting and El-Dakhakhni (2012a, 2014a, 2014b) and Hereema et al (2014, 2015)).

As shown in Fig. 2.1, the test matrix consisted of one rectangular wall (W1), one flanged wall (W2) and two slab-coupled walls systems, (W3 and W4), with an overall aspect ratio of 1.4. The wall's behaviour is analyzed as a system and therefore for the slab-coupled walls the total length comprising of the two individual walls, in addition to the coupling slab length is used in the aspect ratio calculations. In order to facilitate quantifying the slab coupling influence on the wall response, two individual rectangular walls (W5 and W6) were also constructed and tested as they presented individual components of the slab-coupled wall systems, W3 and W4, respectively. The hysteretic behaviour, ductility and post-peak response of the walls at defined response levels were documented and the loading continued until wall failure in order to obtain enough information about the walls' post peak responses. Failure was defined when the wall extreme bars fractured at both ends.

2.2.1 Material Properties

In this study, the third-scale version of the standard 190 mm concrete blocks used in the construction of the walls was 130 mm long, 63 mm thick and 63 mm high. For the walls' vertical (flexural) reinforcement, scaled D7 (7.6 mm diameter) bars were used as the scaled version of the conventional full-scale M20 steel bars. For the horizontal (shear) reinforcement, W1.7 smooth bars (3.8 mm diameter), which represented a scaled version of the full-scale M10 bars, were used and were hooked around outermost vertical bars. However, no shear or slippage failures were observed during testing. The mechanical properties of the wall constituent materials (blocks, mortar, grout, scaled reinforcement) were obtained through a series of standardized tests ASTM CI09-08 (ASTM 2008), CI019-08 (ASTM 2008), CSA A165 (CSA 2014-b), CSA A179-14 (CSA 2014-c) and the average yield strengths, f_y of the D7 and W1.7 reinforcements, were 495 and 670 MPa respectively (Appendix A), based on the tensile strength tests according to CSA G30.18-09 (CSA 2014-d). The W1.7 reinforcements were the only equivalent bars that correspond to full scale M10 rebars noting the fact that its yield strength is higher than the normal M10 rebars used in practice.

The average compressive strength of the masonry blocks was 25.2 MPa according to ASTM C140-08 (ASTM 2008) and CSA A165-14 (CSA 2014-b). Type S mortar was used in wall construction with weight proportions corresponding to 1.0:0.2:3.5:0.85 (Portland cement: lime: dry sand: water), and having an average flow of 127%. Forty-two mortar cubes were tested in compression according to the CSA A179-14 (CSA 2014-c) and resulted in an average compressive strength of 18.7 MPa (COV = 22%). Wall construction was conducted using approximately 3.0 mm thick mortar joints representing the scaled version of the common 10 mm joints in full-scale masonry construction. Premixed grout with weight proportions 1.0: 0.04: 3.9: 0.85 (Portland cement: lime: dry sand: water) was used to reach a target slump of 250 mm and resulted in an average grout compressive strength of 17.1 MPa (COV = 18.7%) based on testing 30 grout cylinders as specified by ASTM C1019-05 (2005b) and CSA A179-14 (CSA 2014-c). Twenty-four fully grouted masonry prisms, that were four-block high and one-block long, were tested and resulted in an average masonry compressive strength, f'_m, of 19.3 MPa (COV = 19.8%) (Appendix A). All the results of the compressive strengths' of the wall constituents are presented in Appendix A.

2.2.2 Wall Characteristics, and Test Setup, Instrumentation and Procedure

All walls had an aspect ratio $h_w/l_w > 1.0$ [h_w= wall height; and l_w = wall length] to promote flexural dominated behaviour and were detailed to meet the requirements for the ductile/special RM SFRS classification specified by the CSA S304-14 and the MSJC-13, respectively. For ease of reference, the detailing requirements for the ductile wall classification by the CSA S304-14 (CSA 2014-a) prescribe minimum horizontal and vertical reinforced steel ratios value of 0.067% of the gross cross-sectional area of the wall. In addition, the walls should be checked for adequate ductility by ensuring that the inelastic rotational capacity of the wall, θ_{ic}, is greater than the inelastic rotational demand, θ_{id}. Moreover, the maximum spacing of vertical reinforcement within the plastic hinge zone shall not exceed the lesser of the value of 6(t +10) mm [t = wall thickness], 1,200 mm or one-quarter of the wall length, but need not be less than 400 mm where the spacing required for strength is greater than 400 mm. Moreover, the spacing of horizontal reinforcement shall not exceed 600 mm or one-half of the wall length. Finally, the horizontal reinforcing bars shall have 180° standard hooks around vertical reinforcement at the ends of the wall and shall not be lapped within 600 mm or $l_w/5$, whichever is greater, from the end of the wall. For the special reinforced masonry wall classification, the MSJC-13 (MSJC, 2013) specifies a maximum vertical/horizontal reinforcement spacing of the smallest of one-third the length or the height of the shear wall and 48 in. (1,200 mm). The MSJC-13 also requires the area of vertical reinforcement to be at least one-third of the required shear reinforcement, with the sum of the cross-sectional areas of horizontal and vertical reinforcement being at least 0.002 of the gross cross-sectional area of the wall.

As mentioned earlier, Walls W1, W2, W3 and W4 had the same overall aspect and reinforcement ratios but differed in their cross sectional configuration. Regarding the reinforcement detailing, all rectangular walls had bars spaced every other cell (133 mm which corresponds to 400 mm in full scale as shown in Fig. B-1a in Appendix B). On the other hand, the flanged wall was reinforced differently but in a way to keep the reinforcement ratio constant and symmetric along the wall cross section (See Fig B-1b in Appendix B). This ensured that all the walls had almost the same vertical steel ratio of approximately 0.6%. To account for high damage in the plastic hinge zone, CSA S304-14 (CSA 2014-a) stipulates that shear force in walls over the plastic hinge length, l_p, be resisted solely by the reinforcement. Therefore, the horizontal reinforcements are spaced at 65 mm (0.26% i.e., every course) in the first floor and then increased to 130 mm (0.14%, i.e., every other course) in the second storey in all the test walls (see Fig. B-1a). For slab detailing, in the rectangular and flanged walls the slabs do not have a major effect in the in-plane direction other than slightly stiffening the walls. On the other hand, the slabs in the slab-coupled walls play an important role in changing the behaviour of the system. Figure C-1 in Appendix C shows the dimensions and reinforcement details in the coupled walls. The slabs were reinforced with D4 deformed bars (5.8 mm in diameter) ensuring that the minimum code requirements of CSA A23.3 were met. Stress-strain curves for sample D4 bars are provided in Appendix A, Fig. A-4.

It should be noted that the (overall) aspect ratio for the slab-coupled walls (W3 and W4) is established by considering the walls acting as a system comprised of two individual walls connected by the slabs. As such, the slab-coupled Wall W3 essentially represents two Walls W5 connected by a 337 mm (1,011 mm in full-scale) slab at each storey level. Similarly, the slab-coupled Wall W4 represents two Walls W6 connected by a 602 mm (1,806 mm in full-scale) slab at each storey level. Subsequently, Walls W5 and W6 have aspect ratios of 3.6 and 4.6, respectively. The walls were constructed in running bond using stretcher units along the length of the wall with half standard blocks at the wall ends. All walls were constructed by an experienced mason on a 200 mm deep and 600 mm wide reinforced concrete, (RC) foundation. Wall dimensions, configuration, aspect ratio, and reinforcement details are summarized in Table 2.1. The vertical, ρ_v and horizontal, ρ_{h1} and ρ_{h2} symbols denote the wall reinforcement ratios where 1 and 2 represent ratios at the first and second storey levels, respectively.

The test setup shown in Fig. 2.2 included a reusable rigid steel foundation (constructed from fabricated and welded plate sections) that was fixed to the structural floor of the laboratory by 1" post-tensioned steel rods. Prior to testing, each RC foundation was also fixed to the reusable rigid steel foundation using post-tensioned rods. In order to prevent out-of-plane wall displacements during testing, eight steel roller supports [four at each floor] were connected to four 5" by 5" by 1/2" HSS sections steel beams that connect to the reference columns, comprising the out-of-plane bracing system (see Fig. 2.2).

The lateral cyclic load was applied using a hydraulic actuator with a maximum capacity of 500 kN and a maximum stroke of ± 250 mm. The actuator was attached to a stiff steel loading beam on the top of the walls to which the vertical reinforcement was welded. The loading beam is a built up section composed of two angles (3" by 3" by 3/8") facing each other and welded to a thick rectangular plate (12" by 10" by 1/2") which is stiffened by W-sections from the front and back of the beam. Special considerations were accounted for, to test the slab-coupled walls where a modification was made to the steel loading beam to allow the wall tops to rotate without imposing additional restraints or increasing the slab-coupled wall system capacity (Appendix D, Fig. D-1c).

The lateral load was transferred through a series of 50 mm by 50 mm by 6 mm steel caps welded to the top of the loading beam and to the walls' vertical reinforcement. This technique facilitated simulating a diaphragm load transmission mechanism along the length of the shear wall instead of applying point loads at the walls' roof slabs. Figure 2.2 shows the internal and external instrumentation used in the test setup to record displacements and strains during testing of the walls. A total of 28 LVDTs (linear variable differential transducer) were attached to the walls to record horizontal and vertical displacements during testing. One LVDT was used to measure sliding between the bottom steel beam and the concrete footing and another was attached to measure the possible wall sliding between the concrete footing and the wall. Foundation uplift between the wall base and the reusable steel beam was also monitored by means of two LVDTs. Fourteen strain gauges were instrumentd to record strains in the rectangular and flanged walls. Additional 9 LVDTs and 14 strain gauges were needed for the slab-coupled walls to record their displacements and strains, respectively (Appendix D. Fig D-1d). The location of steel strain gauges on the two outermost vertical reinforcement bars is also shown in Fig 2.2. Strain gauges 1B and 4B, attached slightly above the wall-foundation interface were used to define the onset of yielding of the reinforcement. All the LVDTs, strain gauges, and load cell were connected to a data acquisition system for data recording.

The quasi-static cyclic testing protocol was split into force-controlled and displacement-controlled phases. As shown in Fig 2.3, during the force-controlled phase, each wall was loaded to 40%, 60% and 80% of its respective theoretical yield load (calculated using a linear strain profile having yield strain of furthest reinforcement set to 0.0025) as shown in Table 2.2, while monitoring the onset of yielding of the outermost bars using the strain gauges installed at the wall-foundation interface level. Once the actual yield load was reached, the walls were cycled twice at multiples of their respective yield displacements until the wall outermost reinforcement bars fractured; at which point the test was terminated. The following sections discuss the test observations followed by analyses of the experimental results from the FBSD perspective.

2.3 TEST RESULTS

2.3.1 Failure Modes

All the walls were designed to develop a ductile behaviour and fail in flexure. However due to different cross-sectional configurations, crack patterns differed during the loading cycles. Figure 2.4 shows the typical damage sequence for Walls W1 and W2, which represents combined shear-flexure cracks. During the initial loading cycles, bed joint cracks were observed at 60% of the theoretical wall yield strengths and continued to extend in length and width until the outermost bars yielded. Diagonal shear cracks were first observed at the onset of yield ($1\Delta_y$) (by monitoring yield strain of strain gauges 1B and 4B as mentioned above) and kept increasing in number, length and width. The shear cracks were mainly observed over two third of the walls' first storey heights and were concentrated around the wall mid-lengths. At higher load cycles, spalling of masonry occurred at the wall toes and resulted in exposure of the reinforcement. With increased loading, buckling of the reinforcement bars developed and the outermost bars eventually fractured in tension at both wall ends. At this point the test was terminated, typically with the walls experiencing more than 50% strength degradation. Although shear cracks were observed in these walls, the walls did fail in flexure. Wall 1 lost about 20% of its ultimate capacity at 25.6 mm ($4\Delta_y$) corresponding to 1.2% drift and at this cycle, slab cracks were observed and spalling of concrete at the wall toes was first noticed. At the $5\Delta_y$ loading cycle (corresponding to 1.48%% drift), buckling of the outermost reinforcement occurred and an additional 10% degradation in strength was observed (61.1 kN). As for the flanged wall, W2, the first noticeable bar buckling occurred at 1.6% top drift corresponding to 34.7 mm and during the second loading cycle, the wall lost about 20% of its strength.

The slab-coupled Walls W3 and W4 exhibited a different failure mechanism compared to Walls W1 and W2, where, as expected, these walls failed by forming plastic hinges at the bottom of the two walls in addition to hinges at the wall/slab interface regions [Fig. 2.5]. Figure 2.5 shows the slab-coupled walls mechanism when subjected to a lateral force. Following a weak beam (slab)/strong column (wall) mechanism, the damage started at the slab, followed by damage at the wall bases. Due to continued load reversal at high displacement demands, the walls outermost reinforcement bars eventually fractured and thus the test was terminated.

The crack patterns for Walls W5 and W6 were dominated by bed joint (flexural) cracks during the initial stages of loading with head joints cracks observed at the first yield load cycle and almost no shear cracks observed. At higher displacement levels, the walls exhibited uplift on the tension side accompanied by vertical splitting cracks on the compression toe. Under increased wall top displacement demands, face shell and grout spalling occurred and was followed by buckling of the outermost reinforcement bars and their eventual fracture. Figure 2.6 shows the extent of cracking in all six walls at 20% peak strength degradation.

2.3.2 Load Displacement Relationships

The hysteretic response for each wall is depicted in Fig. 2.7 in which the table on the bottom right corner of each graph summarizes the main wall characteristics. The experimental loads at yield, ultimate, and 20% peak strength degradation, annotated by V_y, V_u, $0.8V_u$, respectively, along with the percentage top drift of the wall are all indicated on each wall's graph. The displacement ductility values of the walls, $\mu_{\Delta,}$ defined as the ratio of wall displacement to the displacement recorded experimentally at first yield of the outermost vertical reinforcement in each wall is also presented on the graphs in Fig. 2.7.

The response of all the walls was approximately linear elastic up to the wall yield strength level, corresponding to a wall top drift value that ranged between 0.2% and 0.5%, accompanied by minimal energy dissipation. At higher displacement levels, the wider hysteresis loops were characterized by a reduced capacity at the same displacement level due to stiffness and strength degradations. The ultimate load for all the walls was reached approximately between $2\Delta_y$ and $3\Delta_y$ top displacement, with all the walls displaying symmetrical responses in both loading directions.

2.4 Analysis of Test Results: Forced-Based Seismic Design Parameters

The load-displacement envelopes for the walls presented in Fig. 2.8 show that Wall W6, with the smallest cross-sectional area, had the lowest capacity of +9.9 kN and -8.8 kN whereas Wall W2, with the largest cross-sectional area, yielded the highest capacity of +118.5 kN, and -116 kN for the positive and negative loading direction, respectively.

The effect of altering the wall configuration on the lateral strength and top drift is illustrated in Fig 2.8(b). The peak load of the flanged Wall W2 is 1.4, 2.8 and 4.3 times that of rectangular Wall W1, and the slab-coupled Walls W3 and W4, respectively. The flanges in Wall W2 resulted in a reduced compression zone depth, which in turn resulted in increasing the moment arm and ultimately led to higher wall cross section moment capacity. Wall W3 has 45% higher ultimate load than Wall W4.

The responses of the slab-coupled walls were compared to that of two individual wall components *linked together* (i.e. through link members). Figure 2.8(c) shows the predicted load-displacement response of doubling the load *V,* of the individual Walls W5 (noted in the figure as 2W5) and doubling the load of Wall W6 (noted in the figure as 2W6) as well as the load-displacement relationship of the corresponding slab-coupled Walls W3 and W4, respectively. The figure also shows an increased strength acquired by the slab-coupled walls when compared with that of 2W5 and 2W6. This increase in strength is attributed to the coupling moment, $M_c = F \times l_c$, generated by the slabs within the coupled wall system (where F denotes the axial force, either compression or tension, developed in the individual walls and l_c represents the net span of the coupling slab) [Fig. 2.5] as discussed in the next section.

2.4.1 Wall Strength Predictions

The flexural capacity of RM shear walls can be accurately predicted using cross-sectional analysis (Priestley and Elder 1982; Priestley 1986). The predicted and the experimental yield and ultimate loads of the walls are presented in Table 2. The value of 0.003 was used for the ultimate masonry strain as specified by the CSA S304-14 (CSA 2014-a) to calculate the wall ultimate flexural capacity. For the yield strength, a linear strain profile, with a yield strain of the outermost steel reinforcement set to 0.0025, was used. For all walls, the ratio between the theoretical and the experimental strength V_{exp}/V_{pred} ranged between 0.9 and 1.2, and between 0.8 and 1.1, for the yield and ultimate loads calculations, respectively. The equations used for the calculations summarized in Table 2.2, are listed in the Appendix E.

The capacities of the slab-coupled wall systems (Walls W3 and W4) listed in Table 2.2 were predicted using the procedure proposed by Harries et al. (2004) and Hoenderkamp (2012). These two approaches are originally based on the continuous medium method (Chitty 1947), which requires calculation of the degree-of-coupling, *DOC,* parameter between the walls. The *DOC* indicates the ratio between the coupling moment, $F\times l_c$, and the overall overturning moment, M, resisted individually by the two coupled walls' cross sections, M_i and M_j, in addition to that facilitated through wall coupling as given in Eq. 2.1-a. Equation 2.1-b presents the same relationship in a format that enables evaluating the coupling moment, $M_c = F\times l_c$, directly.

$$DOC = \frac{F \cdot l_c}{M_i + M_j + F \cdot l_c} \qquad (2.1\text{- a})$$

$$F \cdot l_c = \left(M_i + M_j\right)\left[\frac{DOC}{1-DOC}\right] \tag{2.1- b}$$

In order to evaluate the coupling moment given by Eq. 2.1-b, the proposed *DOC* formulation by Hoenderkamp (2012), given in Eq. 2.2 was used, where *C* is a constant that depends on the load configuration (Hoenderkamp (2012)).

$$DOC = \left[1 + (k^2 - 1)\left(\frac{1 + C/(k^2 - 1)}{1 - C}\right)\right]^{-1} \tag{2.2}$$

Eq. 2.2 was derived by solving the governing differential equation for coupled walls (Eq. 2.3), and enforcing the appropriate boundary conditions where *dy/dz*, E_m, M_e and *I* define the slope of the walls centerlines at level *z* above the base, the elastic modulus of the masonry walls, the externally applied bending moment and the summation of the two individual walls' moments of inertias, respectively.

$$\frac{d^4 y}{dz^4} - (k\alpha)^2 \frac{d^2 y}{dz^2} = \frac{1}{E_m I}\left(\frac{d^2 M_e}{dz^2} - (k\alpha)^2 \frac{k^2 - 1}{k^2} M_e\right) \tag{2.3}$$

For a complete derivation of the resulting internal forces and displacements for a system of two coupled walls and coupling elements, the reader can refer to the study by Stafford Smith and Coull (1991). In Eq. 2.3, the parameter *k* is a measure of the relative flexural to axial stiffness of the walls and *α* defines the relative flexibility of the coupling slab and the walls (Harries et al. 2004) as given by Eqs. 2.4 and 2.5, respectively.

$$\alpha = \sqrt{\frac{12 I_c l_c^2}{l_c^3 h_f (I_i + I_j)}} \tag{2.4}$$

$$k = \sqrt{1 + \frac{(A_i + A_j)(I_i + I_j)}{A_i A_j l_c^2}} \tag{2.5}$$

In the Eqs. 2.4 and 2.5, l_c, h_f, A_i, A_j, I_i and I_j represent the net slab span between the walls, the center-to-center floor height, the cross-sectional area of each of the individual walls and the individual walls' moment of inertias, respectively. Finally, I_c represents the moment of inertia of the coupling slab accounting for shear deformations and is calculated by Eq. 2.6.

$$I_c = \frac{I_b}{1+\left(\dfrac{12E_c I_b}{l_c^2 G_c A_c}\lambda\right)} \tag{2.6}$$

Where, I_b, A_c, E_c, G_c and λ define the flexural moment of inertia, and cross-sectional area of the coupling slab, the elastic modulus of concrete slab, shear modulus of concrete slab and shape factor respectively. Once the k and α parameters are evaluated, the parameter C in Eq. 2.2 can be evaluated using Eq. 2.7.

$$C = \frac{\sinh(k\alpha h_w)}{(k\alpha h_w)\cosh(k\alpha h_w)} \tag{2.7}$$

Using the above formulation, the *DOC* was evaluated to be equal to 51% and 37% for Walls W3 and W4, respectively (refer to Table 2.3 for the values of the parameters used in the calculations). With the *DOC* of the walls evaluated, the theoretical predictions of V_y and V_u for the slab-coupled walls listed in Table 2.2 were obtained using the predicted values of the individual Walls, W5 and W6 respectively utilizing Eq. 2.8.

$$V_{coupled} = \frac{2\times V_{individual}}{1-DOC} \tag{2.8}$$

A simple comparison to illustrate the strength and stiffness enhancements realized by the slab-coupled walls (compared to the corresponding linked ones) is shown in Fig. 2.8(c). The numbers in the figure show that, by considering the slab coupling effects, the yield, V_y and ultimate strength, V_u of Wall 5 increased by 83.2 % and 44.9% respectively, and corresponding lateral stiffness values increased by 59% and 34%, respectively. As such, the results show that, although no special reinforcement detailing of the slabs was adopted in the current study, the slabs provided significant wall coupling that altered the walls' strength and stiffness characteristics. This in turn indicates that ignoring slab-coupling in the design of RM SFRS might lead to inaccurate estimation of the design lateral shear capacity, stiffness, and period; an issue that might need to be addressed by the MSJC and CSA S304 seismic design sub-committees. However, as only two slab-coupled walls were considered in this study, further testing of slab-coupled RM walls with different *DOC* is necessary to gain a better understanding of slab-coupled wall behaviour under different levels of seismic demands.

2.4.2 Plastic Hinge Length Idealization

A plastic hinge can be defined as the region where a structural component reaches, and maintains, its maximum flexural capacity while undergoing significant inelastic rotations (Paulay and Priestley 1992). Quantifying the extent of such a region is key for FBSD in order to facilitate predicting the wall displacement ductility as well as to define the area within the wall where special detailing might be necessary to facilitate plastic curvature development with minimal (controlled) wall damage. For the tested rectangular and flanged walls (e.g. Walls W1, W2, W5 and W6), plastic hinging would occur exclusively at the base of the walls. On the other hand, for the slab-coupled walls, the hinging mechanism depends on the *DOC* between the walls. For such walls, plastic hinging can develop at the base of the two walls and at the wall/slab interface.

In their studies, Kazaz et al. 2013, Shedid and El-Dakhakhni, 2014 highlighted the variability that exists when quantifying l_p for rectangular RM walls. In addition, there is an analytical study that have focused on evaluating the influence of connecting walls, with different cross sectional characteristics, on their plastic hinge lengths (Bohl and Adebar 2011).

Because of their nonlinear behaviour, idealizing the load displacement envelopes of RM walls is necessary to quantify their idealized plastic hinge length, $l_{p,ideal}$ based on mechanistic models. According to Tomaževič (1999), the experimental load-displacement envelopes can be idealized using three key points: (a) the point where there is a major change in the slope of the load-displacement envelope, (typically at Δ_{ym}); (b) the point representing the maximum capacity, V_u, attained during testing; and (c) the displacement at 20% peak load degradation, $\Delta_{0.8Vu}$. Tomaževič (1999) also suggested that, if the load-displacement envelope is idealized with an elastic-plastic relationship, then the idealized elastic-plastic resistance F_{ep} can be evaluated by equating the energy under the experimental load-displacement envelope to that under the idealized elastic-plastic relationship [recognizing that the yield (effective) stiffness $K_e=F_y/\Delta_y$] as shown in Eq. 2.9.

$$F_{ep} = K_e\left(\Delta_{0.8V_u} - \sqrt{\Delta_{0.8V_u}{}^2 - \frac{2\times A_{env}}{K_e}}\right) \qquad (2.9)$$

Where A_{env} is the area under the experimental load-displacement envelope up to $\Delta_{0.8Vu}$. Subsequently, the idealized plastic hinge, $l_{p,ideal}$ values (plastic hinge length assuming idealized curvature distribution along the wall's height) [Table 2.4] can be calculated by solving for $l_{p,ideal}$ in Eq. 2.10 (Paulay and Priestley 1992), utilizing the values of $\mu_{\Delta 0.8Vu}{}^{ep}$ and $\mu_\phi=\phi_u/\phi_y{}^{ep}$, presented in Table 2.4.

$$\mu^{ep}{}_{\Delta 0.8Vu} = 1 + 3\left(\mu_\phi - 1\right)\frac{l_{p,ideal}}{h_w}\left(1 - 0.5\times\frac{l_{p,ideal}}{h_w}\right) \qquad (2.10)$$

In the above equation, $\mu_{\Delta 0.8Vu}{}^{ep}$ is the idealized displacement ductility at 20% peak load degradation, ϕ_u, $\phi_y{}^{ep}$ and μ_ϕ denote the ultimate curvature, the idealized yield curvature and the curvature ductility of the walls, respectively. The curvature ductility was determined from the idealized yield curvature corresponding to the idealized yield displacement from the idealized elastic-plastic relationships depicted in Fig. 2.9. Walls W1, W2, W3, W4, with the same overall aspect ratios, showed different idealized equivalent plastic hinge lengths ranging between 0.05 l_w and 0.32 l_w [Table 2.4]. Walls W5 and W6 had $l_{p,ideal}$ values of approximately 0.26 l_w and 0.36 l_w, respectively. These values will be compared with available equivalent plastic hinge length model predictions in the next section.

2.4.3 Plastic Hinge Length Predictions

Table 2.5 shows the predicted equivalent plastic hinge length, l_p values from different plastic hinge quantification approaches including those proposed Eurocode 8 (Committee for Standardization, CEN 2005), Priestley et al. (2007) and Bohl and Adebar (2011). *Approach I*, proposed by Eurocode 8 (2005) is given by Eq. 2.11, where l_p is a function of the wall's length moment-shear ratio, l_v, vertical reinforcement diameter, d_b and its yield strength, f_y (MPa) and masonry compressive strength, f'_m in MPa.

$$l_p = \frac{l_v}{30} + 0.2 l_w + 0.11 \times \left(\frac{d_b f_y}{\sqrt{f'_m}} \right) \tag{2.11}$$

Approach II was proposed Priestley et al. (2007) and is given by Eq. 2.12, in which the plastic hinge length is influenced by the wall's length, the stain penetration length, l_{sp}, and strain hardening denoted by the strain hardening parameter r (see Eq. 2.13) where f_u is the ultimate strength of the reinforcement.

$$l_p = r.h_w + 0.1 l_w + l_{sp} \tag{2.12}$$

$$r = 0.2 \times \left(\frac{f_u}{f_y} - 1 \right) \leq 0.08 \tag{2.13}$$

Finally, Bohl and Adebar (2011) (*Approaches III*) proposed Eq. 2.14 where the plastic hinge length is function of wall's length, moment-shear ratio and axial compression.

$$l_p = (0.2l_w + 0.05l_v)\left(1 - 1.5 \times \frac{P}{A \cdot f_m^{'}}\right) \tag{2.14}$$

Where P denotes the axial load on the wall in N. The prediction results of the three different approaches presented in Table 2.5 overestimate the idealized plastic hinge length for Walls W1 and W2. The high μ_ϕ values for Walls W1 and W2 result in lower values for the idealized plastic hinge lengths. Overall, the results in Table 2.5 show that Priestley's et al. (2007) prediction is the best estimate for the plastic hinge length where the percentage difference lies between 1 to 40%. *Approach I* (Eurocode 2005) yielded the best prediction of l_p for Wall W3. Further analysis, shows that the difference between Approaches *I* and *II* is the strain hardening parameter and the moment shear ratio, while between *I* and *III* is the axial compression only. Moreover the difference between Approaches *II* and *III* is the axial compression and moment shear ratio. It can be inferred that the strain hardening parameter, which is only provided in Priestley's expression can be strongly correlated to the plastic hinge length. Axial compression effect, which is only included in Bohl and Adebar (2011) expression, does not seem to have a major effect on l_p. However, because of the limited number of walls reported in the current study, analyses of a more comprehensive experimental RM wall database are necessary to generalize such conclusions for RM walls detailed within the ductile/special RM SFRS classification.

2.4.3 Wall Ductility Quantification

Displacement ductility quantification is key to evaluate the RM walls' inelastic deformation capacities and to facilitate predicting the drift and damage levels under different levels of seismic demand (Park and Paulay 1975; Paulay and Priestley 1992; Priestley et al. 1996; Tomaževič

1999). To date, there has been no consensus amongst researchers in terms of identifying RM and RC walls' yield displacement point (Voon and Ingham 2006 and 2008, Vasconcelos and Lourenço 2009, Haach et al. 2010, Shedid et al. 2010b, Banting and El-Dakhakhni 2012). As can be observed from Fig. 2.8(a) presented earlier, none of the walls had a well-defined yield plateau that can be used to calculate the displacement ductility. As such, the equivalent elastic-perfectly plastic RM wall load-displacement idealization approach (Tomaževič 1999) of the corresponding inelastic response (Fig. 2.9) would facilitate quantifying the wall displacement ductility capacity (Vasconcelos and Lourenço 2009; Haach et al. 2010; Shedid et al. 2010b and Banting and El-Dakhakhni 2012).

The experimentally determined and the idealized displacement ductility, μ_{Δ}^{ep} values at different loading/drift levels are presented in Table 2.6. Comparing the experimental and the corresponding idealized ductility values indicates that the μ_{Δ}^{ep} values are on average 17.5% lower than the μ_{Δ} values (COV = 14.3%). In addition, the idealized wall resistance values, F_{ep}, listed in Table 2.4, were on average 90% (COV = 4%) of the experimental ultimate wall capacities, V_u, averaged from both directions.

The ductility values evaluated at maximum load, $\mu_{\Delta Vu}$, listed in Table 2.6 ranged between 1.9 and 4.3, with the highest values corresponding to the slab-coupled Walls W3 and W4. The displacement ductility values at 1% drift, $\mu_{\Delta 1\%}$ range between 1.4 and 3.6, within which Walls W1 and W2 (the most stiff walls in the test matrix) had the highest values as opposed to the slab-coupled Walls W3 and W4, which reached values of only 2.2 and 1.8 respectively. The relatively high ductility values for Walls W1 and W2 are attained due to the walls' lower yield displacements compared to those of the more flexible walls. At 20% ultimate load degradation, $\mu_{\Delta 0.8Vu}$ values ranged between 4.0 and 6.5, while the $\mu_{\Delta fr}$ values (corresponding to the fracture of the walls' outermost bars) ranged between 5.4 and 7.6, with the highest ductility values again corresponding to the slab-coupled Walls W3 and W4. The effect of slab coupling enhanced the displacement ductility at characteristic limit states. For example comparing between the displacement ductility at 20% ultimate load degradation shows that walls W3 and W4 have better performance than walls W5 and W6 by 59% and 4% respectively.

Figure 2.8(b) presented earlier shows the influence of changing the wall cross-sectional configuration on stiffness and displacement capacities. In this respect, the wall top drift capacities were compared using the corresponding $\Delta_{0.8Vu}$ and Δ_{fr} levels. At $\Delta_{0.8Vu}$, the slab-coupled Walls W3 and W4 have similar percentage drifts (for the (+) and (-) loading directions) of approximately 2.8 and 3.0, respectively. At $\Delta_{0.8Vu}$ level, the corresponding average percentage drift from Walls W3 and W4 was 87% and 76% higher than Walls W1 and W2, respectively. In addition, the top wall drifts corresponding to the Δ_{fr} were very high for the slab-coupled walls reaching 3.4%. On the other hand, the rectangular Wall W1 and the flanged Wall W2 reached only 1.8% and 2.0% drift, respectively, at the Δ_{fr} level.

Moment-curvature analysis was used along with *Approach III* (Priestley et al. 2007) to obtain the theoretical yield and ultimate displacements, presented in Table 2.6. Such values were then used to calculate the theoretical displacement ductility $\mu_{\Delta th}$, which are shown in the table and compared with $\mu_{\Delta 0.8Vuep}$ values. The idealized displacement ductility values at 20% ultimate load degradation, $\mu_{\Delta 0.8Vuep}$ were higher than $\mu_{\Delta th}$ by at least 200% for most of the walls, where the $\mu_{\Delta 0.8Vuep}$ values range between 3.4 and 5.4. The experimental ductility values corresponding to $\mu_{\Delta 1\%}$, $\mu_{\Delta 0.8Vu}$ and $\mu_{\Delta fr}$ demonstrated that RM walls detailed following the same prescriptive requirements for the ductile/special RM SFRS classification can experience significantly different ductile capabilities based on their configurations.

2.5 CONCLUSIONS

This chapter presented an experimental study on *ductile shear walls* or *special reinforced masonry walls* SFRS classification as per CSA S304-14 (CSA 2014-a) and MSJC (2013) standards, respectively. The objective of this part of the study was to evaluate key FBSD parameters of flexural dominant individual and slab-coupled RM shear walls. Quantifying such FBSD parameters would facilitate assessing whether walls with the same overall aspect ratio and detailed following the same prescriptive SFRS classification requirements, but with different cross section configurations would develop similar response under seismic events. In general, all walls showed ductile behaviour and failed in flexure. However due to the variation in their cross-section configurations, crack patterns were different, with the rectangular and flanged Walls W1 and W2 showing a combination of flexure and shear cracks. The slab-coupled Walls W3 and W4 failed by forming plastic hinges at the bottom of the two walls in addition to hinges at the wall/slab interface of the walls. Walls W5 and W6 exhibited a dominating flexural failure characterized by bed and head joint cracking, toe crushing and bar fracture at the end of the test. Based on the FBSD parameters quantification of the test walls, the following conclusions were made:

Displacement ductility capacities corresponding to different wall response levels varied when considering different wall configurations. Using elasto-plastic idealization, on average the idealized displacement ductility capacities, $\mu_{\Delta 0.8Vu}{}^{ep}$ were higher than theoretical, $\mu_{\Delta}{}^{th}$ by at least 200% for most of the walls. The values ranged from 3.4 to 5.4, indicating the variability in the ductility capacity within the walls. Utilizing the idealized load-displacement relationships, Walls W1, W2, W3 and W4 showed different idealized equivalent plastic hinge length ranging between 0.05 l_w to 0.32 l_w. Walls W5 and W6 had an $l_{p,ideal}$ value ranging between 0.26 l_w and 0.36 l_w. The theoretical values from the three different approaches presented in Table 2.5 overestimated the idealized plastic hinge length for Walls W1 and W2. The high μ_ϕ values for Walls W1 and W2 resulted in lower values for the idealized plastic hinge lengths. Overall, the results in Table 2.5 show that Priestley's et al. (2007) prediction is the best estimate for the plastic hinge length where the percentage difference lies between 1 to 40%. *Approach I* (Eurocode 2005) yielded best predictions of l_p for Wall W3. It can be inferred that the strain hardening parameter which is only provided in Priestley's expression can be strongly correlated to the plastic hinge length. Axial compression effect which is only included in Bohl and Adebar (2011) expression does not seem to have a major effect on l_p.

In conclusion, the experimental results presented in this chapter showed that RM walls designed within the same SFRS classification level could show significant difference in their load-displacement relationship characteristics and ultimate displacement ductility capacities. The seismic design process has to incorporate the difference in configuration even for walls within the same SFRS classification level to accurately predict the behaviour of walls designed and detailed for such level. Moreover, North American masonry code seismic design subcommittees might find it beneficial to consider incorporating RM slab-coupled walls, as a separate SFRS classification (similar to their corresponding RC wall counterparts), as they showed better performance than similar uncoupled walls with the same overall aspect ratio. This however would require further testing than what is presented in the current study. The next chapter will further investigate displacement- and performance-based seismic design parameters in order to gain more insight into the behaviour of ductile/special RM walls.

2.6 CHAPTER 2 NOTATION

The following symbols are used in this chapter:
A = total gross cross-sectional area of the walls (mm^2);
A_b = cross-sectional area of coupling slab (mm^2);
$A_{i,j}$ = cross-sectional area of individual wall's i and j (mm^2);
A_{env} = total area under force-displacement envelope curve (mm^2);
A_r = Aspect ratio of the walls;
A_s = cross-sectional area of tensile reinforcement (mm^2)
A'_s = cross-sectional area of compression reinforcement (mm^2)
c = neutral axis depth from compression face (mm);
C_m = compressive force of masonry (kN);
C_{PTL} = Concentrated top load factor;
C_s = compressive force of compressive steel (kN);
d_i = distance of corresponding bars i from compression face (mm);
d_b = vertical reinforcement bar diameter (mm);
DOC = degree of coupling;
E_m = Young's modulus of masonry (MPa);
E_c = Young's modulus of concrete (MPa);
F = axial force either compression or tension developed in the individual walls (kN);
f'_m = compressive strength of masonry prism (MPa);
f_y = yield stress of vertical reinforcement (MPa);
f_u = ultimate stress of vertical reinforcement (MPa);
F_{ep} = Idealized resistance of the walls using bilinear linearization (kN);
G_c = Shear modulus of coupling slab (MPa);
h_f = floor centre to centre height (mm);
h_w = Total height of the wall (mm);
I_b = flexural moment of inertia of coupling slab (mm^4);
I_c = moment of inertia of coupling slab accounting for shear deformation (mm^4);
$I_{i,j}$ = moment of inertia of individual wall's i and j (mm^4);
k = parameter that accounts for the relative flexural to axial stiffness of the walls
l_c = net span of the coupling slab (mm);
l_p = plastic hinge length of the wall (mm);
$l_{p,ideal}$ = idealized plastic hinge length of the wall (mm);
l_{sp} = tensile strain penetration length (mm);
l_v = moment-shear ratio;
l_w = length of wall (mm);
M = overturning moment in a structural wall (kN·m);
M_c = additional couple formed by axial force in a coupled wall mechanism (kN·m);
M_e = externally applied moment (kN·m);
$M_{i,j}$ = overturning moment in individual wall i and j of coupled wall system (kN·m);
M_u = ultimate moment capacity of the wall (kN·m);
M_y = yield moment capacity of the wall (kN·m);
P = axial load on the wall (kN);
r = strain hardening parameter;
T = tensile force of tension steel (kN);

t = thickness of shear wall (mm);
$V_{coupled}$ = Lateral force of the slab-coupled wall (kN);
V_{exp} = Experimental lateral force of the wall (kN);
$V_{individual}$ = Lateral force of the individual wall (kN);
V_{pred} = Theoretical lateral force of the wall (kN);
V_u = Ultimate lateral force of the wall (kN);
V_y = Lateral yield force of the wall (kN);
ϕ_y = yield curvature of the wall (mm^{-1});
Δ_{Vu} = Displacement at maximum lateral load (mm);
Δ_{fr}= Displacement at extreme bar fracture (mm);
$\Delta_{0.8Vu}$ = Displacement at 20% ultimate load degradation (mm);
$\Delta_{u,\,th}$ = theoretical ultimate displacement (mm);
$\Delta_{y,\,th}$ = theoretical yield displacement (mm);
Δ_{yep}= theoretical idealized yield displacement (mm);
Δ_{th} = theoretical yield displacement (mm);
Δ_{ym} = experimental yield displacement (mm);
$\mu_{\Delta 1\%}{}^{ep}$ = idealized displacement ductility at 1% drift limit;
$\mu_{\Delta 0.8Vu}{}^{ep}$ = idealized displacement ductility at 20% ultimate load degradation;
$\mu_{\Delta fr}{}^{ep}$ = idealized displacement ductility at extreme bar fracture;
$\mu_{\Delta}{}^{th}$ = Theoretical Displacement ductility of the shear wall;
μ_{ϕ} = Curvature ductility;
ρ_h = percent area of reinforcement in the horizontal direction (%);
ρ_v = percent area of reinforcement in the vertical direction (%);
ε_m = masonry strain;
ε_{um} = ultimate strain of masonry;
ε_y = yield strain of vertical reinforcement.
α = parameter that defines the relative flexibility of the coupling slab and the walls (mm^{-1});
β_1 = ratio of depth of compression to depth of neutral axis
λ = shape factor;
d_y/d_z = slope of the centroidal axes of the walls at level z due to bending.

2.7 CHAPTER 2 REFERENCES

Ahmadi, F., Hernandez, J., Sherman, J., Kapoi, C., Klingner, R., and McLean, D. (2014). "Seismic Performance of Cantilever-Reinforced Concrete Masonry Shear Walls." *J. Struct. Eng*.,140(9), 04014051.

ASTM CI09-08 (2008) Standard Test Method for Compressive Strength of Hydraulic Cement Mortars. West Conshohocken, PA. ASTM International.

ASTM CI019-08 (2008). Standard Test Method for Sampling and Testing Grout. West Conshohocken, PA. ASTM International.

ASTM International. (2005). ASTMEIII-04 - Standard Test Method for Young's Modulus, Tangent Modulus, and Chord Modulus. West Conshohocken, PA.

ASTM International. (2008). ASTM C140-08 - Standard Test Methods for Sampling and Testing Concrete Masonry Units and Related Units. West Conshohocken, PA.

Banting, B. R. and El-Dakhakhni, W. W. (2012). "Force- and Displacement- Based Seismic Performance Parameters for Reinforced Masonry Structural Walls with Boundary Elements." *J. Struct. Eng.*, 10.1061/(ASCE)ST.1943-541X.0000572, 1477-1491.

Banting, B. and El-Dakhakhni, W. (2014a). "Seismic Performance Quantification of Reinforced Masonry Structural Walls with Boundary Elements." *J. Struct. Eng.*, 140(5), 04014001.

Banting, B. and El-Dakhakhni, W. (2014b). "Seismic Design Parameters for Special Masonry Structural Walls Detailed with Confined Boundary Elements." *J. Struct. Eng.*, 140(10), 04014067.

Bohl, A. and Adebar, P. (2011). "Plastic hinge lengths in high-rise concrete shear walls." *ACI Structural Journal,* 10.14359/51664249, 108(2), 148-157.

Canadian Standards Association (CSA). (2014-a) "Design of masonry structures." CSA S304-14, Mississauga, Canada.

Canadian Standards Association (CSA). (2014-b). "CSA Standards on concrete masonry units." CSA A165, Mississauga, Ontario, Canada.

Canadian Standards Association (CSA). (2014-c). "Mortar and grout for unit masonry." CSA A179-14, Mississauga, Canada.

Canadian Standards Association (CSA). (2014-d). "Carbon steel bars for concrete reinforcement." CSA G30.18-09 (reaffirmed 2014), Mississauga, ON

Chitty, L. (1947). "On the cantilever composed of a number of parallel beams interconnected by cross bars." *London, Edinburgh Dublin Philos. Mag. J. Sci.,* 38, 685–699.

Eikanas, I. K. (2003). "Behaviour of concrete masonry shear walls with varying aspect ratio and flexural reinforcement." Master of Science in Civil Engineering- Thesis, Washington State University, Washington, USA.

El-Dakhakhni, W., Banting B., and Miller, S. (2013). "Seismic Performance Parameter Quantification of Shear-Critical Reinforced Concrete Masonry Squat Walls." *J. Struct. Eng.*, 139(6), 957–973.

European Committee for Standardization (CEN). (2005). "Eurocode 8: Design of structures for earthquake resistance: Part 3: Assessment and retrofitting of buildings." *BS EN 1998-3*, Brussels, Belgium.

Fattal, S. G. and Todd, D. R. (1991). “Ultimate strength of masonry shear walls: prediction vs. test results.” *NISTIR 4633*, Building and Fire Research Laboratory, Gaithersburg, USA.

Haach, V.,Vasconcelos, G., and Lourenço, P.(2010).“Experimental Analysis of Reinforced Concrete Block Masonry Walls Subjected to In-Plane Cyclic Loading.” *J. Struct. Eng*.,136(4), 452–462.

Hamid A. A., Abboud, B. E. and Harris, H. G., “Direct Modelling of Concrete Block Masonry under Axial Compression,” Masonry: Research, Application and Problems, ASTM STP 871, J. C. Grogan and J. T. Conway, Eds., American Society for Testing and Materials, Philadelphia, 1985, pp. 151-166.

Harries, K., Moulton, J., and Clemson, R.(2004). “Parametric Study of Coupled Wall Behaviour—Implications for the Design of Coupling Beams.” *J. Struct. Eng.*,130 (3), 480–488.

Harris, H. G., & Sabnis, G. M. (1999). *Structural Modelling and Experimental Techniques*, Second Edition. Boca Raton: CRC Press LLC.

Hoenderkamp.J. C. D. (2012). “Degree of coupling in high rise mixed shear wall structures.” *Indian Academy of Sciences*, August 2012, 37(4), 481-492.

Leiva G.H. (1991). “Seismic Resistance of Two Storey Masonry Walls with Openings” Ph.D. Thesis, The University of Texas , Austic, US.

Masonry Standards Joint Committee of the American Concrete Institute, American Society of Civil Engineers, and The Masonry Society (MSJC). (2013). “Building code requirements for Masonry Structures.” TMS 402-13/ASCE 5-13/ACI 530-13, Detroit, MI, New York, and Boulder, CO.

Park, R., and Paulay, T. (1975). *Reinforced concrete structures*, Wiley,New York.

Paulay T., and Priestly, M. (1992). *Seismic design of reinforced concrete and masonry buildings*, Wiley, New York.

Priestley, M. J. N. (1976). “Cyclic testing of heavily reinforced concrete masonry shear walls.” *Research Report 76-12*, Department of Civil Engineering, University of Canterbury, Christchurch, New Zealand.

Priestley, M., J., N., and Elder, D., M. (1982). “Seismic Behaviour of Slender Concrete Masonry Shear Walls.”. *Research Rep.*, University of Canterbury, Christchurch, New Zealand.

Priestley, M., J., N., and Kowalsky, M., J. (1998). “Aspects of Drift and Ductility Capacity of Rectangular Cantilever Structural Walls.” *Bulletin of the New Zealand National Society for Earthquake Engineering*, 31(2), 73-85.

Priestly, N., Calvi, G., and Kowalsky, M. (2007). *Displacement-based seismic design of structures*, IUSS Press, Pavia, Italy.

Shedid, M. (2009), “Ductility of Concrete Block Shear Wall Structures” Ph.D. Thesis, Department of Civil Engineering, McMaster University, Ontario, Canada.

Shedid, M., El-Dakhakhni, W. and Drysdale, R. (2010a). “Characteristics of Rectangular, Flanged and End- Confined Reinforced Concrete Masonry Shear Walls for Seismic Design.” *J. Struct. Eng.* 136 (12), 1471-1482.

Shedid, M., El-Dakhakhni, W. and Drysdale, R. (2010b). “Seismic Performance Parameters for Reinforced Concrete-Block Shear Wall Construction.” *J. Perform. Constr. Facil.,* 10.1061/(ASCE)CF.1943-5509.0000061, 4-18.

Shedid, M. T., El-Dakhakhni, W. W., and Drysdale, R. G. (2010c). “Alternative strategies to enhance the seismic performance of reinforced concrete-block shear wall systems.” *J. Struct. Eng.*, 10.1061/(ASCE)ST.1943-541X.0000164, 676–689.

Shedid, M. and El-Dakhakhni, W. (2014). "Plastic Hinge Model and Displacement-Based Seismic Design Parameter Quantifications for Reinforced Concrete Block Structural Walls." *J. Struct. Eng.*, 140(4), 04013090.

Stafford Smith, B. and Coull, A. 1991 *Tall building structures – analysis and design,* New York: Wiley Interscience.

Tomaževič, M. (1999). *Earthquake resistant design of masonry buildings,* Imperial College Press, London.

Vasconcelos, G., and Lourenço, P. B. (2009), "In-Plane Experimental Behaviour of Stone Masonry Walls under Cyclic Loading." *J. Struct. Eng.*, (135)10, 1269-1277.

Table 2.1: Wall Details and Specification

Wall	Configuration	Height (mm)	Overall length (mm)	Overall aspect ratio	Vertical reinforcement	Horizontal reinforcement		CSA S304-14 classification	MSJC-13 classification
					ρ_v (%)	ρ_{h1}* (%)	ρ_{h2} ** (%)		
W1	Rectangular	2160	1533	1.4	0.6	0.26	0.14	Ductile	Special
W2	Flanged	2160	1533	1.4	0.6	0.26	0.14	Ductile	Special
W3	Coupled I	2160	1533	1.4	0.6	0.26	0.14	Ductile	Special
W4	Coupled II	2160	1533	1.4	0.6	0.26	0.14	Ductile	Special
W5 [a]	Rectangular	2160	598	3.6	0.6	0.26	0.14	Ductile	Special
W6 [b]	Rectangular	2160	465	4.6	0.6	0.26	0.14	Ductile	Special

a – W5 is the individual wall of the coupled wall system W3

b – W6 is the individual wall of the coupled wall system W4

***ρ_{h1} – Horizontal reinforcement ratio in the first storey**

****ρ_{h2} – Horizontal reinforcement ration in the second storey**

Table 2.2: Summary of Walls, Predicted, Experimental and Idealized Loads

Wall	**Predicted V_y (kN)**	**Experimental V_y (kN)**		**Predicted V_u (kN)**	**Experimental V_u (kN)**		V_{ym}/V_{yp}	V_{um}/V_{up}
		(+ve)	**(-ve)**		**(+ve)**	**(-ve)**		
W1	55.5	65.9	68.0	83.3	90.5	81.2	1.2	1.0
W2	87.1	90.1	98.4	114.6	118.5	116.0	1.1	1.0
W3	38.4	33.8	34.0	52.7	41.2	43.4	0.9	0.8
W4	19.2	22.3	20.2	26.7	28.3	26.5	1.1	1.0
W5	9.4	9.9	8.6	14.1	15.5	13.7	1.0	1.0
W6	6.3	6.8	7.7	8.8	9.9	8.8	1.2	1.1

Table 2.3: Significant Parameters for *DOC* Calculations

Parameters	Wall W3	Wall W4
l_c (mm)	935	1070
I_b (mm^4)	8.1E+06	8.1E+06
I_c (mm^4)	6.9E+06	7.7E+06
α (mm^{-1})	8.8E-04	6.5E-04
k	1.0	1.0
$k\alpha h_w$	2.0	1.4
$M_{i,j}$ (kN.m)	30.4	19.0
F (kN)	67.9	20.9
DOC	0.51	0.37

Table 2.4: Wall Idealized Ultimate Load, Experimental Displacements and Idealized Plastic Hinge Lengths

Wall	Loading direction	Idealized F_{ep} (kN)	F_{ep}/V_u (%)	Theoretical displacement (mm)		Experimental displacement (mm)		Idealized displacement ductility	Curvature ductility	$l_{p,\ ideal}$ (mm)	$l_{p,\ ideal}/l_w$ (%)
				Δ_{yth}	Δ_{uth}	Δ_{ym}	$\Delta_{0.8Vu}$	$\mu_{\Delta 0.8Vu}{}^{ep}$	$\mu_{\phi}\ (\phi_u/\phi_y{}^{ep})$		
W1	+ve	83.2	91.9	5.7	9.7	6.0	35.2	4.6	4.6	191.1	12.5
	-ve	71.8	88.4			6.4	29.1	4.3	4.3		
W2	+ve	112	94.5	5.7	37.5	6.8	40.5	4.7	4.7	83.0	5.4
	-ve	107.3	92.5			7.1	30.1	3.9	3.9		
W3	+ve	34.8	84.6	11.5	26.7	10.8	55.6	5.0	5.0	484.3	31.6
	-ve	39.3	90.5			9.5	62.0	5.7	5.7		
W4	+ve	25.1	88.6	11.7	25.8	13.8	61.2	3.9	3.9	278.4	18.2
	-ve	25.1	94.5			10.9	66.2	4.9	4.9		
W5	+ve	13.4	86.5	14.7	21.3	9.5	37.6	2.9	2.9	153.1	25.6
	-ve	12.4	90.4			10.1	56.4	3.9	3.9		
W6	+ve	9.1	92.1	18.7	28.3	13.8	59.7	3.2	3.2	167.6	36.0
	-ve	7.5	84.9			15.7	78.6	5.2	5.2		

Table 2.5: Equivalent Plastic Hinge Predictions

Walls	**Length**	l_p **(mm)**			l_p/l_w **(%)**			$l_p/\ l_{p,\ ideal}$		
		Appr. I **Eurocode (2005)**	***Appr. II*** **Priestley et al. (2007)**	***Appr. III*** **Bohl & Adebar (2011)**	***Appr. I*** **Euroco de (2005)**	***Appr. II*** **Priestley et al. (2007)**	***Appr. III*** **Bohl & Adebar (2011)**	***Appr. I*** **Eurocode (2005)**	***Appr. II*** **Priestley et al. (2007)**	***Appr. III*** **Bohl & Adebar (2011)**
W1	1533	400.8	270.5	304.8	26.1	17.6	19.9	2.1	1.4	1.6
W2	1533	400.8	270.5	304.6	26.1	17.6	19.9	4.8	3.3	3.7
W3	1533	400.8	270.5	305.3	26.1	17.6	19.9	0.8	0.6	0.6
W4	1533	400.8	270.5	305.6	26.1	17.6	19.9	1.4	1.0	1.1
W5	598	213.9	177.0	120.4	35.8	29.6	20.1	1.4	1.2	0.8
W6	465	187.4	163.7	94.4	40.3	35.2	20.3	1.1	1.0	0.6

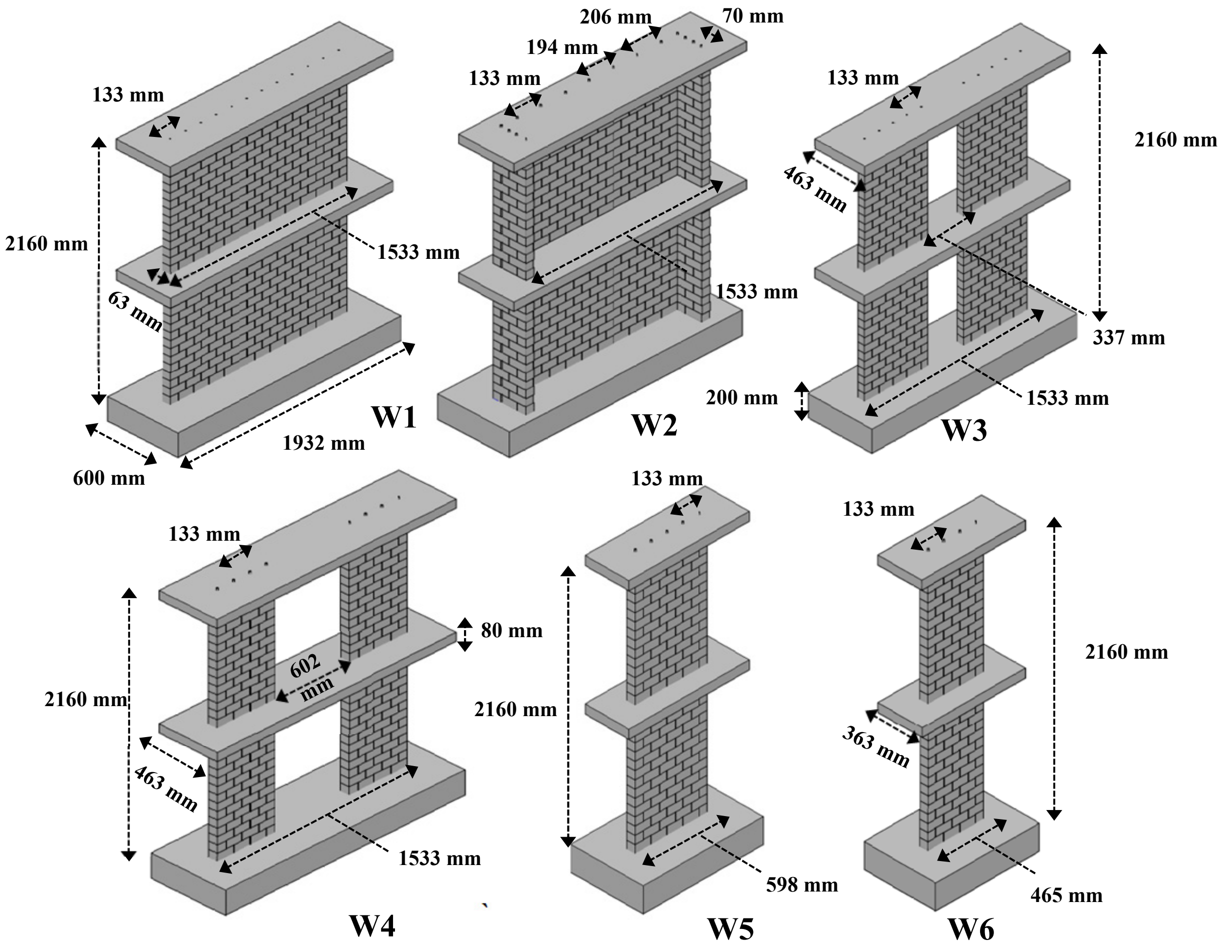

Fig. 2.1. Walls dimensions

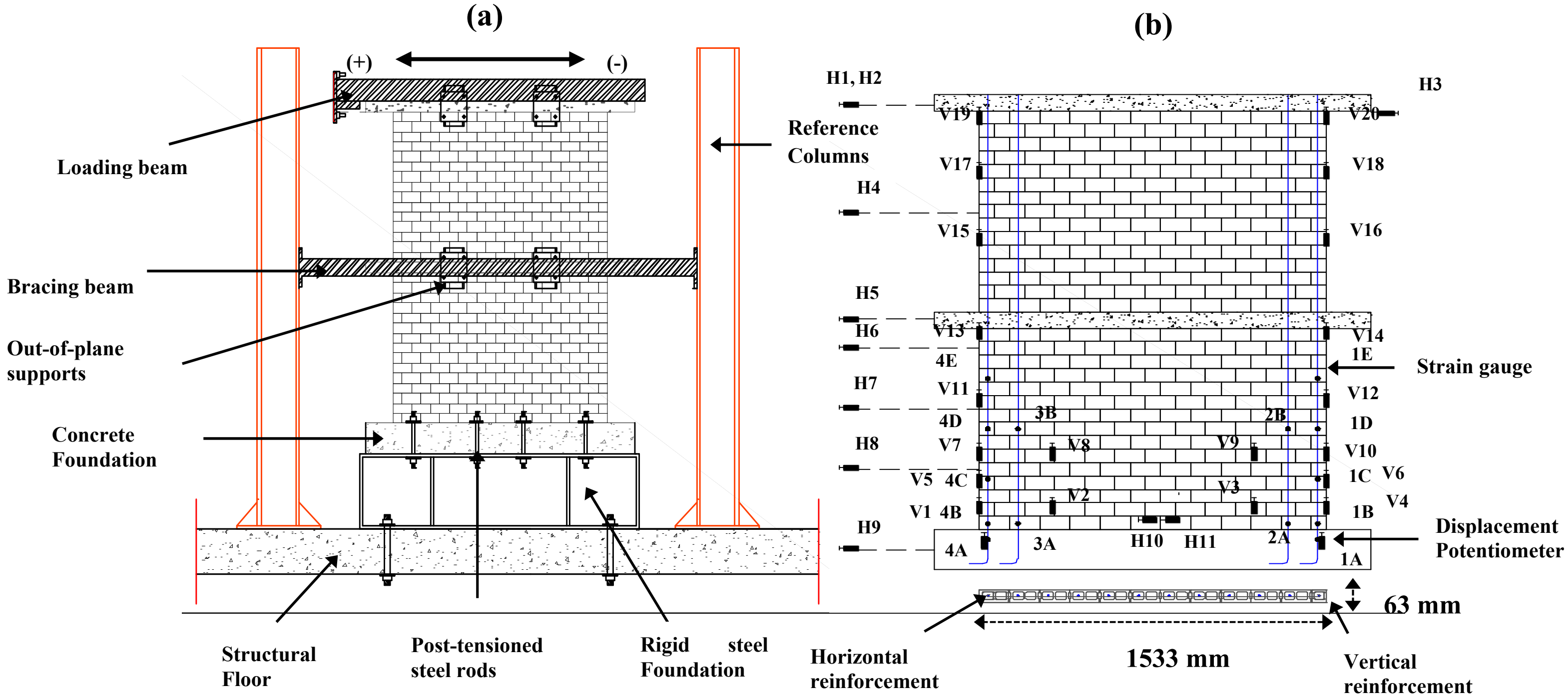

Fig. 2.2. Test setup; (a) Layout (b) External and internal instrumentation

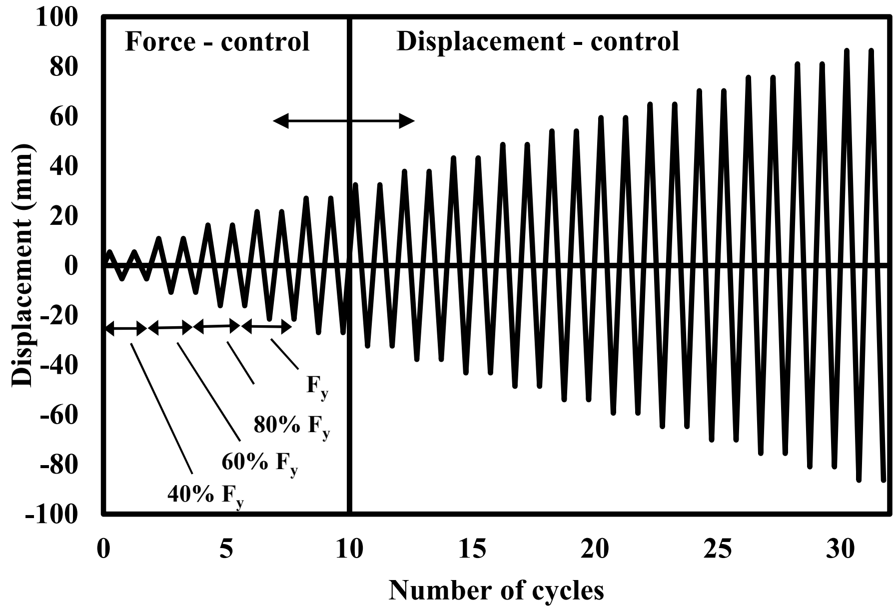

Fig. 2.3. Sample loading history for Wall W1

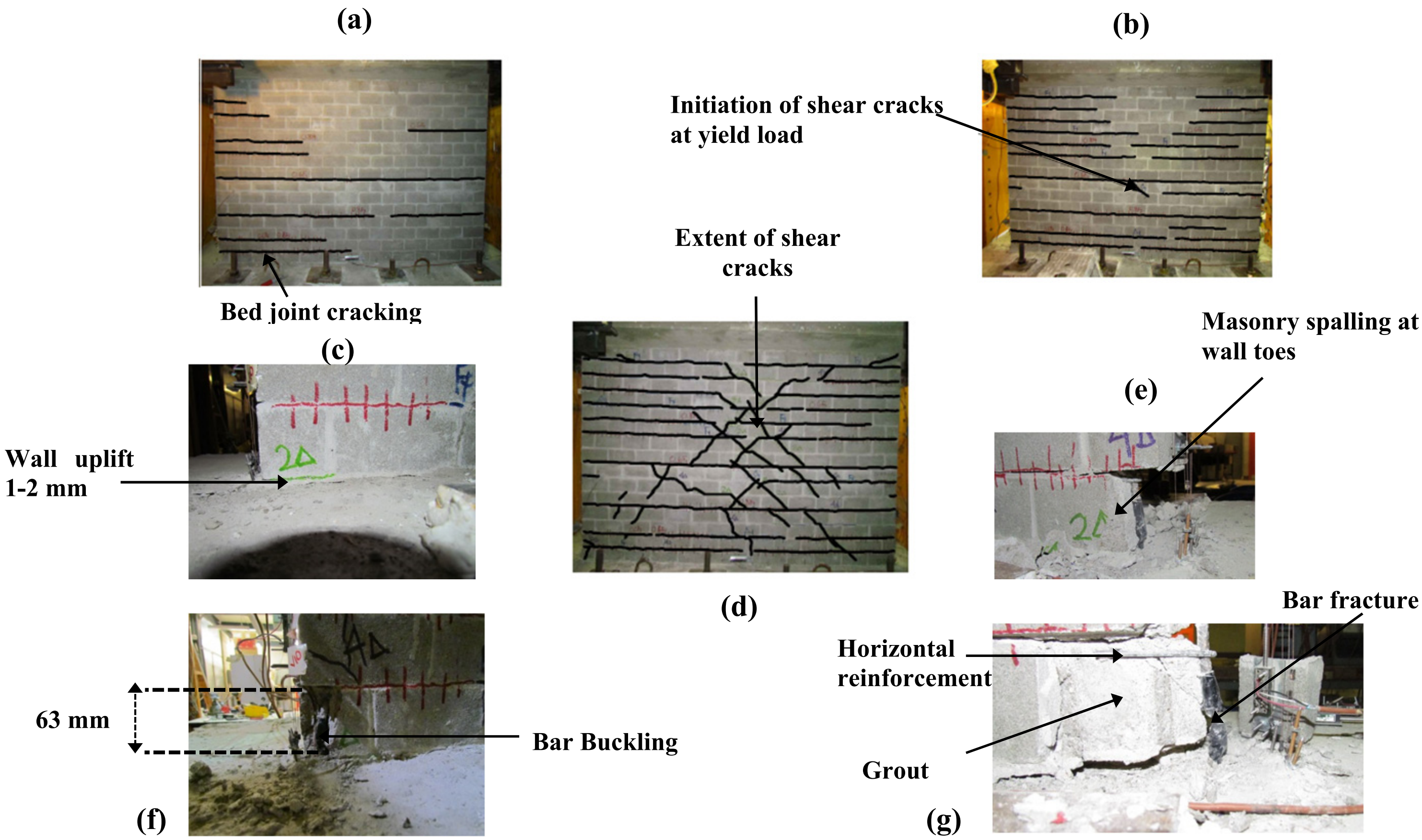

Fig. 2.4. Damage sequence of Walls W1 and W2 at % top wall drift: (a) 0.07%; (b) 0.3%; (c) 0.6%; (d) 0.6%-1.9%; (e) 1.2%-1.5%; (f) 1.5%; (g) 1.8%-2%

(a)

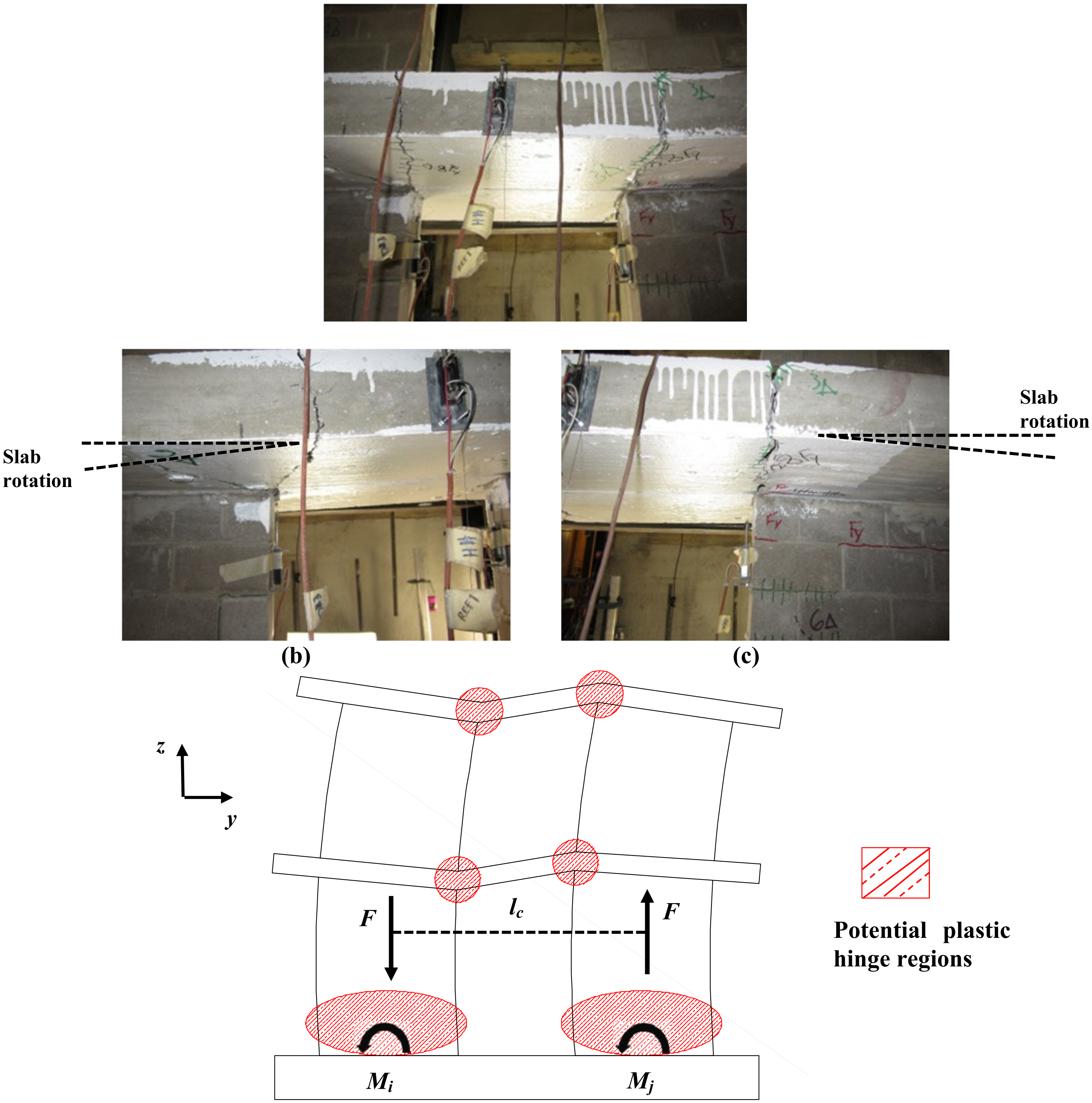

(d)

Fig. 2.5. Weak beam/strong pier failure mechanism; (a) Slab rotation; (b) West slab interface; (c) East slab interface; (d) Slab-coupled wall mechanism due to horizontal lateral load

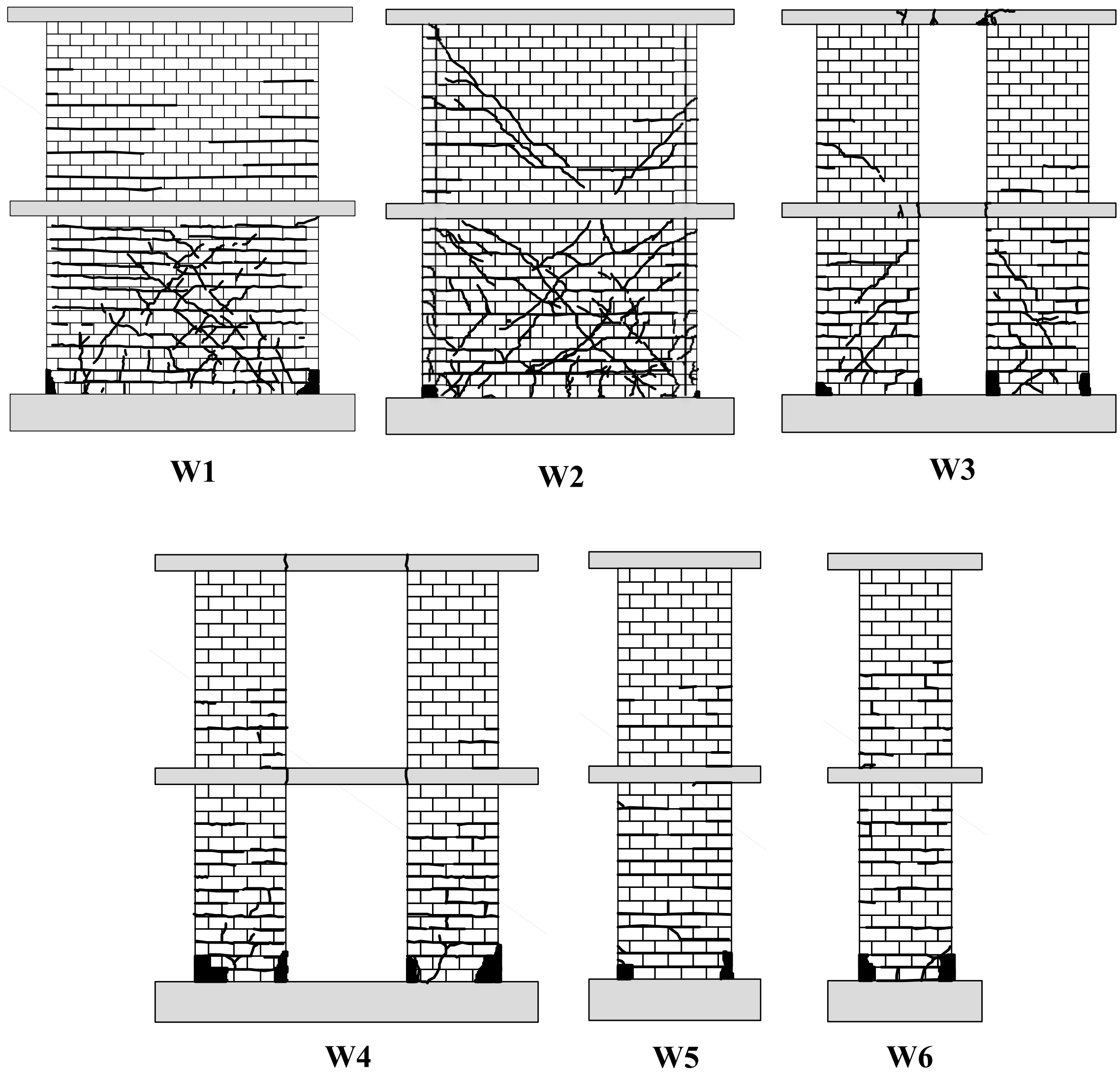

Fig. 2.6. Wall crack patterns at 20% peak strength degradation

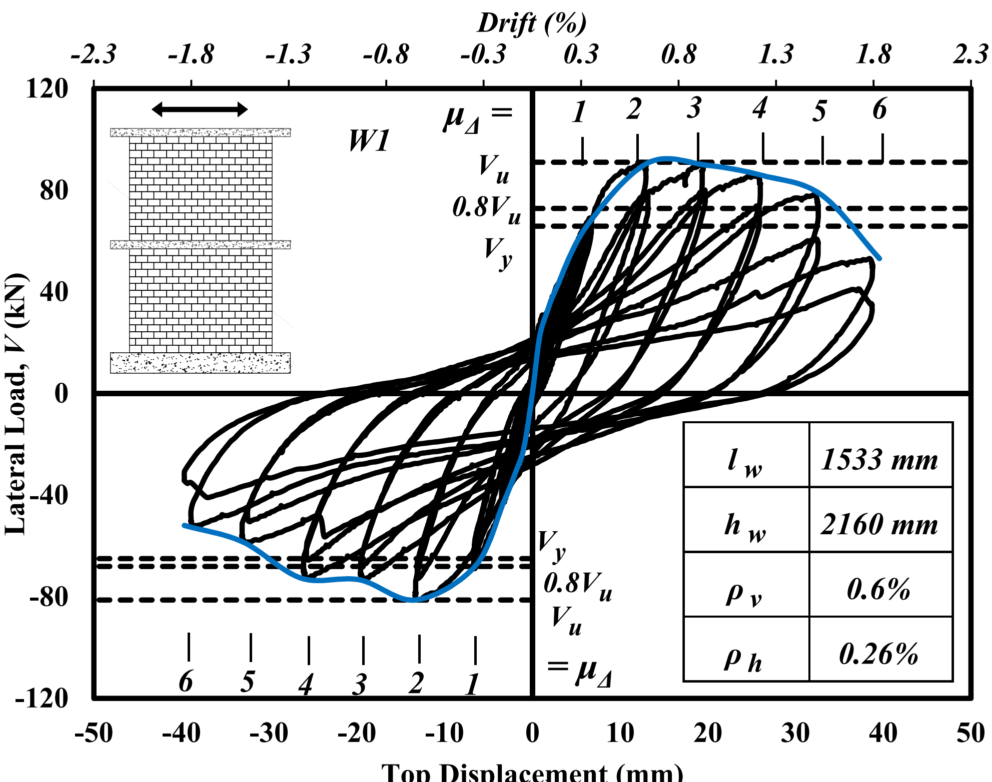
Drift (%)
-2.3 -1.8 -1.3 -0.8 -0.3 0.3 0.8 1.3 1.8 2.3
W1
μΔ =
1 2 3 4 5 6
Vu
0.8Vu
Vy
Lateral Load, V (kN)
120 80 40 0 -40 -80 -120
Vy
0.8Vu
Vu
= μΔ
6 5 4 3 2 1
lw 1533 mm
hw 2160 mm
ρv 0.6%
ρh 0.26%
-50 -40 -30 -20 -10 0 10 20 30 40 50
Top Displacement (mm)

(a)

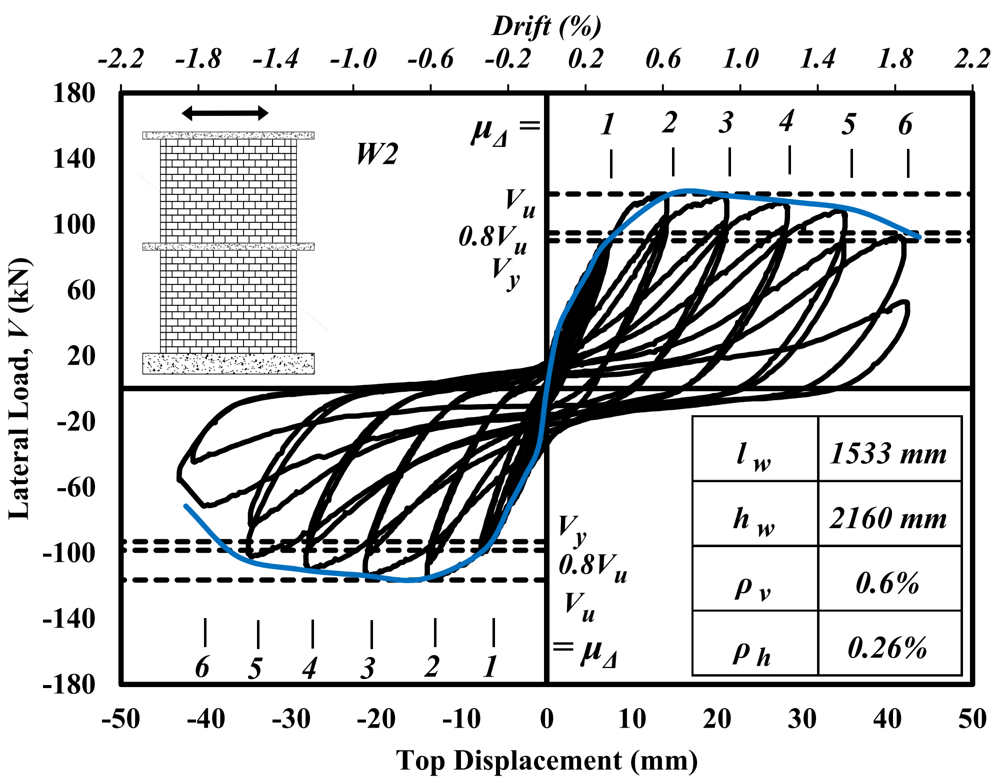
Drift (%)
-2.2 -1.8 -1.4 -1.0 -0.6 -0.2 0.2 0.6 1.0 1.4 1.8 2.2
W2
μΔ =
1 2 3 4 5 6
Vu
0.8Vu
Vy
Lateral Load, V (kN)
180 140 100 60 20 -20 -60 -100 -140 -180
Vy
0.8Vu
Vu
= μΔ
6 5 4 3 2 1
lw 1533 mm
hw 2160 mm
ρv 0.6%
ρh 0.26%
-50 -40 -30 -20 -10 0 10 20 30 40 50
Top Displacement (mm)

(b)

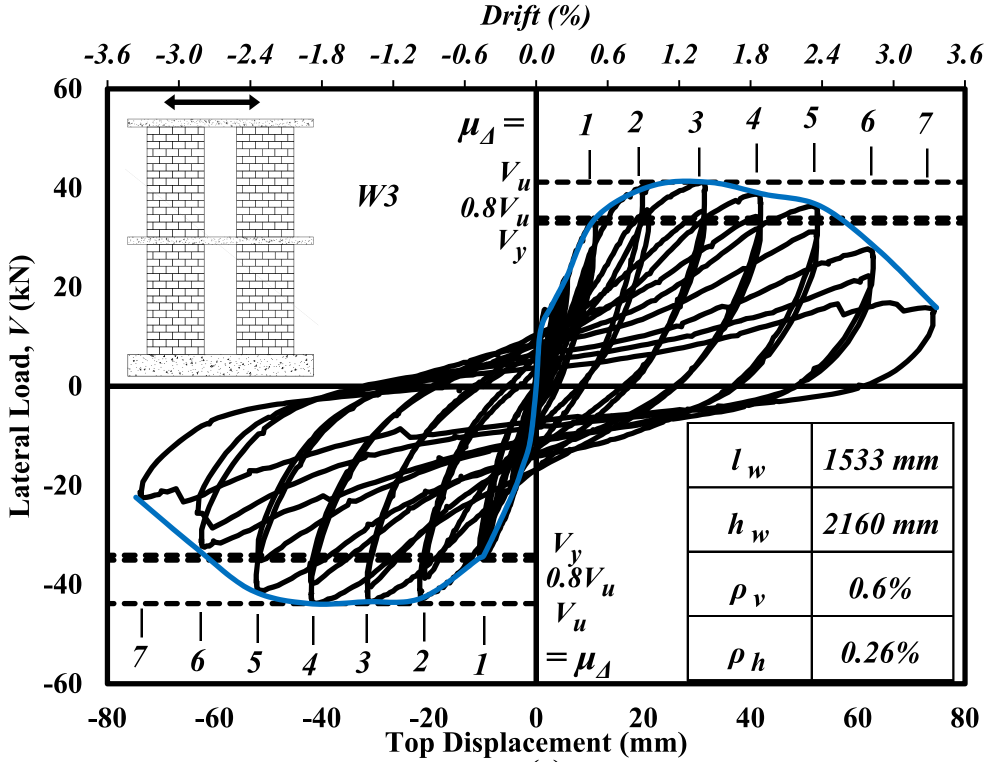
Drift (%)
-3.6 -3.0 -2.4 -1.8 -1.2 -0.6 0.0 0.6 1.2 1.8 2.4 3.0 3.6
W3
μΔ =
1 2 3 4 5 6 7
Vu
0.8Vu
Vy
Lateral Load, V (kN)
60 40 20 0 -20 -40 -60
Vy
0.8Vu
Vu
= μΔ
7 6 5 4 3 2 1
l w | 1533 mm
h w | 2160 mm
ρ v | 0.6%
ρ h | 0.26%
-80 -60 -40 -20 0 20 40 60 80
Top Displacement (mm)

(c)

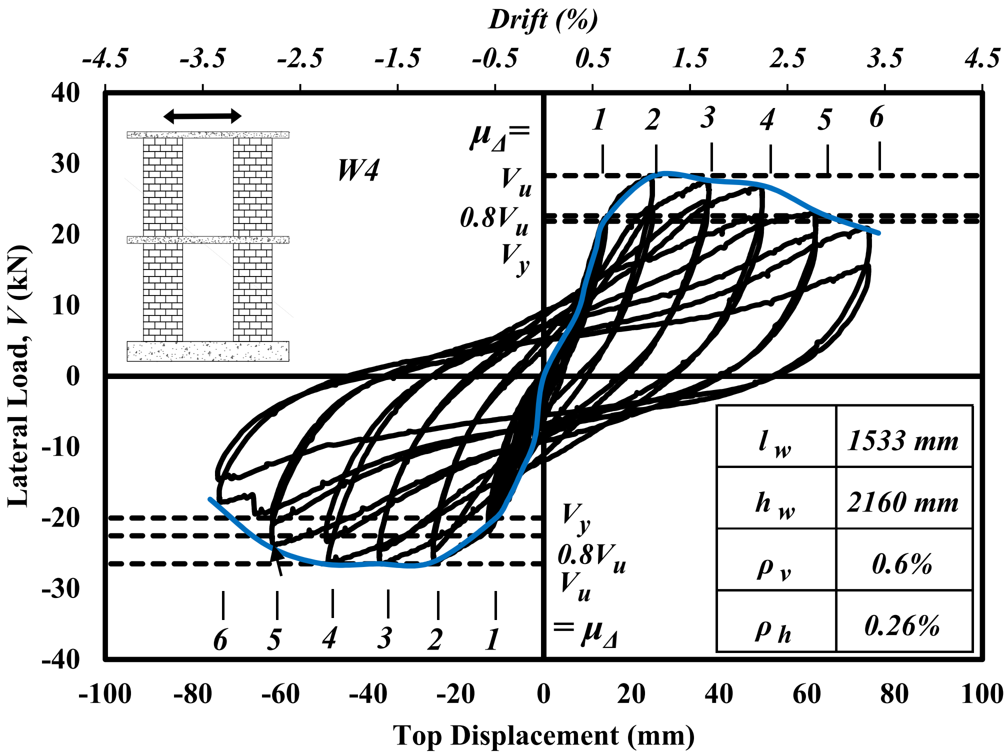
Drift (%)
-4.5 -3.5 -2.5 -1.5 -0.5 0.5 1.5 2.5 3.5 4.5
W4
μΔ=
1 2 3 4 5 6
Vu
0.8Vu
Vy
Lateral Load, V (kN)
40 30 20 10 0 -10 -20 -30 -40
Vy
0.8Vu
Vu
= μΔ
6 5 4 3 2 1
l w | 1533 mm
h w | 2160 mm
ρ v | 0.6%
ρ h | 0.26%
-100 -80 -60 -40 -20 0 20 40 60 80 100
Top Displacement (mm)

(d)

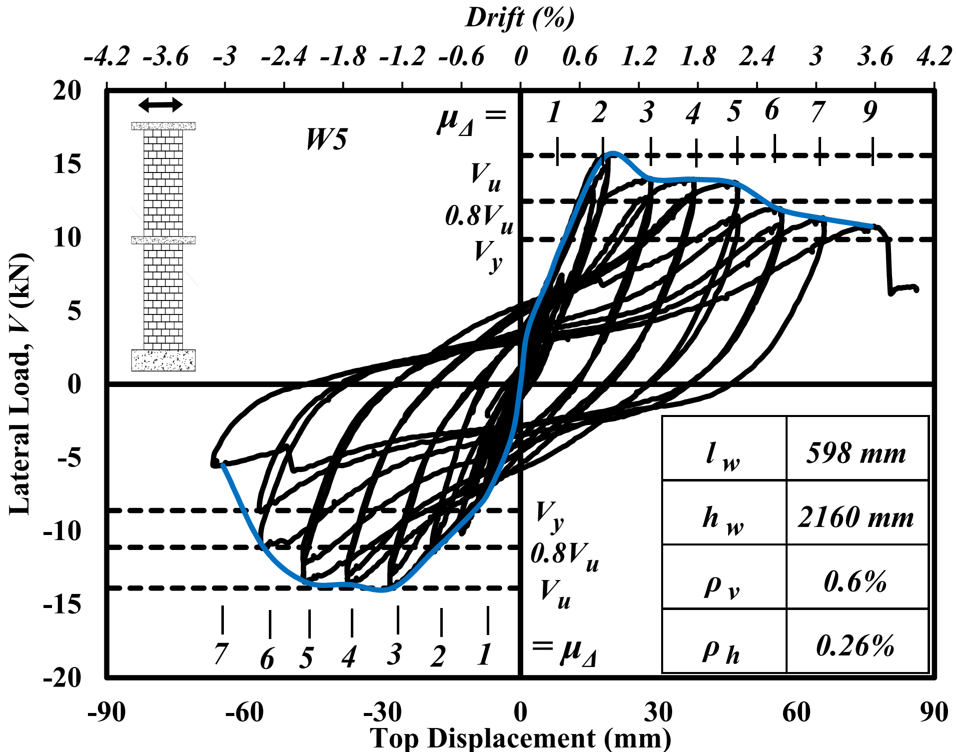

(e)

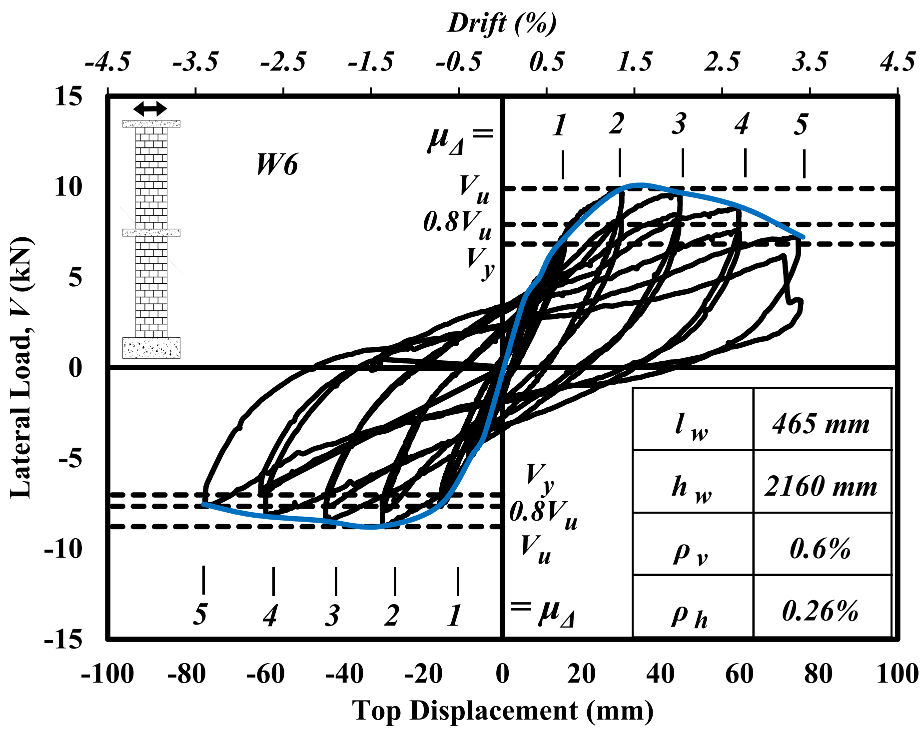

(f)

Fig. 2.7. Load-Displacement relationships: (a) W1; (b) W2; (c) W3; (d) W4; (e) W5; (f) W6

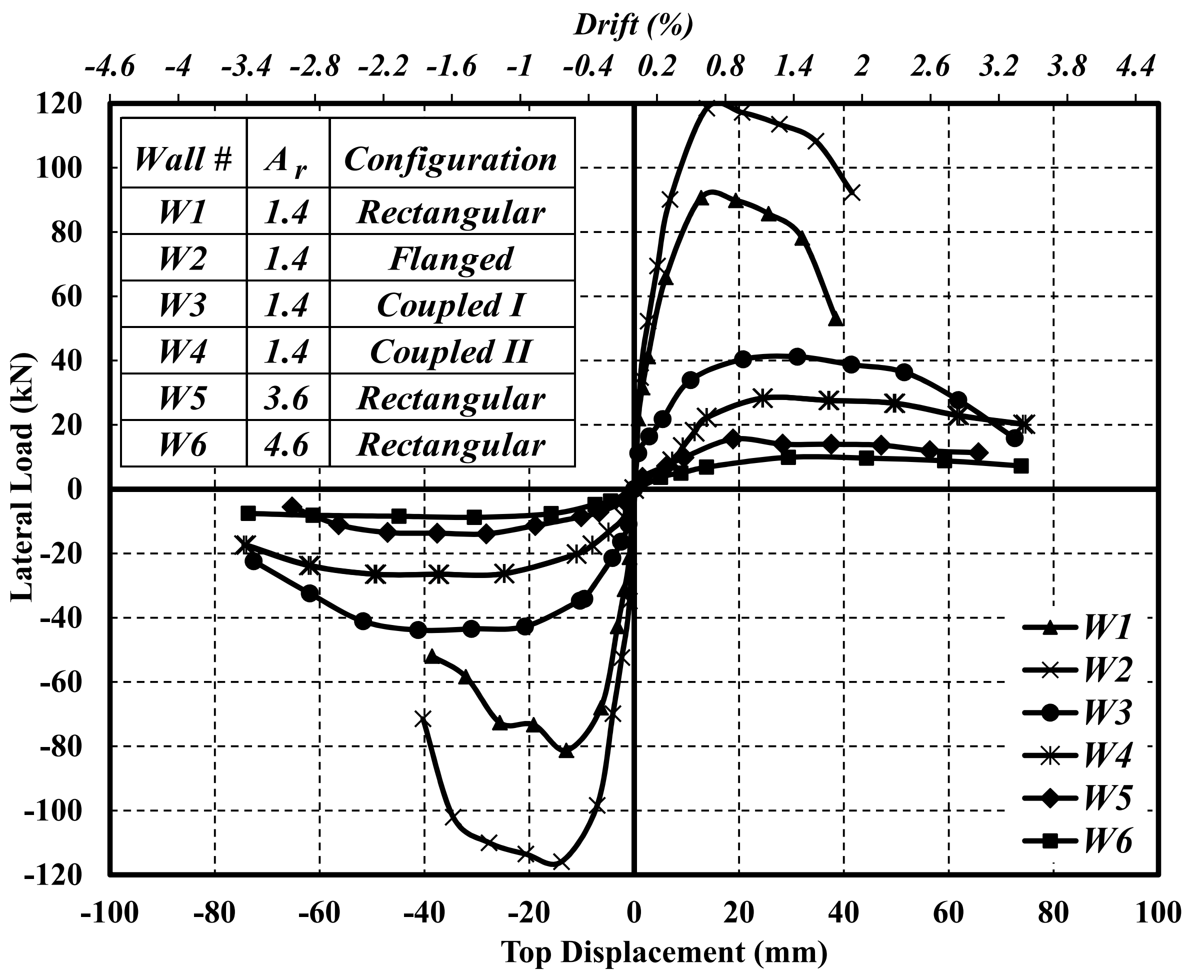

Drift (%)
-4.6 -4 -3.4 -2.8 -2.2 -1.6 -1 -0.4 0.2 0.8 1.4 2 2.6 3.2 3.8 4.4
Lateral Load (kN)
120
100
80
60
40
20
0
-20
-40
-60
-80
-100
-120
Wall # | A r | Configuration
W1 | 1.4 | Rectangular
W2 | 1.4 | Flanged
W3 | 1.4 | Coupled I
W4 | 1.4 | Coupled II
W5 | 3.6 | Rectangular
W6 | 4.6 | Rectangular
W1
W2
W3
W4
W5
W6
-100 -80 -60 -40 -20 0 20 40 60 80 100
Top Displacement (mm)

(a)

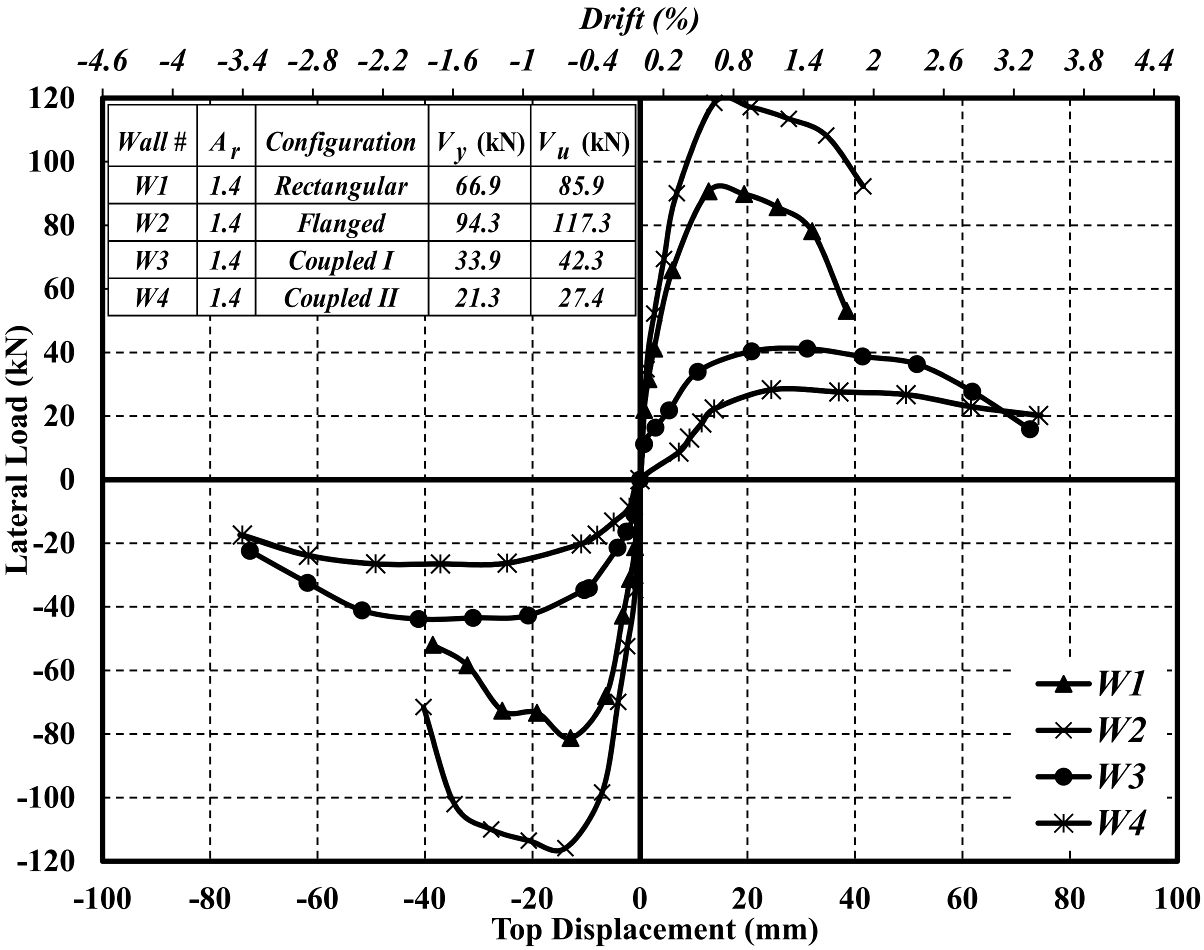

Wall #	A_r	*Configuration*	V_y (kN)	V_u (kN)
W1	*1.4*	*Rectangular*	*66.9*	*85.9*
W2	*1.4*	*Flanged*	*94.3*	*117.3*
W3	*1.4*	*Coupled I*	*33.9*	*42.3*
W4	*1.4*	*Coupled II*	*21.3*	*27.4*

(b)

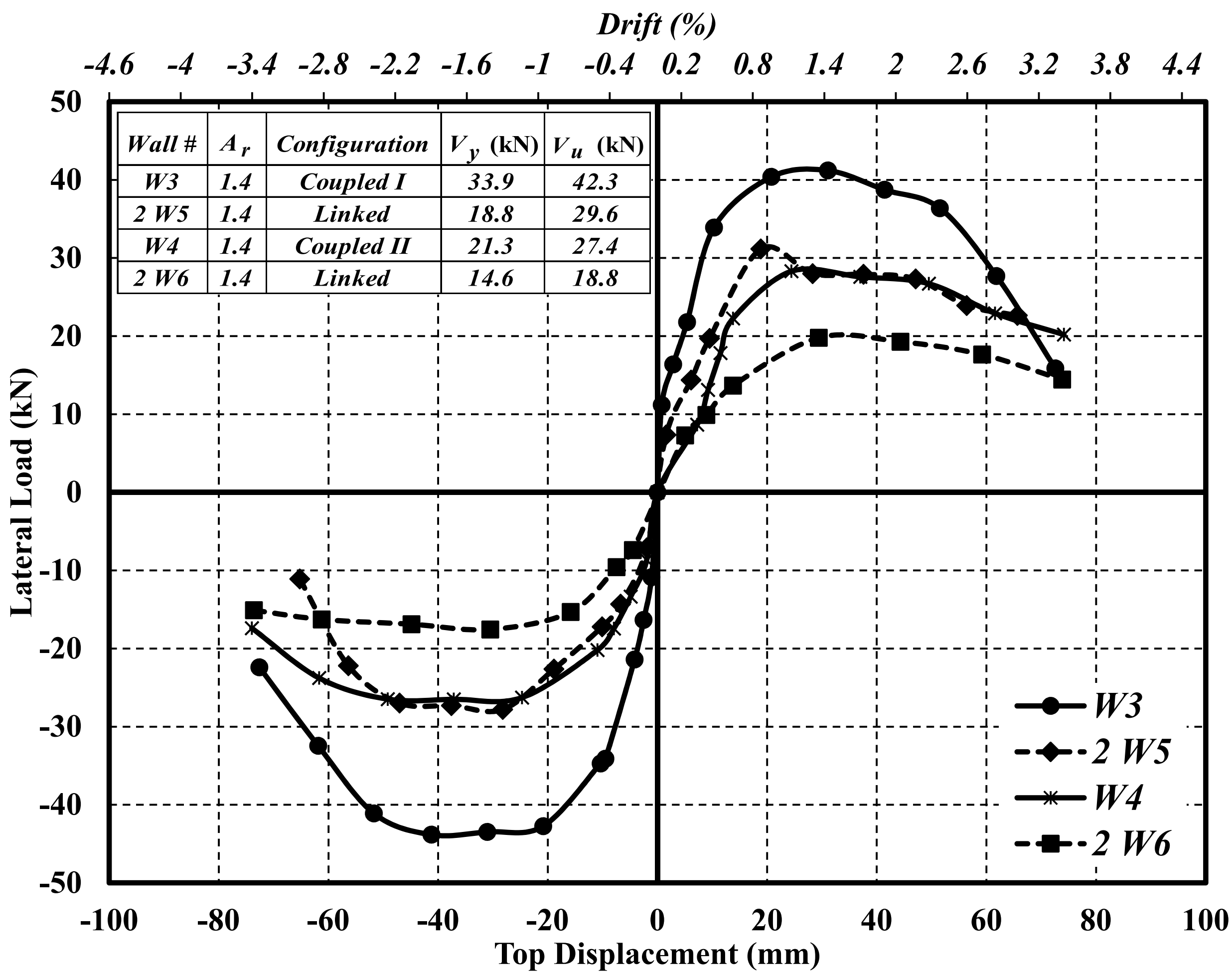

(c)

Fig 2.8. Load-Displacement envelopes: (a) All the walls; (b) Walls with same overall aspect ratio; (c) Slab-coupled and linked walls

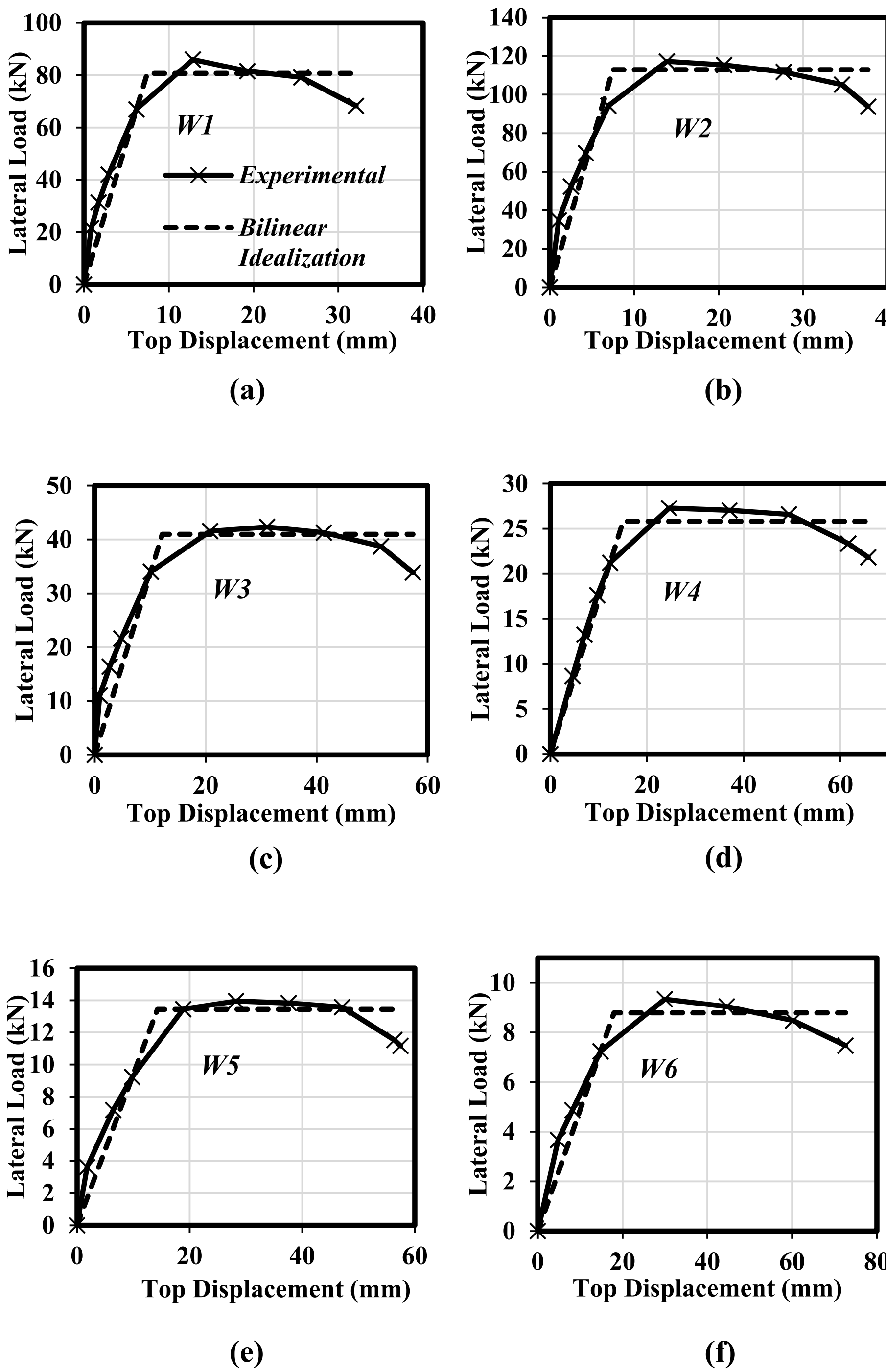

Fig 2.9. Average load displacement envelopes and bilinear idealization curves: (a) W1; (b) W2; (c) W3; (d) W4; (e) W5; (f) W6

CHAPTER 3: SEISMIC RESPONSE EVALUATION OF DUCTILE REINFORCED CONCRETE BLOCK STRUCTURAL WALLS. II: DISPLACEMENT AND PERFORMANCE-BASED DESIGN PARAMETERS

ABSTRACT: A typical seismically designed reinforced masonry building is comprised of structural walls, that are constructed following the same prescriptive detailing requirements corresponding to a code classified seismic force resisting system (SFRS). However, due to architectural requirements (i.e. to allow for openings and wall intersections, etc.), some of these walls might have the same overall aspect ratio but differ in their cross section configurations. The previous chapter presented the experimental results and force-based seismic design parameters for walls that fall under the CSA S304-14 (CSA 2014) *ductile shear walls* and the MSJC-13 (TMS-402/ACI-530/ASCE-5) *special reinforced walls* SFRS classifications. The current chapter utilizes the experimental results to extract key displacement-based seismic design parameters, including wall yield and ultimate curvatures, wall displacements at yield and at the post-yield stages, stiffness degradation, period elongation and equivalent viscous damping. The chapter also identified different damage states and linked them to wall drift levels, as well as the extent of plasticity within the wall base region as key performance-based seismic design parameters. The study showed that, using a mechanics-based approach, the curvature ductility values were at least double the theoretical code values predicted for most walls. In addition, within the same SFRS classification, walls having the same overall aspect and reinforcement ratios will possess significantly different displacement-based seismic design parameters which would subsequently influence their predicted response under seismic events. Moreover, the results showed that slab-coupled masonry walls showed an enhanced overall performance compared to the rectangular and flanged walls tested. Subsequently, it is suggested that future editions of the CSA S304 and MSJC account for the effects of varying the wall cross section and slab coupling influence on the seismic response of ductile/special walls SFRS classifications.

KEYWORDS: Cyclic loading, Displacement-based design, Ductility, Performance-based design, Reinforced Masonry, Seismic response, Slab-coupled, Structural wall.

3.1 INTRODUCTION

Concrete block structural walls comprise the main components of reinforced masonry building seismic force resisting systems (SFRS). In typical building designs, due to architectural requirements, the walls might possess the same overall aspect ratio but have different cross section configurations. However the ductility capacity of the masonry SFRS and, therefore, its components (i.e. the structural walls) depends on the reinforcement ratios, axial load and the component cross section (Priestley, 2000). As such, assigning the same displacement ductility capacity values for each SFRS classification, as is currently implied in North American codes using ductility-related force reduction factors, might result in inconsistent response predictions (Priestley et al., 2007). Similar conclusions were highlighted in the previous chapter (Siyam et al. 2015a) which showed that reinforced masonry (RM) shear walls designed within the same SFRS classification can exhibit significant variations in key force-based seismic design parameters (FBSD). In this respect, the details of the walls tested by Siyam et al. 2015a place them under the *ductile shear walls* and the *special reinforced masonry walls* SFRS classifications according to the Canadian S304-14 (CSA 2014) and American (MSJC 2013) masonry codes, respectively.

The focus of the current chapter is to quantify key displacement-based seismic design (DBSD) and performance-based seismic design (PBSD) parameters for the RM walls reported in the previous chapter. The DBSD parameters studied include walls' curvatures, displacements at yield and post-yield stages, displacement ductility, stiffness degradation and period of vibration elongation in addition to the equivalent viscous damping. In addition, the PBSD aspects included identification of damage states and their linkage to wall drift levels, as well as the extent of plasticity and crack patterns at the corresponding damage states.

PBSD adopts a system-level performance quantification approach, where previous and recent test results on masonry systems (Seible et al. 1991, Stavridis et al. 2011) have indicated that floor diaphragms induce system-level effects, such as slab-coupling of shear walls, which can play a significant role in determining the overall behaviour of the SFRS. In this respect, the study by Beyer (2005) concluded that wall base shear seismic demands are significantly influenced by the wall-to-slab degree of coupling. In addition, White and Adebar (2004) analyzed the behaviour of reinforced concrete shear walls coupled by beams (with varying heights and degrees of coupling) and showed that wall beam-coupling can significantly influence the wall base rotations and their top displacement demands. Finally, Lehman et al. (2013) experimentally investigated the response of mid-rise coupled walls with specially reinforced coupling beam designed to meet code requirements and demonstrated the importance of analyzing coupled walls as a system in order to accurately quantify their structural response and failure mechanisms.

Although wall coupling effects have been recognized for some time, currently, North American masonry design standards: Canadian Standards Association "Design of Masonry Structures" S304-14 (CSA 2014) and the TMS 402-13/ACI 530-13/ASCE 5-13 Masonry Standards Joint Committee code (MSJC 2013) do not specify design guidance for reinforced masonry (RM) shear walls coupled by concrete slabs or place them within a separate SFRS classification. Although concrete block masonry coupling beams can be used to create masonry moment-resisting frame SFRS (NRCC, 2010; Paulay and Priestley 1992), construction of such SFRS is limited due to practical considerations. In this respect, it should be noted that reinforced concrete (RC) coupling beams typically rely on special diagonal and confinement reinforcement details in order to effectively couple RC walls while minimizing the beam damage under the corresponding force and displacement demands. However, this typical RC coupling beam detailing is impractical to adopt in RM beams constructed using standard concrete masonry units because of the units' geometry (i.e. the webs and the limited grout cell size). One alternative would be to utilize deep lintel units and to place a reinforcement cage in the formed beam after the units are laid; however such uncommon approach is rarely considered in design offices or in job sites because of the associated labor costs and construction time. It should also be noted that, when masonry beams are utilized (e.g. to span openings), the common construction practice would be to introduce movement joints on the beam interface(s) with the wall, and subsequently wall coupling would not develop. In addition, steel angles or precast concrete beams are typically used to span openings and carry only gravity loads rather than providing wall coupling elements per se. The next section will first present a brief summary of the experimental program and test results reported in the previous chapter.

3.2 SUMMARY OF EXPERIMENTAL PROGRAM AND TEST RESULTS

The experimental program focused on evaluating the seismic response of six, fully-grouted, RM shear walls subjected to reversed cycles of quasi-static loading. The walls were constructed using one-third scale blocks measuring 130 mm in length, 63 mm in width and 63 mm in height simulating the standard 390 mm x 190 mm x 190 mm stretcher units used in North America. Four of the walls (W1, W2, W3, and W4) have the same (overall) aspect ratios but different cross section configurations, with Wall W1 being rectangular, Wall W2 being flanged and Walls W3 and W4 being two slab-coupled systems (made up of two individual walls each). In order to facilitate comparison, Walls W5 and W6 are constructed and tested as they represented the individual components of the slab-coupled wall systems, Walls W3 and W4, respectively. In this respect, the response of two-linked Walls W5 can represent that of Wall W3 with a very flexible/weak slab coupling and the same for Wall W6 with respect to the slab-coupled Wall W4. Details of all the walls' dimensions, aspect ratios and steel reinforcement ratios are presented in Table 3.1, in which the vertical and horizontal steel ratios, and the vertical and horizontal bar diameters are denoted by, $\rho_{v,}$ $\rho_{h,}$ d_v and d_h, respectively. In general, the experimental results showed that the tested RM walls failed in a flexural manner reaching an experimental displacement ductility level, at 20% ultimate strength degradation, between 4.0 and 6.5. The results also showed that RM shear walls detailed following the same SFRS classification requirements, and having the same overall aspect ratio, but with different cross section configurations, might exhibit significantly different FBSD parameters.

3.3 DISPLACEMENT-BASED SEISMIC DESIGN PARAMETERS

3.3.1 Wall Curvatures

Wall cross section curvature is an important DBSD parameter as it directly influences the wall's ability to develop inelastic flexural rotations and a plastic hinge mechanism. Within the context of DBSD, prediction of yield and ultimate curvatures is key for quantifying the yield and ultimate displacement capacities of SFRS components (Priestley et al. 2007). The theoretical and experimental values of the yield (ϕ_y) and the ultimate (ϕ_u) curvatures for all the walls are provided in Table 3.2. The values of the theoretical curvatures at yield and ultimate listed in Table 3.2 were calculated using two methods: a mechanics based method (*Method I*) and an empirical method proposed by Paulay (2002) (*Method II*) as will be explained next.

Method I (Mechanics-based)

Method I uses first principles by adopting the flexural beam theory and the plane sections assumption as given by CSA S304-14 (CSA 2014). The theoretical yield curvature is defined as the curvature when the wall outermost reinforcement bar reaches the yield strain ε_{sy} = 0.0025 and is calculated by $\phi_{y,th1} = \varepsilon_{sy} / (d - c_y)$. The theoretical ultimate curvature is defined as $\phi_{u,th1} = \varepsilon_u / c_u$ where the ultimate strain in the masonry is taken as ε_u = 0.0033 in accordance to ultimate strains obtained from experimental testing of prism columns (Appendix A, Fig A-1). The symbols d, c_y and c_u represent the distance from the top fiber to extreme tensile reinforcement, the neutral axis depth at yield, and the neutral axis depth at ultimate, respectively. Curvature analysis of the slab-coupled Walls W3 and W4 involve proportioning the yield curvature of the individual wall after evaluating each wall's degree of coupling (*DOC*), evaluated in the previous chapter as 51% and 37%, corresponding to Walls W3 and W4, respectively. Consequently, the wall yield and ultimate curvatures corresponding to the total overturning moment, $\phi_{th1,cw}$ is calculated using Eq. 3.1 as described by Priestley et al. (2007) where $\phi_{y,u}$, denotes the yield and ultimate curvature, respectively, of the individual wall. Sample calculations of the yield and ultimate curvatures are presented in the Appendix F.

$$\phi_{th1,cw} = \frac{\phi_{y,u}}{1 - DOC} \tag{3.1}$$

Method II (Paulay 2002)

As an alternative to *Method I* above, Paulay (2002) proposed evaluating the yield curvatures using the empirical formula, $\phi_{y,th2} = \eta \varepsilon_y / l_w$. The formula shows that the yield curvature can be estimated using a coefficient of dimensionless curvature, $\eta = \left(M_n / M_y \right) / \left(1 - c / l_w \right)$ which accounts for the ratio of the nominal-to-yield moments (M_n/M_y)

and the relative position to the neutral axis (1-c/l_w). As such, the formula relates the yield curvature of a shear wall to its length, l_w and yield strain of the flexural reinforcement, ε_y. The corresponding c/l_w and η values for four tested walls are given in Table 3.3. The ultimate theoretical curvature formula given by Eq. 3.2 is developed using the tensile strain limits for the vertical reinforcement determined to be the point of the steel strain hardening (10% strain) obtained from direct tensile experimental tests of the vertical reinforcement.

$$\phi_{u,th2} = \frac{0.072}{l_w} \tag{3.2}$$

It was assumed that, towards the ultimate stage, and after the coupling slab failure, the ultimate curvatures of the slab-coupled walls would be the same as that of two separate cantilever walls connected through link members. This was validated using experimental curvature derivation near the end of the testing at a top displacement of $5\Delta_y$ where the ultimate curvature in Wall W3 was 1.25×10^{-4} rad/mm as compared to the ultimate curvature of 1.70×10^{-4} rad/mm for Wall W5. Similarly at $4\Delta_y$ displacement level, ultimate curvature in Wall W4 was 0.44×10^{-4} compared to the ultimate curvature of 1.76×10^{-4} for Wall W6.

Experimental Curvature and Comparison with Theoretical Curvatures

Applying a top load on a RM wall system results in an experimental curvature profile presented schematically in Fig. 3.1. The experimental curvatures are calculated through the vertically mounted displacement potentiometers (DP) along the wall heights (Fig. 3.1) using Eq. 3.3.

$$\phi_{\exp} = \frac{\Delta_{Ti} + \Delta_{Ci}}{h_{gauge(i)} \times l_w} \tag{3.3}$$

Where: ϕ_{exp} = average curvature over a given segment along the wall height in rad/mm; Δ_{Ci} = compression displacement measurement at the compression side of the wall in mm; Δ_{Ti} = tensile displacement measurement on the tension side of the wall in mm; $h_{gauge(i)}$ = wall segment height in mm corresponding to the Δ_{Ci} and Δ_{Ti} measurements.

The experimental curvature values calculated using Eq. 3.3 are presented in Table 3.2 for the bottom 100 mm wall segment. In addition, values of curvature ductility (μ_ϕ) have been calculated as $\mu_\phi=\phi_u/\phi_y$ (Table 3.2) for each of the theoretical and experimental curvature values. The experimental yield curvatures were calculated at the onset of yielding of the outermost reinforcement. Whereas, the ultimate curvatures were obtained from measurements taken during the $5\Delta_y$ displacement cycle except for Wall W5, for which the measurements at $4\Delta_y$ was considered as a result of the masonry spalling at this displacement level. A simplified approach was used for the curvature measurements of the slab-coupled Walls W3 and W4, where the individual wall curvatures were averaged to facilitate comparison with other walls of the same overall aspect ratio.

The results presented in Table 3.2 indicate that using *Method I* underestimates curvature values over the bottom 100 mm segment length. In *Method I*, an ultimate masonry strain of ε = 0.0033 was used for the ultimate curvature calculations. The ultimate curvature values in the Table 3.2 would have been higher if the code defined ultimate strain of 0.0025 was used, leading to inaccurate curvature values. Similar observations were reported by Shedid et al. (2010-b) where higher ultimate strain values corresponded to higher curvatures, and thus better agreements with the experimental results. On the other hand, *Method II* shows that yield curvature can be estimated fairly accurately from the coefficient of dimensionless curvature (which consider yield and ultimate moments capacities of the walls), yield strain of the vertical reinforcement and length of the walls. Moreover, there is a good agreement (≤ 20%) between the ultimate curvature and the experimental results, when the steel hardening strain value was used in the calculation. The average curvature ductility values based on the experimental displacement measurements for the bottom 100 mm wall segments varied between 8.2 and 30.2. The experimental values for curvature ductility were at least double the corresponding theoretical values for most walls. The slab-coupled Walls W3 and W4 show almost twice the ultimate curvatures when compared to Walls W1 and W2 with the same overall aspect ratio.

The variation in the experimental results indicates the influence of the wall cross-section configuration on the wall curvature ductility capacity. The highest discrepancy between *Method I* and the experimental curvature ductility values were for Wall W1 (230% increase), Wall W5 (200%) and Wall W6 (240%). By contrast, using *Method II*, the yield and ultimate curvature values were similar to the experimental results leading to more accurate curvature ductility predictions. Since the curvature and the displacement ductility values are directly related, inaccurate prediction of the curvature ductility will subsequently lead to inaccurate estimation of wall's displacement ductility capacity; a key parameter in DBSD.

3.3.2 Wall Displacements at Yield and at the Post Yield Stage

The theoretical yield and post-yield displacement predictions, shown in Table 3.4, were derived using two methods as will be explained in the following sections.

Method A (Priestley et al. 2007)

Method A is based on moment-curvature analysis assuming an elastic-plastic relationship of the reinforcement including the effect of tensile strain penetration in the foundation (Priestley et al. 2007; Shedid et al. 2010a, Shedid and El-Dakhakhni 2014). The yield and ultimate displacements for the rectangular and the flanged walls are discussed first followed by the slab-coupled walls. For the rectangular and flanged walls, Eqs. 3.4 and 3.5 were used to calculate the yield, Δ_{y1}, and ultimate, Δ_{u1}, displacements, respectively after utilizing the values of the strain penetration length, l_{sp}, in mm ($l_{sp} = 0.022 \times f_{ye} \times d_{bl}$), (Priestley et al., 2007), the plastic hinge length, l_p, in mm, ($l_p = 0.2\times\left(f_u/f_y - 1\right) \times h_w + 0.1l + l_{sp}$), and the yield and ultimate curvatures using *Method II*, $\phi_{y,th2}$ and $\phi_{u,th2}$, respectively.

$$\Delta_{y1} = \frac{\phi_{y,th2}(h_w + l_{sp})^2}{3} \tag{3.4}$$

$$\Delta_{u1} = \Delta_{y1} + \Delta_{p1} = \Delta_{y1} + (\phi_{u,th2} - \phi_{y,th2})l_p h_w \tag{3.5}$$

The yield displacement at the top level, h_w for the slab-coupled walls can be estimated from moment-area analysis using Eq. 3.6 (Priestley et al. 2007).

$$\Delta_{y1,cw} = \left(\frac{0.175}{1-DOC} - \left(\frac{DOC}{1-DOC}\right) \times \left(\frac{0.1225 + 0.188n}{n}\right)\right)\phi_y h_w^2 \tag{3.6}$$

As shown in Table 3.4, the values of 11.5 mm and 11.7 mm were obtained for the yield displacements of Walls W3 and W4, respectively. The predictions range between - 12.7% lower and - 6% higher than the corresponding experimental values, respectively, indicating good agreement (< 15%) with the experimental results.

In terms of the ultimate displacement predictions of the slab-coupled walls, the ultimate displacement capacity might be governed by three limiting scenarios (cases) as described by Priestley et al. (2007): the wall base strain (Eq. 3.7), the code limitation on wall drift at the contra-flexure height (H_{CF}) (Eq. 3.8), and the strains in the coupling elements (Eq. 3.9), respectively. Subsequently, the case that yields the least displacement would govern the displacement capacity of the slab-coupled shear wall system.

Case I: *Wall Base Strain Case*:

$$\Delta_{D\varepsilon} = \Delta_{y1} + (\phi_{ls} - \phi_{y,th2})l_p h_w \tag{3.7}$$

Case II: *Wall Drift Limit Case*: $$\Delta_{D\theta} = \Delta_{y1} + (\theta_C - 0.5\phi_{y,th2} H_{CF}) h_w \quad (3.8)$$

Case III: *Coupling Beam Material Strain Limit*: $$\theta_{CS,ls} = \frac{0.6\varepsilon_{su} \times 2 l_{SP}}{0.75 h_{CS}}; \theta_{W,CS} = \frac{\theta_{CS,ls}}{1 + l_w / l_{cs}} \quad (3.9)$$

Where: ϕ_{ls}, θ_C, $\theta_{CS,ls}$ and $\theta_{W,ls}$ indicate the curvature limit corresponding to a specific wall response level, the design standard rotation (drift) limit, the coupling slab rotation, and the critical wall rotation, respectively. The CSA S304-14 (CSA 2014) adopts a value of 0.025 as a limit for inelastic rotational capacity for the *ductile* RM walls SFRS classification (i.e. θ_C = 0.025).

For *Case I* (Eq. 3.7), to control wall damage, the wall curvature was limited to the value resulting from $\phi_{ls} = 0.072/l_w$ as described earlier. The displacements determined from *Case I* were 46.6 mm and 53.4 mm for Walls W3 and W4, respectively. Using the expression of *Case II* (Eq. 3.8), the displacements for Walls W3 and W4 were determined to be 47.0 mm and 44.3 mm, respectively. Finally, for *Case III* (Eq. 3.9), the slab limiting strain was obtained from the tensile testing of the D4 bars used for the slab reinforcement which yielded at an average value of ε_{su} = 0.09 (Appendix A). Using Eq. 3.9, the ultimate displacements at the limiting slab steel strain were found to be 46.2 mm and 72.6 mm for Walls W3 and W4, respectively. From the above three scenarios, the predictions of *Cases II* and *III* (44.3 mm and 46.2 mm) would govern the ultimate displacements of Walls W3 and W4, respectively.

Method B (Effective Stiffness)

Method B involves yield and ultimate displacement predictions, Δ_{y2} and Δ_{u2}, respectively, calculated by dividing the effective stiffness and stiffness at ultimate load values by the theoretical yield and ultimate forces (V_y and V_u, respectively) obtained from flexural analysis.

The effective stiffness values (assuming cantilever free end condition) presented in Table 3.5 were calculated using the effective moment of inertia, I_e, the effective area, A_e, the elastic modulus E_m, the shear modulus, G_m and the wall cross section shape factor, k taken as 1.2 for all walls for simplicity (see Eq. 3.10).

$$K_e = \frac{1}{\frac{h_w^{\ 3}}{3E_m I_e} + \frac{k \cdot h_w}{G_m A_e}} \tag{3.10}$$

Except that for the slab-coupled walls, I_e and A_e are calculated by multiplying the gross stiffness, I_g, and cross-sectional area, A_g, by a factor α (see Eq. 3.11), following the CSA S304-14 (CSA 2014), where P_s denotes the axial load acting on the wall considering seismic load case in building codes, A_g is the gross cross-sectional area, f_y is the yield stress of the reinforcement and f'_m is the masonry compressive strength.

$$\alpha_1 = 0.3 + \frac{P_s}{f'_m A_g} \leq 1.0 \tag{3.11}$$

As the above CSA S304-14 (CSA 2014) formulation assumes individual (uncoupled) wall behaviour, the formulation proposed by Paulay (1981) for slab-coupled shear walls (where, due to coupling, one wall can experience tension while the other experiences compression) will be considered for Walls W3 and W4 as follows:

Walls subjected to axial tension:

$$I_e = 0.5I_g ; A_e = 0.5A_g \tag{3.12}$$

Walls subjected to axial compression

$$I_e = 0.8I_g ; A_e = A_g \tag{3.13}$$

Coupling slabs:

$$I_e = \frac{0.2 I_g}{\left(1 + 3(t / l_c)^2\right)} \tag{3.14}$$

Where: t is the slab's thickness and l_c is the coupling slab net span. These effective moments of inertias were used to quantify the K_e values presented in Table 3.5. The predicted values were higher than the K_{ey} values by 259% and 144% for Walls W3 and W4, respectively.

Decoupling of Wall Displacements

It is well understood that structural walls typically exhibit a combination of flexural, shear and sliding displacements under in-plane lateral loads. Flexural displacements can be obtained based on mechanics by integrating the curvatures of the cross sections along the height of the wall. Experimentally, wall base sliding can be obtained directly from the measurements of the displacement potentiometer placed at the bottom of the wall near the wall-foundation interface. As such, by subtracting the flexural and sliding displacements (Massone and Wallace 2004) from the overall wall top displacement, the shear displacements might then be decoupled. Overall, the sliding displacements at wall yield and ultimate loads were insignificant, when compared to flexural and shear displacements, ranging between 0.6% and 5%, and 0.7% and 6%, respectively. A summary of the measured yield and ultimate displacements after decoupling the flexure, and shear displacements at yield and ultimate is given in Table 3.4.

The percentage of flexural displacements at yield, Δ_{ym} and ultimate conditions, Δ_{um}, are also given in Table 3.4, respectively. The stiffer Walls W1 and W2, reached 60% and 62% on average of their experimental yield displacement by flexural dominated mechanism, respectively. The rest of the experimental total top displacement was attributed to diagonal shear (35% and 33%) and sliding (5%). The contribution of flexural displacements to the total top displacement at yield of the slab-coupled walls system was recorded to be an average 90% and 79% for Walls W3 and W4, respectively. For such walls, the yield displacement was defined when the strain in the extreme reinforcement for the wall subjected to axial tension reached a value of 0.0025. This was useful in terms of comparing the response of the slab-coupled Walls W3 and W4 to that of their corresponding individual components Walls W5 and W6.

As shown in Table 3.4, the ratio of flexural-to-overall displacement at yield, Δ_{fy} is lower in the rectangular, Wall W1, and the flanged Wall W2, compared to the slab-coupled Walls W3 and W4. The slab coupled walls and their counterparts Walls W5 and W6 responded predominantly in flexural deformations, such that Δ_f was calculated to be on average 90%, 79%, 75% and 87% of the total wall top displacement at yield, respectively. The percentage flexure for a slab-coupled wall was computed by taking the average flexural displacement of the individual walls' displacements. Using such methodology has overestimated the flexure displacement at yield for slab-coupled walls W3.

At the ultimate loads, the shear contributions to the overall wall top displacement became more evident for the flanged Wall W2 and the slab-coupled Walls W3 and W4 and were 41%, 32% and 43%, respectively. As the slab-coupled Walls W3 and W4, reached their ultimate loads the extent of plasticity reached a plateau and the increased displacement cycles led to a behaviour similar to their individual components (i.e. Walls W5 and W6). Whereas for Walls W5 and W6, the percentage flexural displacement increased to more than 84%. In such walls, the contribution of shear deformation is minimal (less than 8%) which was supported by the lack of diagonal cracks. Figure 3.2 illustrates the decoupled hysteretic load-displacement plots of each wall where the three plots in each row represent the displacement components in flexure, shear and sliding for each wall.

In Fig. 3.3, the normalized lateral load was plotted against the percentage top drift. In the same figure, the 2.5% drift limit set for collapse prevention of structures according to the National building code of Canada, NBCC (NRCC, 2015) was used to compare between the walls. Despite having the same overall aspect ratio, the slab-coupled Walls W3 and W4 attained higher average drift capacities up to 3.4% top drift and exhibited reduced yield stiffness when compared to Walls W1 and W2 as indicated in Fig. 3.3. Walls W3 and W4 were capable of reaching, and sometimes exceeding, the drift capacities of Walls W5 and W6 but at a higher lateral load capacity than twice that of their corresponding individual wall components. The slab-coupled walls formed plastic hinges at wall-slab interface which acted as a linked member at later loading stages. As expected, the lateral load capacity of the slab-coupled Walls W3 and W4 fall between twice their corresponding individual components (Walls W5 and W6) and Walls W1 and W2. At 20% peak load degradation only the slab-coupled Walls W3, W4 and its individual components, Wall W6 exceeded the 2.5% drift limit as illustrated in Fig. 3.3. On the other hand Walls W1 and W2 experienced 20% peak load degradation at drift level of 1.5% and 1.7% respectively, which is below the above limit for collapse prevention (NRCC, 2015).

Comparisons between Theoretical and Experimental Wall Displacements

Based on the results highlighted in the previous sections it can be concluded that *Method A* underestimates the yield displacement predictions for the walls with high lateral stiffness (i.e. Wall W1 and W2) by 9% and 63%, respectively, predicts well the slab-coupled walls where percentage difference is below 13%, and overestimates Δ_{y1} for Walls W5 and W6 by 50% and 28%, respectively. At ultimate load, the method does not accurately predict top displacement for Walls W1, W2, W3 and W4 (percentage difference of 33%, 169%, 36% and 40%, respectively).

Nevertheless, *Method A* showed good agreement for Walls W5 and W6 (≤ 15%) when compared to the corresponding experimental displacements at ultimate, Δ_{um}.

Method B showed more consistency in predicting the yield displacements where maximum percentage difference of 32% resulted for the flanged Wall W2. In addition, Δ_{y2} is also overestimated by approximately 14% and 4% for Walls W5 and W6 respectively, compared to the experimental values. For the ultimate displacements, *Method B* demonstrates good predictions of Walls W1 and W2 (≤ 21%) displacements and less accurate predictions for Walls W5 and W6 as indicated in Table 3.4.

The experimental displacements at 20% ultimate load degradation and at bar fracture were significantly higher than Δ_{u1} and Δ_{u2} due to excessive shear and sliding deformations at such displacement levels which are not accounted for, neither in *Method A* nor in *Method B*. However, the theoretical displacements predicted using *Method B* indicate approximately 30% difference when considering the flexural component of the displacement at 20% peak strength degradation. In addition, both methods do not accurately predict the displacement at 20% load degradation for the slab-coupled walls although the limiting strain expression (Eq. 3.2) was utilized. In summary, the CSA S304-14 (CSA 2014) definition of effective moment of inertia (*Method B*) yields consistently more accurate results (≤ 21%, ≤ 14% difference) for the stiffer walls ultimate displacement predictions and the slender walls yield predictions, respectively, compared to the model proposed by Priestley et al. 2007 (*Method A*). However, *Method A*, provides better displacement predictions for the slab-coupled walls' and slender walls' ultimate displacements. In conclusions, moment curvature idealization is a good methodology for predicting ultimate displacements for slender walls but not for the stiffer walls. The rationale lies in the fact that the idealization in Priestley's (et. al 2007) method does not account for coupled shear displacements which appear to be more significant in stiffer walls. Using the effective stiffness and stiffness at ultimate load can accurately predict the yield displacement for slender walls and the ultimate displacement for the stiffer walls respectively. Moreover, estimation of yield and ultimate displacements depend on accurate estimation of the wall lateral stiffness and the slenderness of the wall.

3.3.3 Stiffness Degradation and Period Shift

In FBSD procedures such as those adopted by the ASCE/SEI 7-10 (ASCE 2010) and NBCC-15 (NRCC, 2015), the elastic (at yield) stiffness is used to predict the period of the structural component. Although such an approach satisfies the requirements for FBSD, it does not represent the SFRS stiffness degradation, due to inelastic response, under seismic loading. Subsequently, Priestley et al. (2007) suggested the use of the secant stiffness, within the context of DBSD, to facilitate better prediction of the SFRS seismic response. In addition to stiffness predictions, design codes often use empirical relationships to estimate the SFRS fundamental period. In FBSD this period is used to obtain the spectral acceleration, which is subsequently used to calculate the SFRS base shear demand. On the other hand, DBSD utilizes the effective period approach (Priestley et al., 2007) to predict the SFRS response at target displacement levels as explained before in Chapter 1.

To facilitate comparison between the walls, Fig 3.4 shows the wall normalized effective secant stiffness, K_{norm} plotted against displacement ductility, μ_{Δ} and the percentage drift. The normalized effective stiffness K_{norm}, used in Fig. 3.4 was derived by calculating the effective secant stiffness, K_e at each load cycle for both directions divided by the initial experimental wall stiffness, K_i evaluated at 20% of the yield load. The stiffness degradations trends show a similar behaviour for all the walls but with variations in the level of degradation. In general, all walls experienced severe stiffness degradation of approximately 80% at 0.5 % drift level, and continued to degrade at higher drift levels. From the test results, it can be inferred that the slab-coupled walls show steeper stiffness degradation at a drift range between 0.2 and 0.5%. In addition, Wall W4 with lower *DOC* (*DOC* =0.37) compared to that of Wall W3 (*DOC* = 0.51), exhibited the highest stiffness degradation over its loading history.

Figure 3.4 also illustrates the period elongation that occurs due to stiffness degradation for the walls. For details about calculating the normalized period $T_{norm,}$ the reader can refer to Shedid et al. (2010b). The figure shows the trend of normalized period increase with increased wall top displacements. Walls W1 and W2, which did not reach the 2.5% drift limit had their period elongation that varied between five and six times $T_{initial}$ at 1.8%. 1.9% top drifts respectively. The slab-coupled Walls W3 and W4 showed the highest period elongation, at least five times the initial period, $T_{initial}$ at 2.5% top drift signifying more cracking due to the formation of plastic hinges at the wall-slab interface. At this drift level, Walls W5 and W6 show 4.2 and 3.0 times $T_{initial}$ respectively. Higher period elongation reduces the seismic demand imposed on to the structural components and therefore such components can be designed for lower lateral shear forces.

3.3.4 Equivalent Viscous Damping

The SFRS energy dissipation capabilities and the corresponding equivalent viscous damping levels are key aspects of the DBSD procedure. In structural components, the equivalent viscous damping is a function of two components, elastic viscous damping, ζ_{el} and hysteretic damping, ζ_{hyst} ($\zeta_{eq} = \zeta_{el} + \zeta_{hyst}$). The elastic damping ratio for RM walls and systems is typically assumed to be equal to 5% (Priestley et al. 2007). Experimentally, the equivalent viscous damping at each cycle can be evaluated using Eq. 3.15 (Chopra, 2007) using the elastic potential energy, E_S and the dissipated energy, E_D, components respectively.

$$\zeta_{eq} = \frac{1}{4\pi} \times \frac{E_D}{E_S} \tag{3.15}$$

Priestley et al. (2007) proposed an empirical formulation for the hysteretic damping calculation of different SFRS, where, for RM SFRS, Eq. 3.16 can be used to relate the target displacement ductility level, μ_Δ, to the hysteretic damping ratio.

$$\zeta_{hyst} = 0.444 \times \left(\frac{\mu_\Delta - 1}{\mu_\Delta \pi} \right) \tag{3.16}$$

Figure 3.5 shows the experimental equivalent viscous damping ratio plotted against displacement ductility. Most walls experienced a gradual increase of the equivalent damping ratio up to $4\Delta_y$. After this displacement level, most walls experienced an almost constant equivalent damping ratio equal to approximately 20%. The figure illustrates the variability in the hysteretic damping ratios at different loading cycles for the walls. Equation 3.16 is also plotted on the same figure for comparison with experimental damping ratio curves after superimposing elastic damping of 5%.

The hysteretic damping ratios of the slab-coupled wall systems are influenced by the slab damage and the *DOC*. As such, the *DOC* was used to calculate the walls' and the slabs' contributions to the overall damping ratio of the slab-coupled wall system, ζ_{sys}, (Priestley et al. 2007) as given in Eq. 3.17-a and expanded in Eq. 3.17-b.

$$\zeta_{sys} = (1 - DOC)\,\zeta_W + (DOC)\zeta_{CS} \tag{3.17-a}$$

$$\zeta_{sys} = (1 - DOC)\left(0.05 + 0.444 \times \left(\frac{\mu_\Delta - 1}{\mu_\Delta \pi} \right) \right) + DOC\left(0.05 + 0.565 \times \left(\frac{\mu_\Delta - 1}{\mu_\Delta \pi} \right) \right) \tag{3.17-b}$$

In the above equations, the equivalent viscous damping contribution of the walls, ζ_W, and of the coupling slabs, ζ_c, are added algebraically after multiplying by the corresponding weight (*DOC* influence) as described in Priestley et al. (2007). Equation 3.17-b is an expansion of Eq. 3.17-a after substituting the formulations of ζ_W and ζ_c given by Priestley et al. (2007) as a function of the displacement ductility μ_Δ and coefficients representing the corresponding elastic damping and hysteretic rule. Figure 3.5 also depicts the variation in the damping ratio with the wall displacement ductility based on the experimental results and those predicted using Eq. 3.17-b. As can be seen, the equivalent viscous damping formulation given by Priestley et al. (2007) is on the conservative side when compared to the experimental results, which is consistent with the observations made by Shedid and El-Dakhakhni (2014) based on individual (uncoupled) wall results. The difference between the experimental results and Priestley's et al. (2007) predictions falls between 6% and 35%. On average, the walls reached as high as 21% equivalent viscous damping as compared to other walls.

The effect of slab coupling enhanced the equivalent viscous damping of the walls. The presence of slabs between the walls created more plastic hinge regions in wall/slab interfaces, which enhanced the energy dissipation mechanism of the walls. When compared to walls W5 and W6, the slab coupled Walls, W3 and W4 have at least the same or higher equivalent viscous damping at the same displacement ductility level up to $5\Delta_y$ as illustrated in Fig 3.5.

3.4 Performance-Based Seismic Design Parameters

3.4.1 Damage States and Crack Patterns

The development of the damage states DS1, DS2 and DS3, as defined by the FEMA 58-1/BD-3.8.10 (ATC 2009) which indicate slight, moderate and severe flexural damage, respectively, were noted during each wall test. The definition of each damage state is given in

Table 3.6. In addition to the FEMA 58-1/BD-3.8.10 (ATC 2009) damage states, two additional damage states, DS1* specified to describe slab damage, and DS3*, specified to indicate the outermost bar fracture were added to Table 3.6. The additional damage state, DS1* was introduced to characterize failure of the coupling slab as, currently, experimental test data and corresponding damage state definitions for slab-coupled RM shear walls do not exist.

The values of lateral load, *V*, and drifts corresponding to each wall's damage state are presented in Table 3.7. It is important to note the similarity in the drifts at the corresponding damage states, DS1, DS2 and DS3 even for walls with different configurations (Walls W1, W2 and W5) as shown in the load-displacement plots of Fig 3.6. The slab-coupled Walls W3 and W4 show resemblance in the drift values for the DS1, DS2 and DS3 damage states. Wall W6 damage states seem to occur at higher drifts compared to the other walls. Figure 3.7 shows sample photographs of the wall damage corresponding to the different damage states.

3.4.2 Extent of Plasticity

By specifying the extent of plasticity, one can identify the critical wall regions where special reinforcement detailing (e.g. additional shear reinforcement, avoiding lap splicing etc.) is required to contain wall damage and enhance wall performance under seismic demands. Experimentally, the *extent of plasticity*, denoted as L_p, can be obtained by analyzing the average curvature profiles as shown in Fig. 3.8. The L_p level in Fig. 3.8 is the height at which the average curvature of the wall exceeds the experimental yield curvature. High curvatures are typical near the base of the wall where most of the plastic deformations develop as shown in Fig. 3.8. Walls W1, W2, W3 and W4 had L_p values of 28%, 26%, 33% and 15% of l_w, respectively. Considering Walls W5 and W6, the extent of plasticity was higher than 36% of each wall's, length respectively. Overall, the values of L_p ranged between 15% and 40% of each wall's length for the six test walls; indicating the influence of the wall cross section configuration on the L_p levels. Another approach to roughly predict the extent of plasticity is by analyzing the wall deflection profiles shown for both the positive and negative loading directions in Fig. 3.9. The deformation profiles show maximum deflections at the free end as expected from a cantilever wall behaviour. Similar deformation patterns were noticed between the walls where the deflections become more abrupt when the walls pass their experimental yield as defined in the previous chapter. This can be attributed to the increase in the non-linear behaviour of the walls when higher displacement cycles are imposed past the yield point. As described by Shedid et. al (2010b), during the post ultimate load stages, kinks in such profiles can indicate the extent of the plastic hinge zone. All the plots show symmetry in both directions with Wall W6 showing some discrepancy as one of the displacement potentiometers reached its maximum stroke during testing. However, as no well-defined abrupt changes (kinks) were noticeable in the wall deflection profiles, it was difficult to accurately quantify the exact extent of the plasticity from Fig. 3.9. Subsequently, based on the results presented in Fig. 3.8, it is clear that Walls W1, W2 and W3 have significantly different extents of plasticity.

3.5 CONCLUSIONS

Chapter 3 presented analyses of an experimental study performed on reduced-scaled concrete block structural walls designed under the same prescriptive detailing requirements for specific SFRS classifications according to the North American code provisions. The walls are classified as *ductile reinforced masonry shear walls* and *special reinforced walls* following the CSA S304-14 (CSA 2014) and MSJC 2013 code provisions. The focus of the analyses was to evaluate key displacement- and performance-based seismic parameters for walls designed to meet the requirements of the same SFRS classification and having the same overall aspect ratio in order to quantify the effect of changing the cross sectional configuration. Moreover, the study presented preliminary analyses that may be used towards the adoption of slab-coupled masonry shear wall systems. The DBSD parameters studied included wall curvatures, wall displacements at yield and at the post-yield stages, stiffness degradation, period elongation and equivalent viscous damping. PBSD parameters included damage states identification and linkage to wall drift levels as well as extent of plasticity quantification. The values obtained for each parameter showed different characteristics and a range of ductile capabilities for the tested RM walls. Based on the chapters' results, the following conclusions can be made:

1. The experimental curvature ductility values based on the bottom 100 mm wall segments ranged between 8.2 and 30.2. The experimental values for curvature ductility were at least double the theoretical values for most of the walls. The slab coupled Walls W3 and W4 shows almost twice the ultimate curvatures when compared to Walls W1 and W2, respectively.
2. Moment curvature idealization is good for predicting ultimate displacement for slender walls but not for stiffer walls. The rationale lies in the fact that the idealization in Priestley's method might not account for coupled shear displacements that arises in stiffer walls. Using the effective stiffness and stiffness at ultimate load can accurately predict the yield displacement for slender walls and ultimate displacement for the stiffer walls respectively. Moreover, estimation of yield and ultimate displacements depend on accurate estimation of the wall lateral stiffness and the slenderness of the wall.
3. The stiffness degradations relationships show a similar decreasing trend for all the walls but with variations in the degradation level depending on the wall configuration.

4. Walls W1 and W2, (the walls did not reach the 2.5% drift limit prior to the 20% strength degradation level) had their period of elongation that varied between five to six times $T_{initial}$ at 1.8% and 1.9% top drift, respectively. On the other hand, the corresponding slab-coupled Walls W3 and W4 did reach the 2.5% top drift limit with similar period elongation prior to reaching their respective 20% strength degradation levels. At this drift level, Walls W5 and W6 showed 4.2 and 3.0 times their $T_{initial}$, respectively.

5. Most walls experienced a gradual increase of the equivalent damping ratio up to $4\Delta_y$. After this displacement level, most walls experienced an almost constant equivalent damping ratio equal to approximately 20%. The wall curvature profiles were used to quantify the extent of plasticity, L_p. The values of L_p ranged between 15% and 40% of each wall's length for the six test walls; indicating the influence of the wall cross section configuration on the L_p levels.

6. Based on the test results reported within the current chapter, walls with the same overall aspect and reinforcement ratios, with different cross section configuration, would possess different DBSD and PBSD parameters as well as a range of ductility capacity. In general, the slab-coupled walls demonstrated a better performance in terms of ultimate drifts capacities reached, period elongation and equivalent viscous damping when compared to the rectangular and the flanged walls. Moreover, the walls were capable of reaching, and sometimes exceeding, the drift capacities of Walls W5 and W6 but at a higher lateral load capacity than twice that of their corresponding individual wall components.

The current study highlights the need for additional provisions to be included in future North American masonry design codes that would reflect the slab-coupling effects on the seismic response of RM walls. In this respect, the current MSJC approach that does not recognize slab coupling as a means to couple RM walls might need to be revisited. In addition, the coupling influence on altering the response of RM walls would need to be addressed in future edition of the CSA S304. Finally, the study showed that, when applicable, accounting for slab coupling during the analysis process has the potential of affecting both DBSD and PBSD parameters on many levels (i.e. by affecting the extent of energy dissipation and the level of stiffness degradation and period of elongation). Nevertheless, because of the limited number of tests performed within the current study, additional studies that are focused on evaluating slab-coupled wall systems are necessary for codification of this SFRS.

3.6 Chapter 3 Notation

The following symbols are used in this chapter:

A_g = total gross cross-sectional area of the walls (mm^2);
A_e= effective web cross-sectional area of the wall (mm^2);
DOC = degree of coupling;
d= distance to extreme tension reinforcement from compression surface (mm);
d_{bl} = diameter of flexural reinforcement (mm);
E= young's modulus of the wall's material (MPa);
E_D= energy dissipated at certain displacement cycle(KN.mm);
E_S= energy dissipated through elastic system (KN.mm);
E_m=young's modulus of masonry (MPa);
f'_m=compressive strength of masonry prism (MPa);
f_y= yield stress of vertical reinforcement (MPa);
G_m=masonry shear modulus (MPa);
h = total height of the wall (mm);
H_{cf} = contra-flexure height (mm);
h_e = effective height of the wall (mm);
I_{cr}= cracking moment of inertia of shear wall (mm^4);
I_e= effective moment of inertia of the wall (mm^4);
I_g= gross moment of inertia of coupling element (mm^4);
k = shape factor taken as 1.2;
K_g – Wall's gross stiffness (kN/mm)
K_i – Initial experimental wall's stiffness (kN/mm)
K_e – Theoretical effective wall's stiffness (kN/mm)
K_{ey} – Experimental wall's stiffness at yield load (kN/mm)
K_{eVu} – Experimental wall's stiffness at ultimate load (kN/mm)
$K_{e\Delta fr}$ –Experimental wall's stiffness at bar fracture (kN/mm)
l_{cs} = clear span of coupling slab (mm);
l_p = plastic hinge length of the wall (mm);
L_p = extent of plasticity (mm);

l_{sp}= strain penetration length of flexural reinforcement (mm);
l_w= length of wall (mm);
M = overturning moment in a structural wall (kN·m);
V = applied lateral load (kN);
V_y= lateral yield force of the wall (kN);
V_u = ultimate lateral force of the wall (kN);
ϕ_{dc}=damage control state curvature (mm^{-1});
ϕ_{ls}=limit state curvature (mm^{-1});
ϕ_m =masonry material reduction factor;
ϕ_h =horizontal reinforcement bar diameter (mm);
ϕ_s= serviceability curvature (mm^{-1})
ϕ_v =vertical reinforcement bar diameter (mm);
ϕ_y =yield curvature of the individual wall (mm^{-1});
$\phi_{y,exp}$= experimental yield curvature (mm^{-1});
$\phi_{y,th1}$ =the theoretical yield curvature using mechanics approach (mm^{-1});
$\phi_{y,th2}$ =the theoretical yield curvature using Paulay 2002 (mm^{-1});
ϕ_u = ultimate curvature of the individual wall (mm^{-1});
$\phi_{u,exp}$= experimental ultimate curvature (mm^{-1});
$\phi_{u,th1}$ =theoretical ultimate curvature using mechanics approach (mm^{-1});
$\phi_{u,th2}$ =theoretical ultimate curvature using Paulay 2002 (mm^{-1});
θ_C= code drift rotation limit;
$\Delta_{D\varepsilon}$= ultimate theoretical displacement for wall base strain case (mm);
$\Delta_{D\theta}$= ultimate theoretical displacement for drift limit case (mm);
Δ_{Vu}= displacement at maximum lateral load (mm);
Δ_p= plastic displacement (mm);
Δ_{max} = displacement at collapse limit state (mm);
$\Delta_{0.8Vu}$ = displacement at 20% ultimate load degradation (mm);
Δ_{top}= total top displacement of the wall (mm);
Δ_{up}= predicted ultimate displacement (mm);
Δ_{u1} = predicted ultimate displacement corresponding to CSA definition (mm);
Δ_{u2} = predicted ultimate displacement corresponding to Priestley 2007 definition (mm);
Δ_y= theoretical yield displacement (mm);
Δ_{yp}= predicted yield displacement (mm);
Δ_{ym}= measured yield displacement (mm);
μ_ϕ= curvature ductility of the shear wall;
μ_Δ= displacement ductility of the shear wall;
$\mu^{ep}_{\Delta 1\%}$= idealized displacement ductility at 1% drift limit;
$\mu^{ep}_{\Delta 0.8Fu}$= idealized displacement ductility at 20% ultimate load degradation
$\mu^{ep}_{\Delta max}$= idealized displacement ductility at collapse limit state
ζ_{hyst}= hysteretic viscous damping
ζ_c = hysteretic viscous damping for coupled-slab
ζ_{eq}= equivalent viscous damping
ζ_{hyst}= hysteretic viscous damping
ζ_W= hysteretic viscous damping for wall
ρ_h= percent area of reinforcement in the horizontal direction (%);
ρ_v= percent area of reinforcement in the vertical direction (%);

ε_y= yield strain of vertical reinforcement;

3.7 CHAPTER 3 REFERENCES

Applied Technology Council (ATC). (2009). "Background Document: Damage States and Fragility Curves for Reinforced Masonry Shear Walls." Federal Emergency Management Agency (FEMA) 58-1/BD-3.8.10, Washington, DC.

Applied Technology Council (ATC). (2012). "Seismic performance assessment of buildings. Vol. 1: Methodology." Federal Emergency Management Agency (FEMA) 58-1, Washington, DC.

ASCE (2010) "Minimum Design Loads for Buildings and Other Structures." ASCE Standard SEI/ASCE 7-10, American Society of Civil Engineers, Reston, Virginia.

Beyer, K. (2005)."Design and Analysis of Walls Coupled by Floor Diaphragms." M.S. Thesis, I.U.S.S., Pavia, Italy.

Canadian Standards Association (CSA). (2014) "Design of masonry structures." CSA S304-14, Mississauga, Canada.

Chopra, A. K. (2007). *Dynamics of Structures: Theory and Applications to Earthquake Engineering*, 3rd Ed., Pearson Prentice Hall, Upper Saddle River, NJ.

Drysdale, R.G., Hamid A. (2005). *Masonry Structures Behaviour and Design*, Canada Masonry Design Centre, Mississauga.

Lehman, D. E., Turgeon, J. A., Birely A. C., Hart, C. R., Marley, K. P., Kuchma D. A., Lowes, L. N. (2013). "Seismic Behaviour of a Modern Concrete Coupled Wall."*J. Struct. Eng.,* August 2013, 139(8), 1371-1381.

Masonry Standards Joint Committee of the American Concrete Institute, American Society of Civil Engineers, and The Masonry Society (MSJC). (2013). "Building code requirements for Masonry Structures." TMS 402-13/ASCE 5-13/ACI 530-13, Detroit, MI, New York, and Boulder, CO.

Massone, L. and Wallace, J. (2004). "Load-Deformation Responses of Slender Reinforced Concrete Walls." *ACI Struct. J.*, Vol. 101, No. 1, pp. 103-113.

National Building Code of Canada (NBCC). (2015). "National Building Code of Canada 2010." National Research Council of Canada, *NRC*, Ottawa, Canada.

Paulay T., (1981). "The Design of Reinforced Concrete Ductile Shear Walls for Earthquake Resistance." *Research Report*, University of Canterbury, New Zealand.

Paulay T., (2002). "The displacement capacity of reinforced concrete coupled walls."*Eng. Struct*. (24), 1165-1175

Paulay T., and Priestly, M. (1992). *Seismic design of reinforced concrete and masonry buildings*, Wiley, New York.

Priestley, M. J. N. (2000). "Performance-based seismic design" Keynote Address, *Proceedings of the Twelfth World Conference on Earthquake Engineering*. Earthquake Engineering Research Institute, Auckland, New Zealand, Paper #2831.

Priestley, M.J.N., and Kowalsky, M.J. (1998). "Aspects of drift and ductility capacity of rectangular structural walls." *Bulletin of the New Zealand Society for Earthquake Engineering*, 31: 73–85.

Priestley, N., Calvi, G., and Kowalsky, M. (2007). *Displacement-based seismic design of structures*, IUSS Press, Pavia, Italy.

Seible, F., Kingsley, G. R., Priestley, M. J. N., and Kurkchubasche, A. G. (1991). "Flexural coupling of topped hollow core plank floor systems in shear wall Structures." *Report No. SSRP 91/10*, Department of Structural Engineering, University of California, San Diego, La Jolla, CA.

Shedid, M. and El-Dakhakhni, W. (2014). "Plastic Hinge Model and Displacement-Based Seismic Design Parameter Quantifications for Reinforced Concrete Block Structural Walls." *J. Struct. Eng*.,140(4), 04013090.

Shedid, M., El-Dakhakhni, W. and Drysdale, R. (2010a). "Characteristics of Rectangular, Flanged and End- Confined Reinforced Concrete Masonry Shear Walls for Seismic Design." *J. Struct. Eng.,* 136 (12), 1471-1482.

Shedid, M.,El-Dakhakhni, W., and Drysdale, R.(2010b). "Seismic Performance Parameters for Reinforced Concrete-Block Shear Wall Construction." *J. Perform. Constr. Facil*.,24(1), 4–18.

Siyam, M., El-Dakhakhni, W., Shedid, M., and Drysdale, R. (2015a). "Seismic Response Evaluation of Ductile Reinforced Concrete Block Structural Walls. I: Experimental Results and Force-Based Design Parameters." *J. Perform. Constr. Facil.*, 10.1061/(ASCE)CF.1943-5509.0000794, 04015066.

Stavridis, A., Ahmadi F., Mavros M., Koutromanos I., Hernández J., Rodríguez J., Shing P. B., and Klingner R. E. (2011). "Shake-table tests of a 3-story, full-scale masonry wall system." *Proc., ACI Masonry Seminar*, Dallas, TX.

Tomaževič, M. (1999). *Earthquake resistant design of masonry buildings,* Imperial College Press, London.

White, T., and Adebar, P. (2004). "Estimating rotational demands in high-rise concrete wall buildings" *13th World Conference on Earthquake Engineering*, Vancouver, BC, Canada, 15.

Table 3.1: Wall Details and Specifications

Wall	Configuration	Height (mm)	Overall length (mm)	Overall aspect ratio	Vertical reinforcement ρ_v (%)	Horizontal reinforcement		CSA S304-14 classification	MSJC-13 classification
						ρ_{h1}* (%)	ρ_{h2} ** (%)		
W1	Rectangular	2160	1533	1.4	0.6	0.26	0.14	Ductile	Special
W2	Flanged	2160	1533	1.4	0.6	0.26	0.14	Ductile	Special
W3	Coupled I	2160	1533	1.4	0.6	0.26	0.14	Ductile	Special
W4	Coupled II	2160	1533	1.4	0.6	0.26	0.14	Ductile	Special
W5 [a]	Rectangular	2160	598	3.6	0.6	0.26	0.14	Ductile	Special
W6 [b]	Rectangular	2160	465	4.6	0.6	0.26	0.14	Ductile	Special

a – W5 is the individual wall of the coupled wall system W3

b – W6 is the individual wall of the coupled wall system W4

***ρ_{h1} – Horizontal reinforcement ratio in the first storey**

****ρ_{h2} – Horizontal reinforcement ration in the second storey**

Table 3.2: Walls Curvatures and Curvature Ductility Values

	Wall					
	W1	W2	W3	W4	W5	W6
Theoretical curvature values at yield and ultimate (*Method I - mechanics based*)						
$\phi_{y,th1}$ *(1 x* 10^{-6}*)*	2.2	2.1	11.9	12.3	5.9	7.7
$\phi_{u,th1}$ *(1 x* 10^{-6}*)*	14.3	85.9	74.3	76.8	36.4	48.4
$\mu_{\phi 1}$	6.6	40.7	6.2	6.3	6.2	6.3
Theoretical curvature values @ yield and ultimate (*Method II - Paulay 2002*)						
$\phi_{y,th2}$ *(1 x* 10^{-6}*)*	3.3	2.7	16.0	15.6	7.9	9.8
$\phi_{u,th2}$ *(1 x* 10^{-6}*)*	46.7	46.9	120.4	154.8	120.4	154.8
$\mu_{\phi 2}$	14.3	17.4	7.5	9.9	15.3	15.7
Experimental curvatures values (averaged over the wall bottom 100 mm from both loading direction)						
$\phi_{y,exp}$ *(1 x* 10^{-6}*)*	4.6	2.6	15.3	14.6	13.3	11.5
$\phi_{u,exp}$ *(1 x* 10^{-6}*)*	68.6	78.4	125.2	151.7	168.6	176.4
$\mu_{e\phi 1}$	14.8	30.2	8.2	10.4	12.7	15.3
$\mu_{e\phi 1}/\mu_{\phi 1}$	2.3	0.7	1.3	1.7	2.0	2.4
$\mu_{e\phi 1}/\mu_{\phi 2}$	1.0	1.7	1.1	1.1	0.8	1.0

$\phi_{y,th1}$: Theoretical yield curvature using *Method I*: mechanics based approach in rad/mm
$\phi_{u,th1}$: Theoretical ultimate curvature using *Method I* rad/mm
$\mu_{\phi 1}$: Theoretical curvature ductility using *Method I*
$\phi_{y,th2}$: Theoretical yield curvature using *Method II*: Paulay 2002 approach in rad/mm
$\phi_{u,th2}$: Theoretical ultimate curvature using *Method II* in rad/mm
$\mu_{\phi 2}$: Theoretical curvature ductility using *Method II*
$\phi_{y,exp}$: Experimental yield curvature in rad/mm
$\phi_{u,exp}$: Experimental ultimate curvature in rad/mm
μ_e : Experimental curvature ductility

Table 3.3: Theoretical Coefficient of Dimensionless Curvature

Wall	***c/l_w***	***M_y (kN.m)***	***M_n (kN.m)***	***$1-c/l_w$***	***η***
W1	0.23	120.0	185.0	0.77	2.01
W2	0.21	195.0	256.0	0.79	1.66
W5	0.24	21.0	30.4	0.76	1.88
W6	0.24	14.0	19.0	0.76	1.83

Table 3.4: Theoretical and Experimental Wall Displacements

Wall	W1	W2	W3	W4	W5	W6
Theoretical Displacement at Yield and Post-yield stage (*Method A* – Priestley et al. 2007 using $\phi_{y,th2}$ and $\phi_{u,th2}$)						
Δ_{y1} (mm)	5.7	4.3	11.5	11.7	14.7	18.9
Δ_{u1} (mm)	9.7	37.5	26.7	25.8	21.5	26.8
% difference between Δ_{y1} and Δ_{ym}	8.8	62.8	12.7	6.0	50.0	27.7
% difference between Δ_{u1} and Δ_{um}	33.0	169.8	35.5	40.3	14.0	6.5
Theoretical Displacement at Yield and Post-yield stage (*Method B* - Effective and Stiffness at Ultimate Load)						
Δ_{y2} (mm)	5.1	5.3	7.1	7.4	11.2	15.4
Δ_{u2} (mm)	13.0	11.5	75.3	26.7	32.7	41.9
% difference between Δ_{y2} and Δ_{ym}	21.6	32.1	30.4	40.3	14.3	4.1
% difference between Δ_{u2} and Δ_{um}	0.8	20.9	108.3	9.0	33.4	42.0
Experimental Displacements at Yield and Post-yield						
Total displacement						
Δ_{ym} (mm)	6.2	7.0	10.2	12.4	9.8	14.8
Δ_{um} (mm)	12.9	13.9	36.2	24.5	24.5	29.5
$\Delta_{0.8Vu}$ (mm)	32.1	35.3	58.8	63.7	47.0	69.2
Δ_{fr} (mm)	38.6	42.6	72.6	74.1	65.5	88.5
Flexure component						
Δ_{fy} (mm)	3.7	4.3	9.2	9.8	7.4	12.9
Δ_{fu} (mm)	8.4	7.4	22.5	13.1	20.8	26.7
Sliding component						
Δ_{sy} (mm)	0.3	0.3	0.2	0.4	0.0	0.1
Δ_{su} (mm)	0.6	0.8	2.0	0.8	0.3	0.2
Shear component						
Δ_{shy} (mm)	2.2	2.3	0.8	2.2	2.4	1.8
Δ_{shu} (mm)	3.9	5.7	11.7	10.6	3.5	2.6
% flexure of Δ_{ym}	59.7	61.4	90.0	79.0	75.5	87.2
% flexure of Δ_{um}	65.1	53.2	62.2	53.5	84.9	90.5

Δ_{ym}: Measured yield displacement in mm
Δ_{um}: Measured ultimate displacement in mm
$\Delta_{0.8Vu}$: Experimental load at 20% load degradation in mm
Δ_{max}: Experimental load at 50% or higher load degradation in mm
Δ_{fy}: Flexural component at yield force in mm
Δ_{fu}: Flexural component at ultimate force in mm

Δ_{sy}: Sliding component at yield force in mm
Δ_{su}: Sliding component at ultimate force in mm
Δ_{shy}: Shear displacement at yield force in mm
Δ_{shu}: Shear displacement at ultimate force in mm

Table 3.5: Gross, Effective and Experimental Wall Stiffness Values

Wall	**K_g (kN/mm)**	**K_e (kN/mm)**	**K_{ey} (kN/mm)**		**K_{eVu} (kN/mm)**		**$K_{e\Delta fr}$ (kN/mm)**		**Exp. V_y (kN)**	**Exp. V_u (kN)**
			(+)	(-)	(+)	(-)	(+)	(-)		
W1	52.7	16.1	11.0	10.7	7.1	6.3	1.4	1.4	67.0	85.9
W2	78.5	23.9	13.2	13.9	8.6	8.4	2.2	1.8	94.3	117.3
W3	8.3	5.4	1.0	0.9	0.8	0.5	0.2	0.1	33.9	42.3
W4	4.0	2.6	1.6	1.9	1.2	0.7	0.3	0.2	21.3	27.4
W5	4.0	1.2	1.0	0.9	0.8	0.5	0.2	0.1	9.3	14.6
W6	1.9	0.6	0.5	0.5	0.3	0.3	0.1	0.1	7.3	9.4
2 ×W5[a]	8.0	2.4	2.1	1.7	1.7	1.0	0.3	0.2	18.6	29.2
2 × W6[a]	3.8	1.2	0.9	0.9	0.7	0.6	0.2	0.2	14.3	18.8

Note: a – Walls W5 and W6 stiffnesses and lateral load capacities are doubled.

Table 3.6 FEMA 58-1 (ATC 2009) Damage State Description for Reinforced Masonry Walls

Damage State	Description	Repair Measure Fully grouted
DS1 Slight damage in flexure	1. Few flexural and shear cracks with hardly noticeable residual crack widths. 2. Slight yielding of extreme vertical reinforcement. 3. No spalling 4. No fracture or buckling of vertical reinforcement. 5. No structural significant damage.	1. Cosmetic repair. 2. Patch cracks and paint each side.
DS1* Slight damage in flexure	1. Numerous flexural and maybe diagonal cracks. 2. Slab cracks extending over an effective width	1. Epoxy injection to repair cracks. 2. Patch cracks and paint each side.
DS2 Moderate damage in flexure	1. Numerous flexural and diagonal cracks. 2. Mild toe crushing with vertical cracks or light spalling at wall toes. 3. No fracture or buckling of reinforcement. 4. Small residual deformation.	1. Epoxy injection to repair cracks. 2. Remove loose masonry. 3. Patch spalls with non-shrink grout. 4. Paint each side.
DS3 Severe damage in flexure	1. Severe flexural cracks. 2. Severe toe crushing and spalling. 3. Significant residual deformation.	1. Shore. 2. Demolish existing wall. 3. Construct new wall.
DS3* Severe damage in flexure	1. Fracture of one or more extreme reinforcements	1. Shore. 2. Demolish existing wall. 3. Construct new wall.

Table 3.7: Wall Drift Levels at Different Damage States

Wall	DS1		DS1*		DS2		DS3		DS3*	
	V (kN)	**Drift (%)**	**V (kN)**	**Drift (%)**	**V (kN)**	**Drift (%)**	**V (kN)**	**Drift (%)**	**V (kN)**	**Drift (%)**
W1	32.0	0.1	N/A	N/A	79.1	1.2	68.2	1.5	52.5	1.8
W2	52.4	0.1	N/A	N/A	111	1.3	105	1.6	71.4	1.9
W3	16.3	0.2	21.7	0.3	41.6	1.0	38.7	2.4	22.4	3.3
W4	13.2	0.2	22.3	0.5	26.2	1.1	23.4	2.9	18.8	3.4
W5	5.4	0.2	N/A	N/A	13.8	1.3	13.5	2.2	8.4	3.0
W6	4.9	0.4	N/A	N/A	8.5	2.7	7.4	3.4	4.6	4.8

* - Damage states corresponding to slab-coupled walls

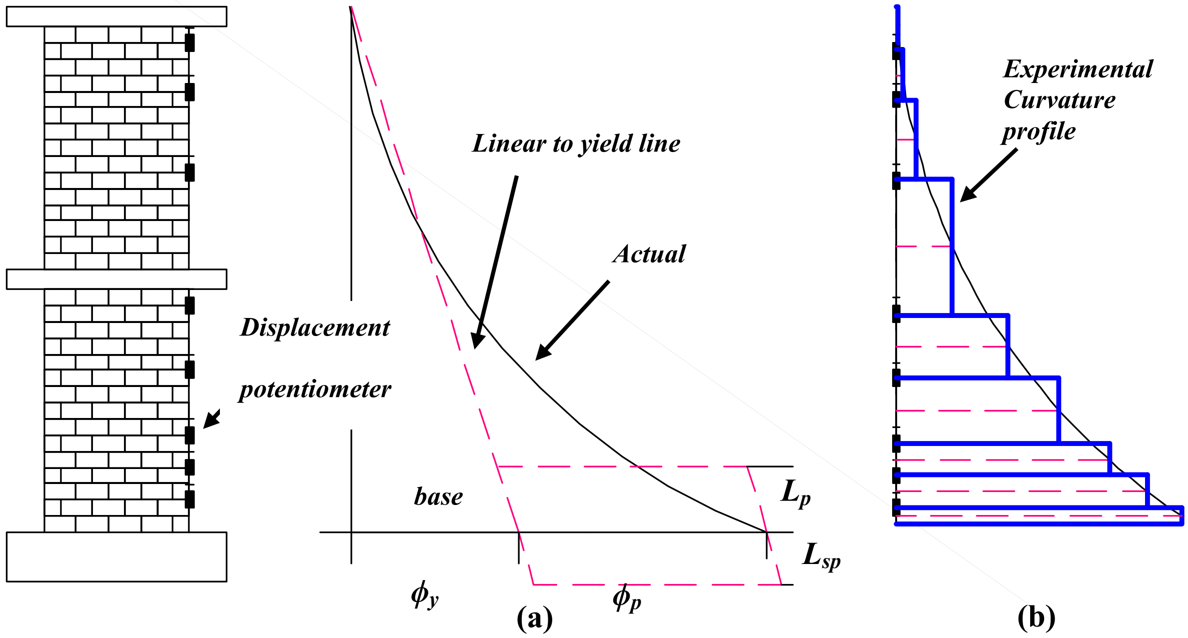

Fig. 3.1. Sample displacement potentiometer setup: (a) Plastic hinge idealization; (b) Curvature profile

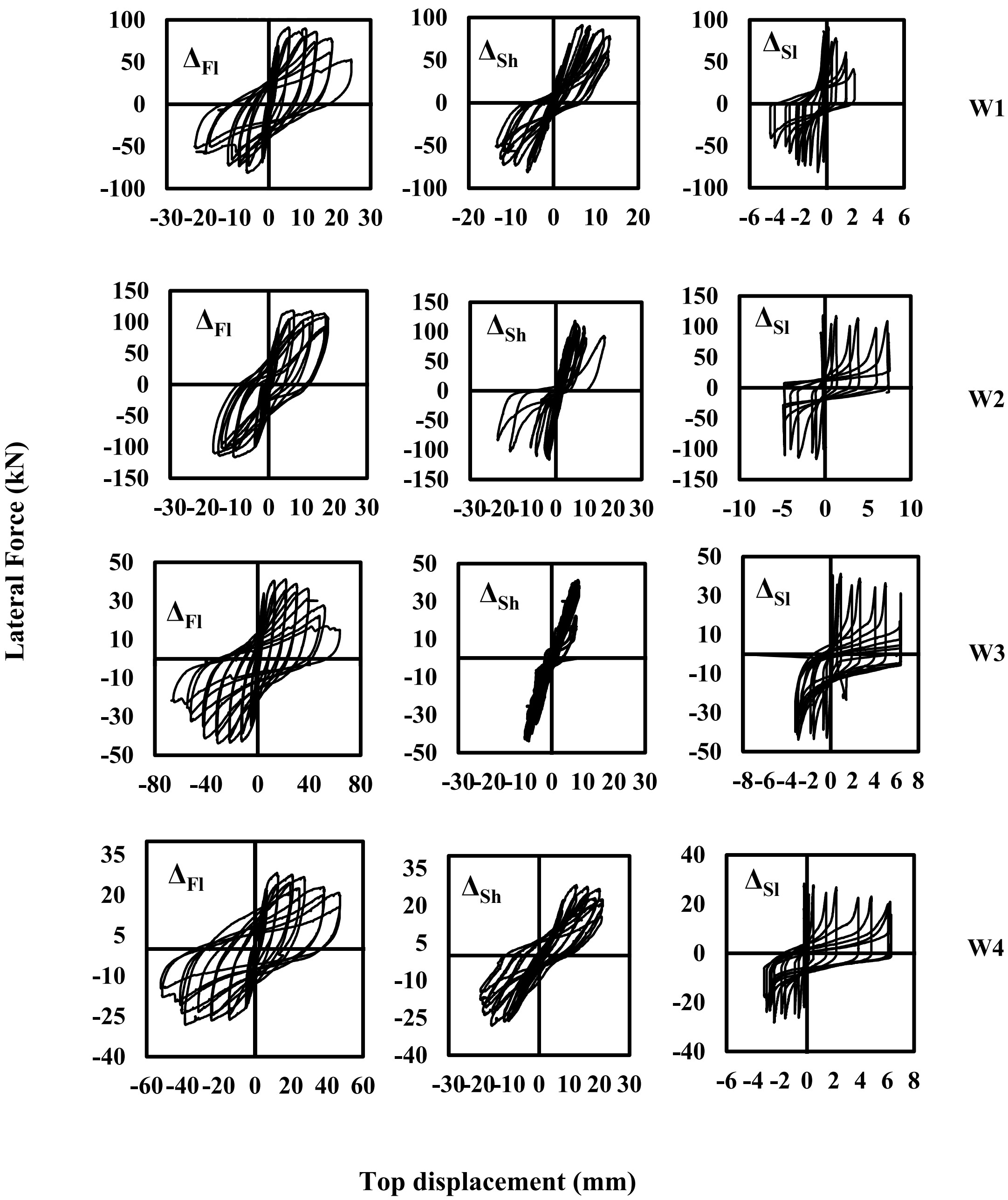

Lateral Force (kN)
Top displacement (mm)
Δ_{Fl}
Δ_{Sh}
Δ_{Sl}
W1
W2
W3
W4

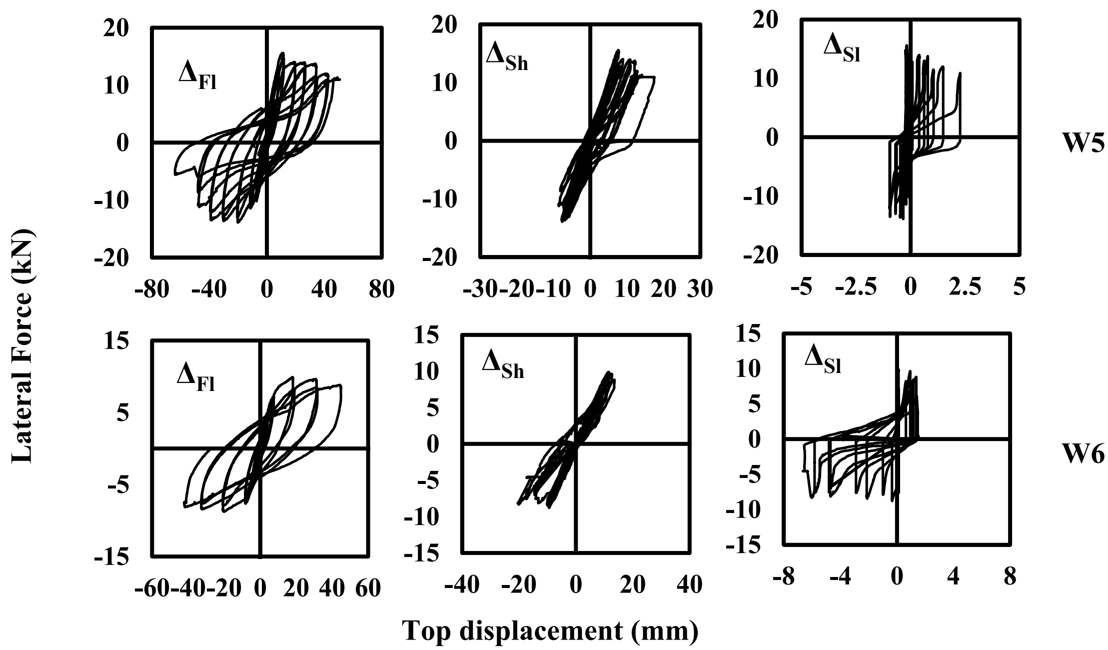

Fig. 3.2. Decoupled hysteresis relationships for the six walls

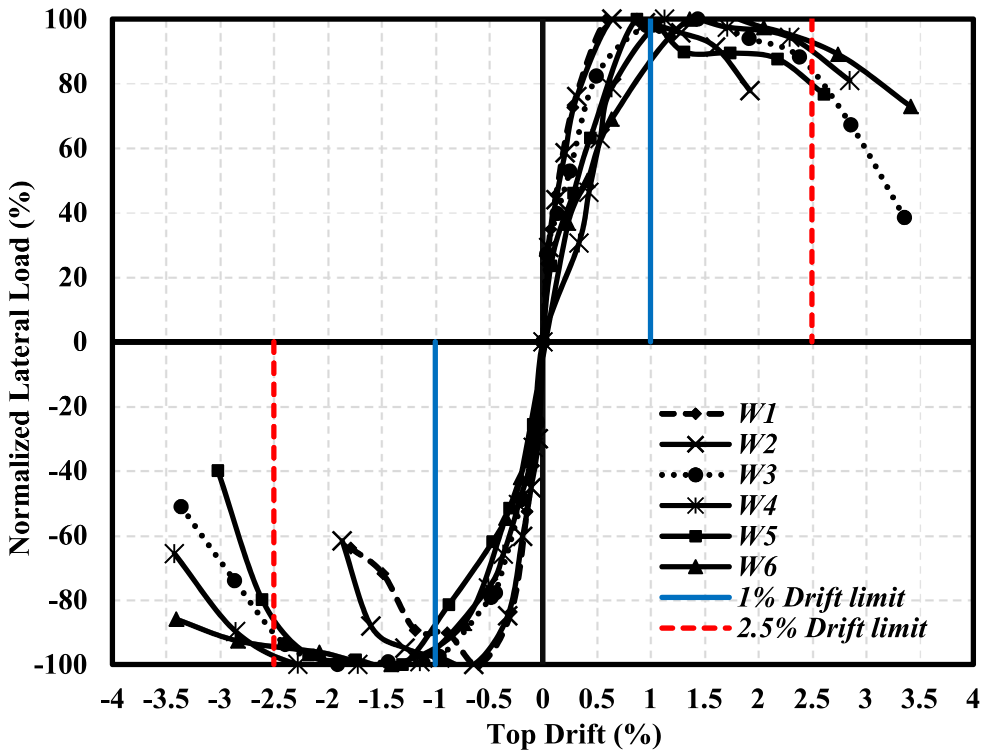

Fig. 3.3. Normalized load versus % drift for all the walls

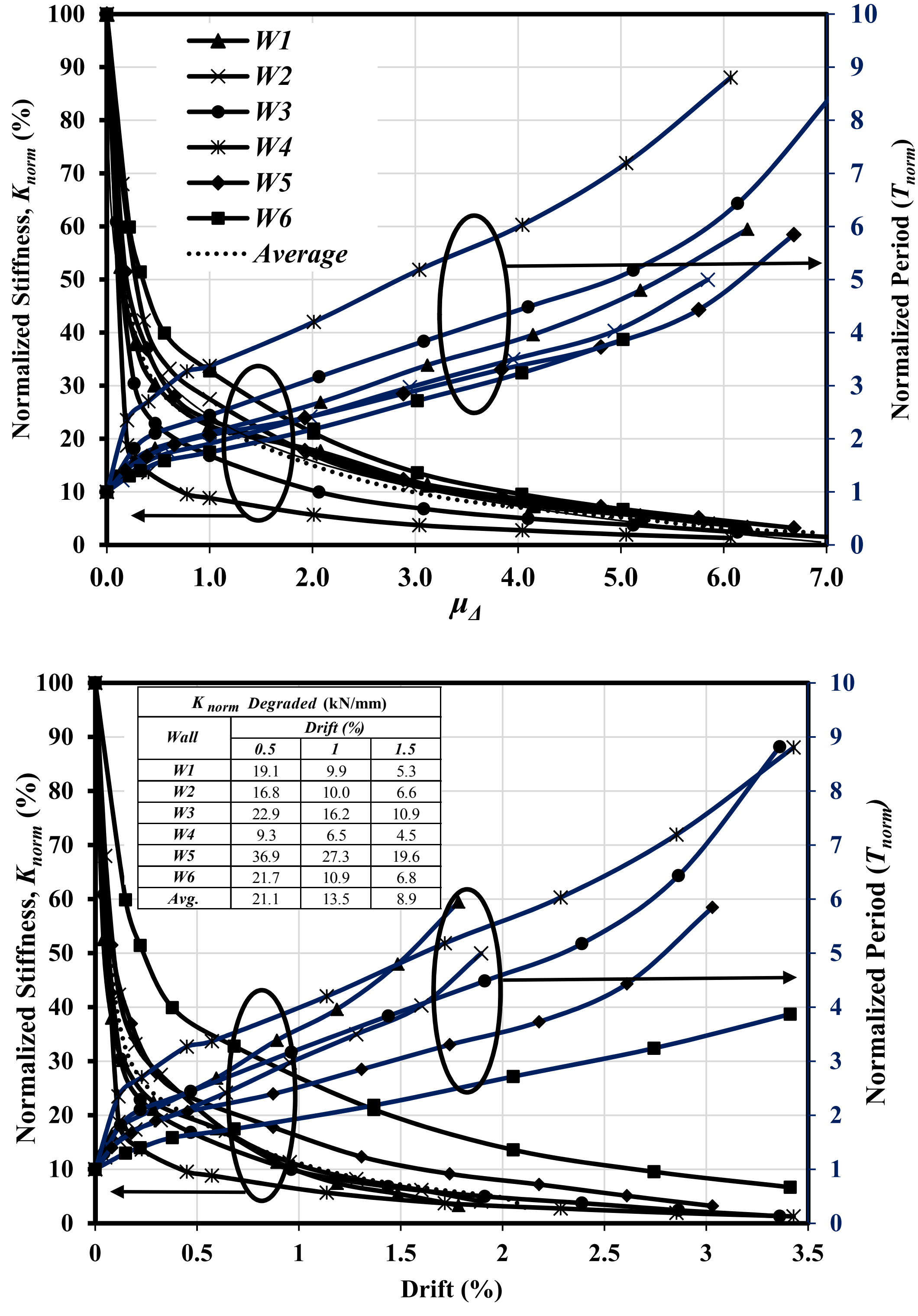

K_{norm} *Degraded* (kN/mm)			
Wall	*Drift (%)*		
	0.5	*1*	*1.5*
W1	19.1	9.9	5.3
W2	16.8	10.0	6.6
W3	22.9	16.2	10.9
W4	9.3	6.5	4.5
W5	36.9	27.3	19.6
W6	21.7	10.9	6.8
Avg.	21.1	13.5	8.9

Fig. 3.4. Variation of normalized stiffness and period with; (a) Displacement ductility; (b) Drift

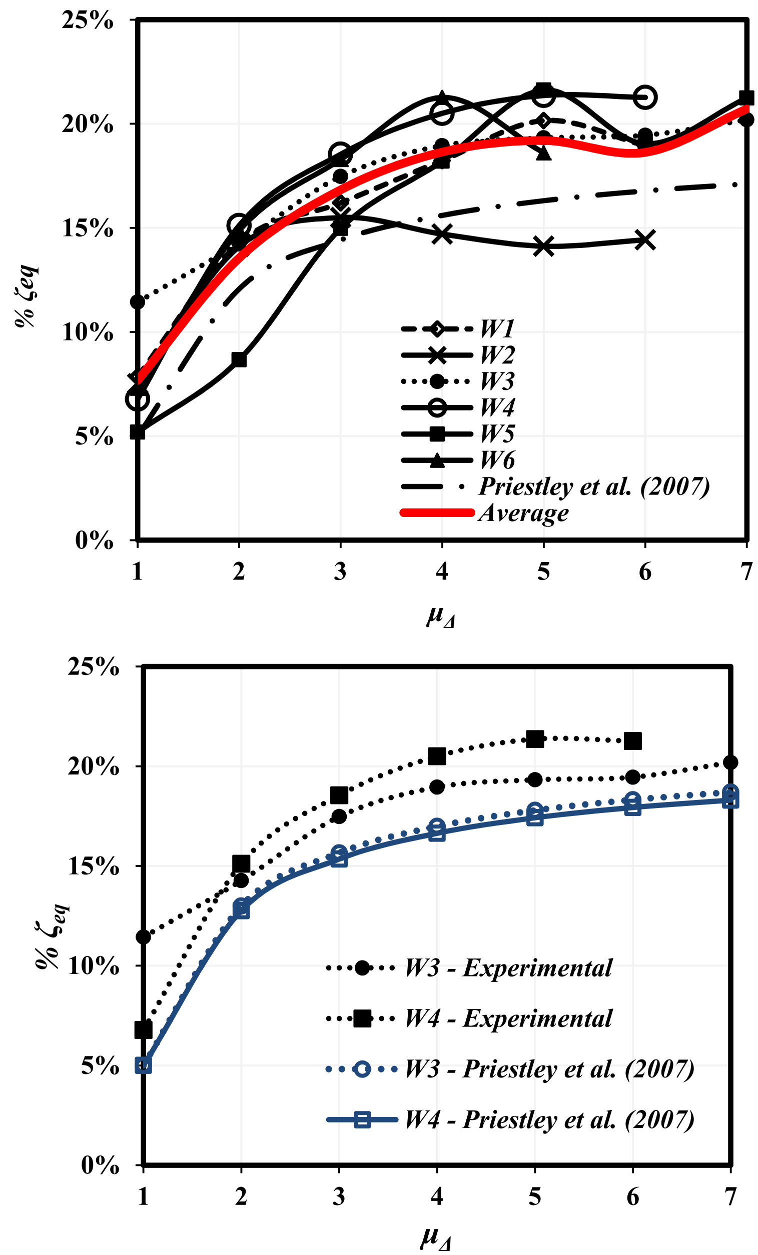

Fig. 3.5. Equivalent viscous damping against displacement ductility: (a) All the walls; (b) Slab-coupled Walls

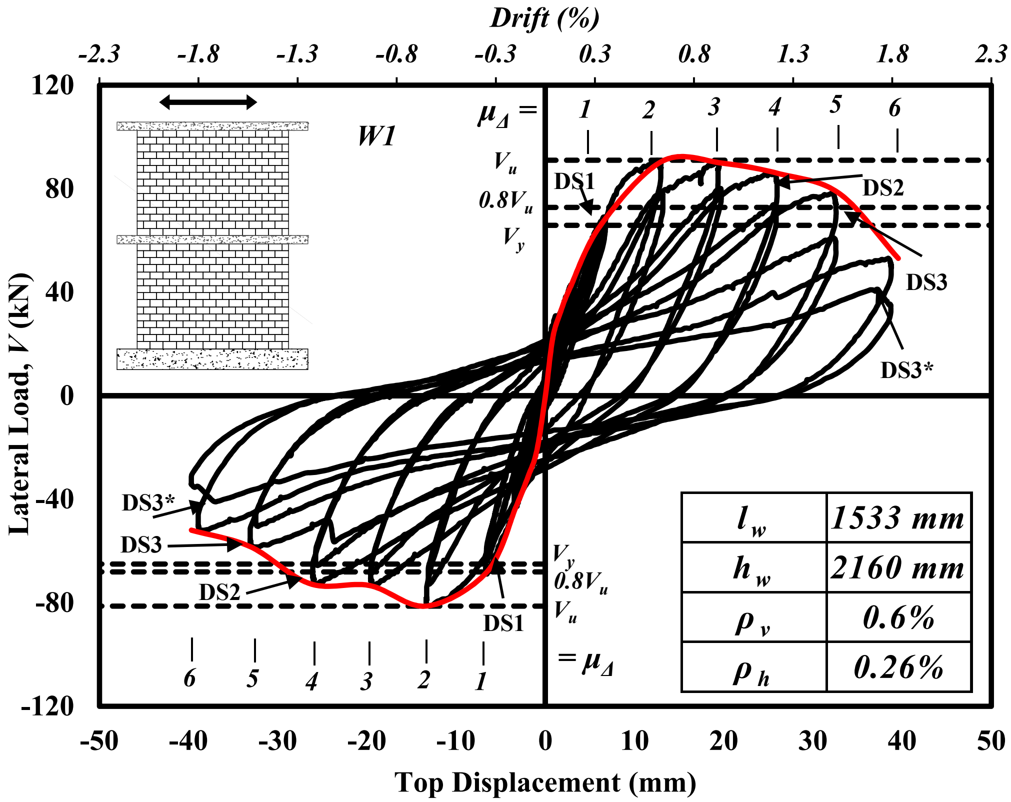

l_w	1533 mm
h_w	2160 mm
ρ_v	0.6%
ρ_h	0.26%

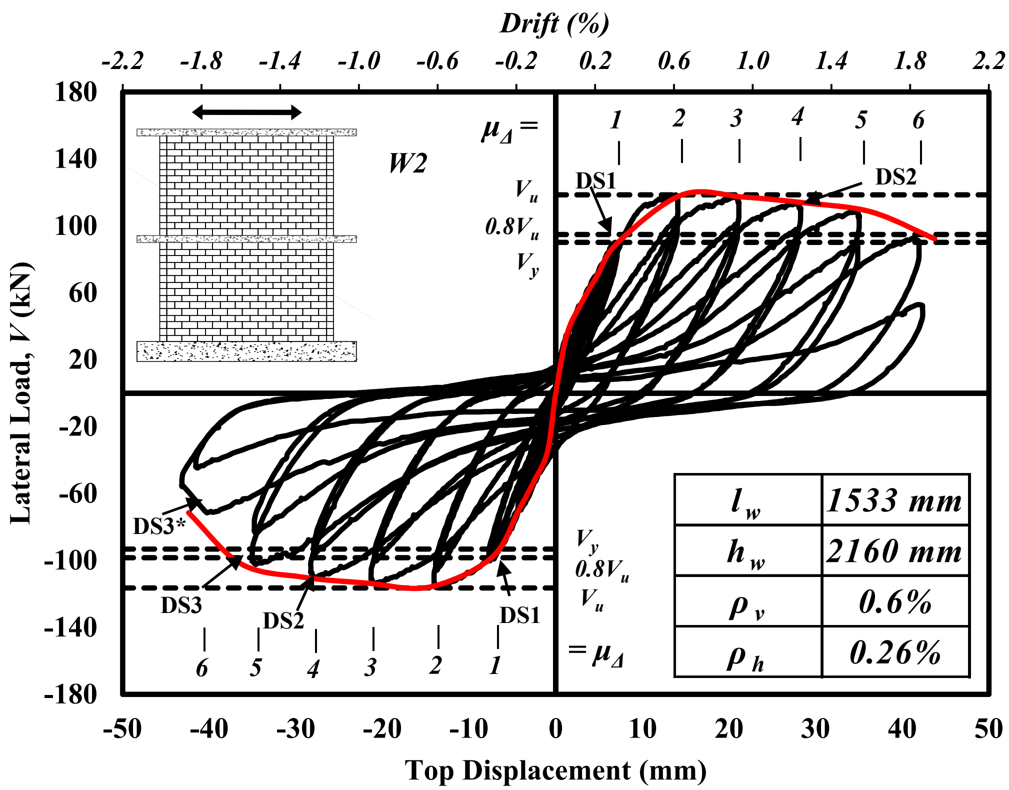

l_w	1533 mm
h_w	2160 mm
ρ_v	0.6%
ρ_h	0.26%

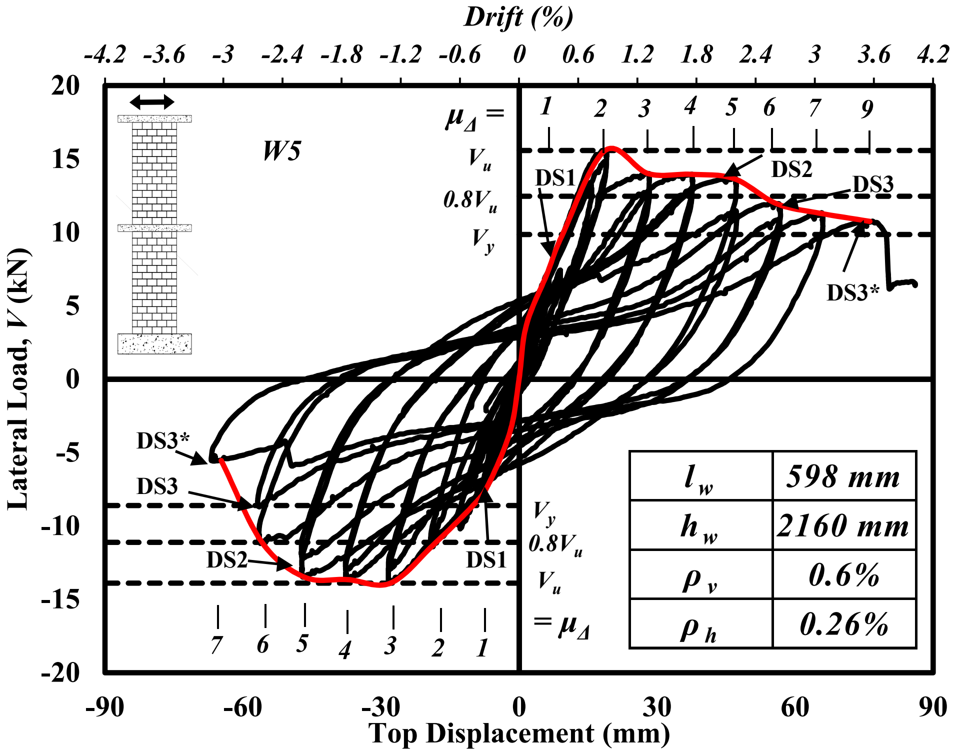

l_w	598 mm
h_w	2160 mm
ρ_v	0.6%
ρ_h	0.26%

Fig. 3.6. Load-Displacement relationship with damage state identification; (a) W1; (b) W2; (c) W3

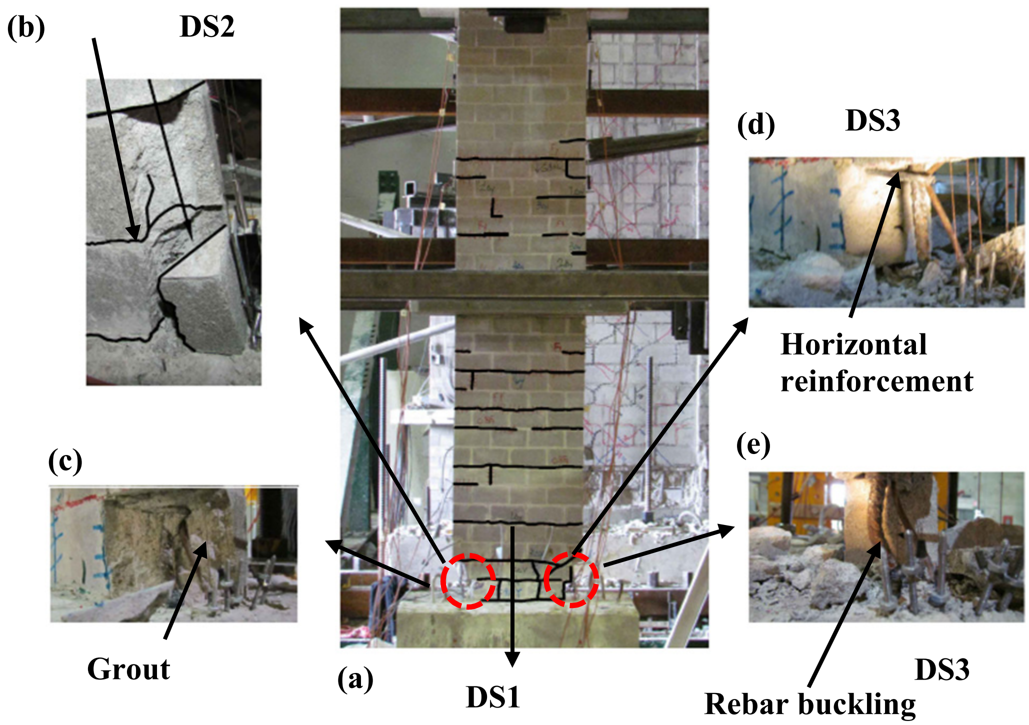

Fig. 3.7. Damage states in reinforced masonry shear wall

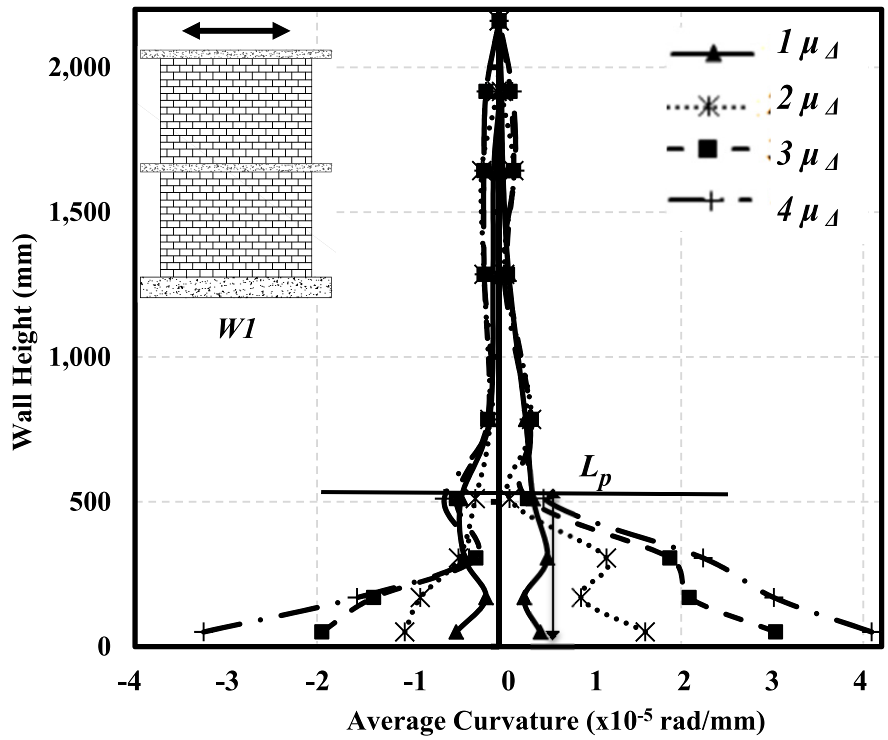

1 μ Δ
2 μ Δ
3 μ Δ
4 μ Δ
W1
Lp
Wall Height (mm)
0
500
1,000
1,500
2,000
-4
-3
-2
-1
0
1
2
3
4
Average Curvature (x10-5 rad/mm)

(a)

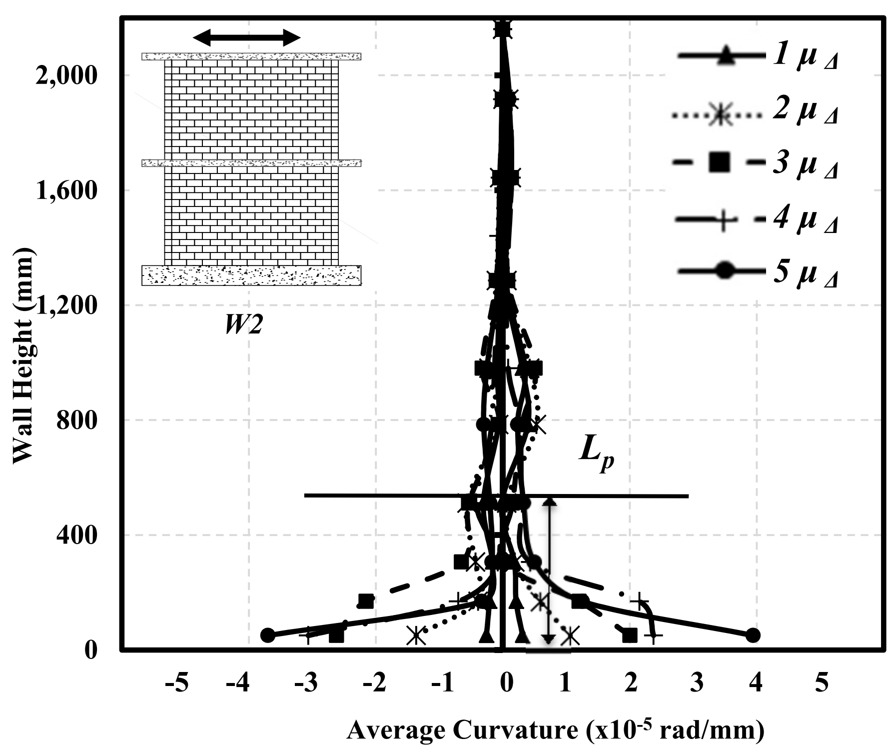

1 μ Δ
2 μ Δ
3 μ Δ
4 μ Δ
5 μ Δ
W2
Lp
Wall Height (mm)
0
400
800
1,200
1,600
2,000
-5
-4
-3
-2
-1
0
1
2
3
4
5
Average Curvature (x10-5 rad/mm)

(b)

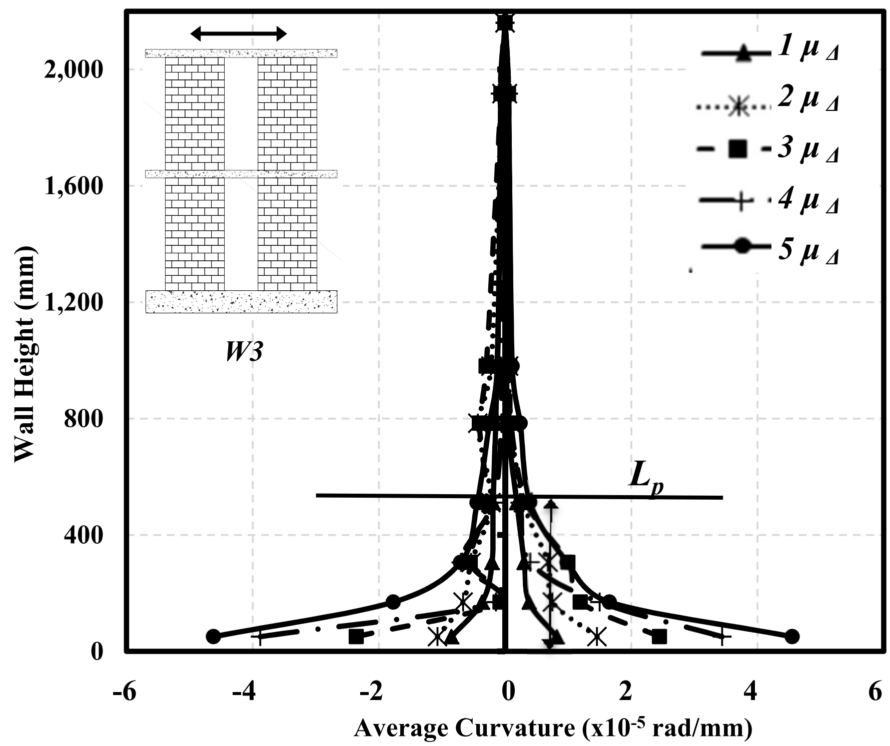

1 μ Δ
2 μ Δ
3 μ Δ
4 μ Δ
5 μ Δ
W3
L p
Wall Height (mm)
Average Curvature (x10-5 rad/mm)

(c)

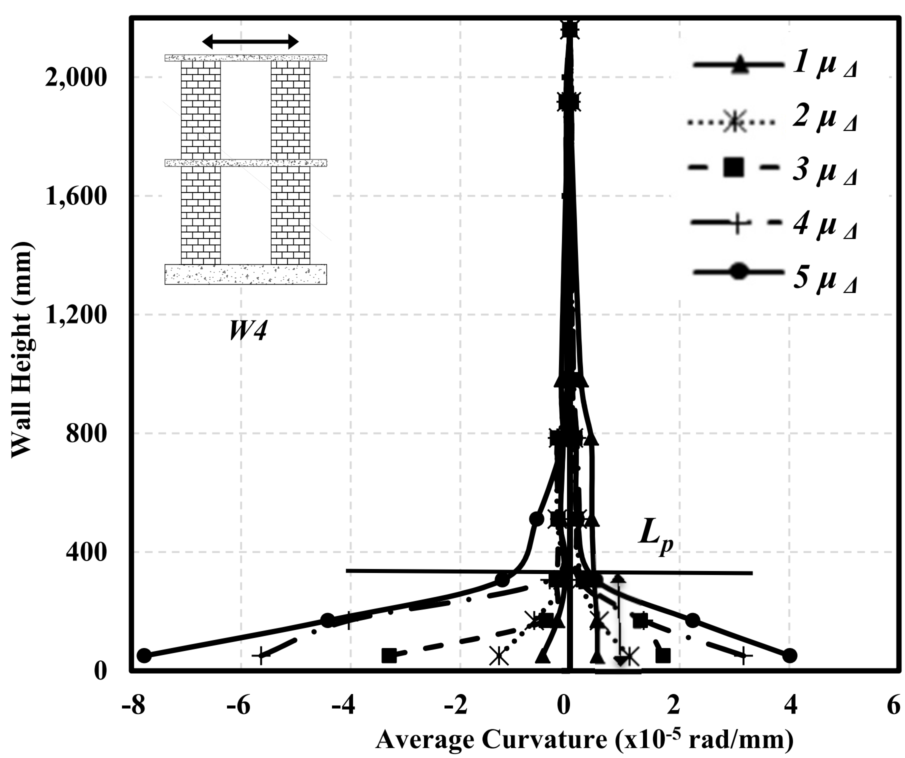

1 μ Δ
2 μ Δ
3 μ Δ
4 μ Δ
5 μ Δ
W4
L p
Wall Height (mm)
Average Curvature (x10-5 rad/mm)

(d)

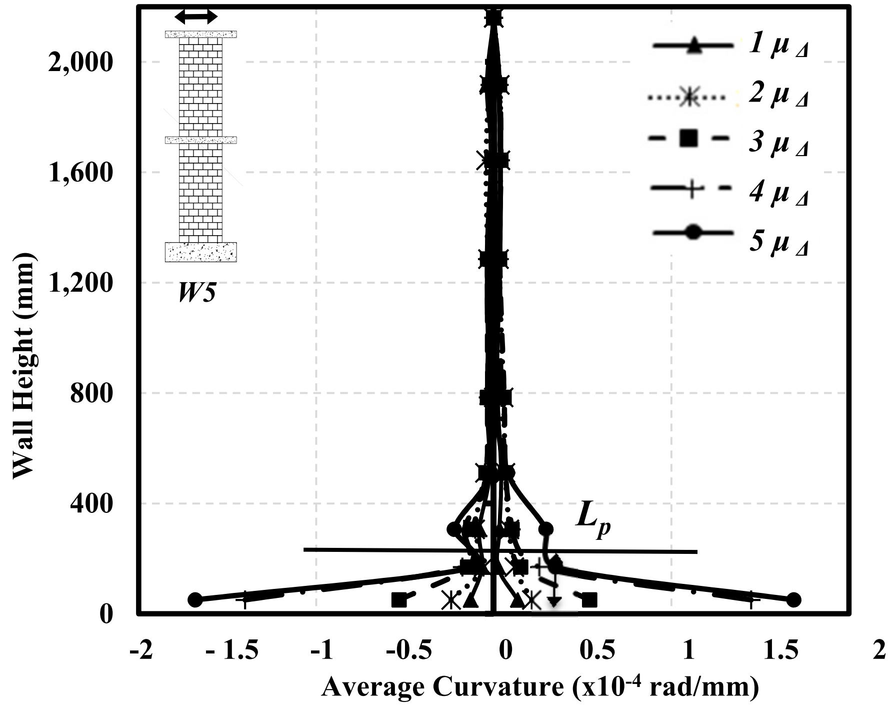

(e)

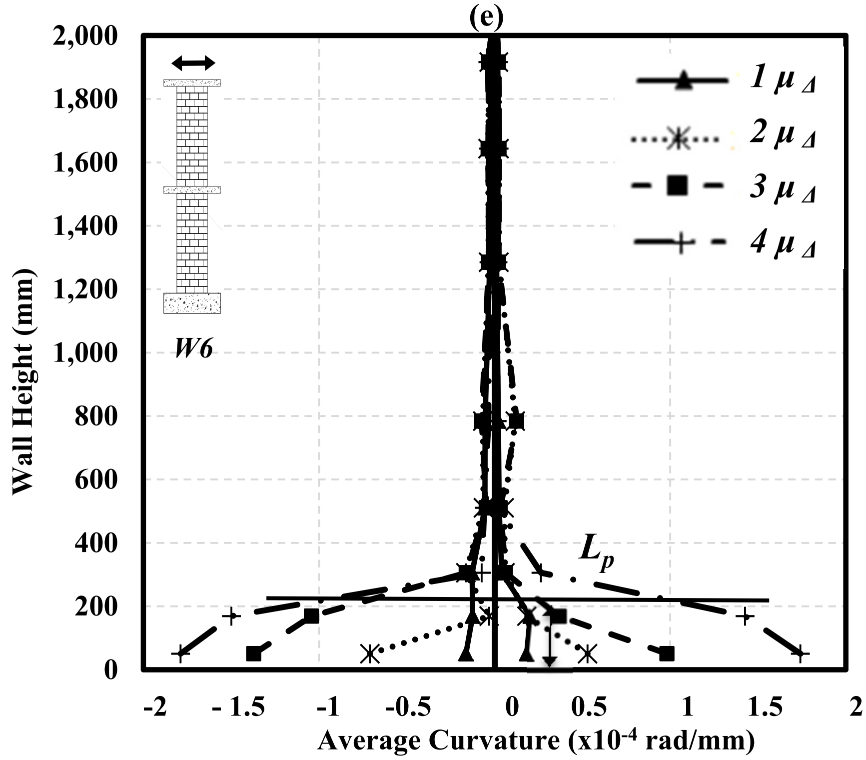

(f)

Fig. 3.8. Average curvatures over wall height: (a) W1; (b) W2; (c) W3; (d) W4; (e) W5; (f) W6

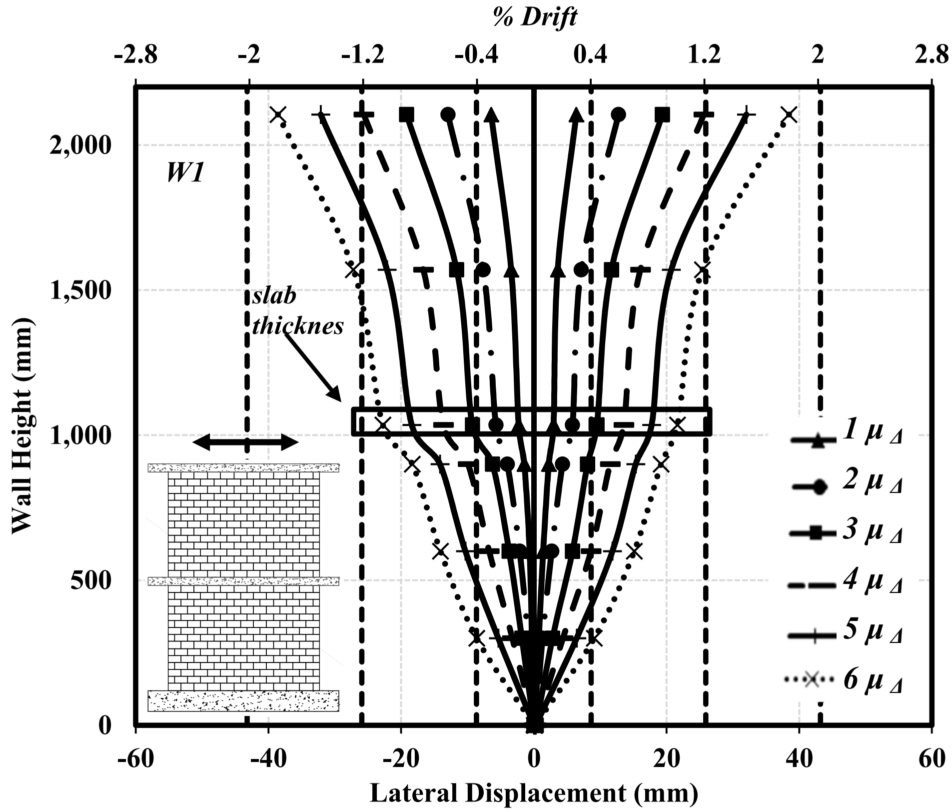
% Drift
-2.8
-2
-1.2
-0.4
0.4
1.2
2
2.8
W1
slab thicknes
Wall Height (mm)
2,000
1,500
1,000
500
0
1 μ Δ
2 μ Δ
3 μ Δ
4 μ Δ
5 μ Δ
6 μ Δ
-60
-40
-20
0
20
40
60
Lateral Displacement (mm)

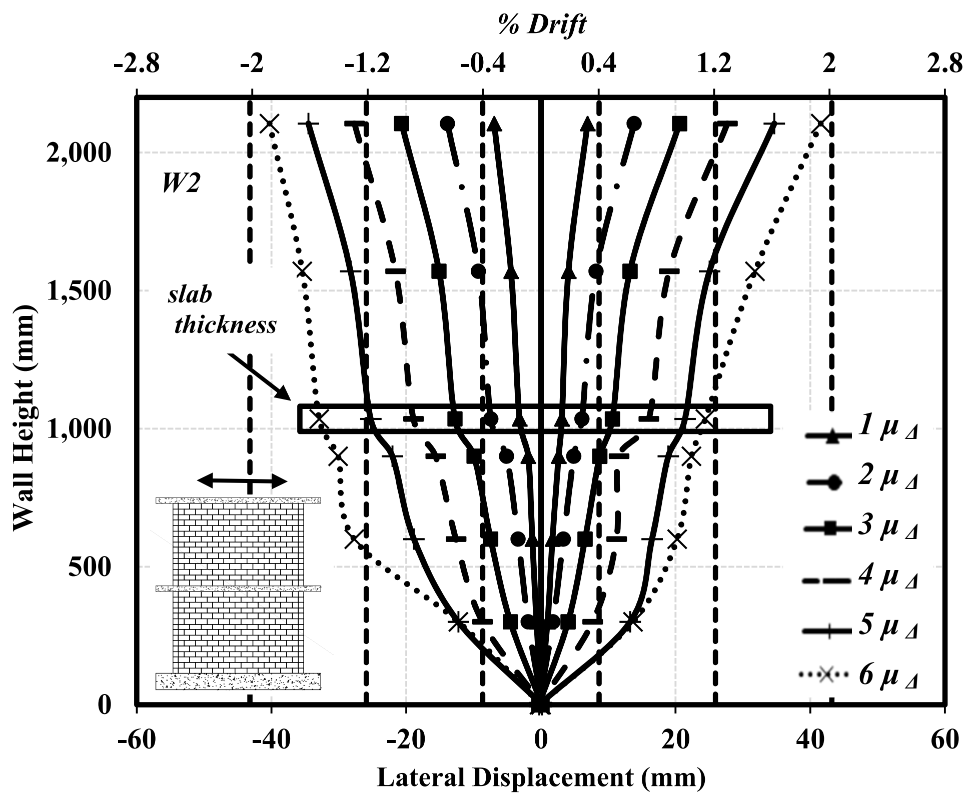
% Drift
-2.8
-2
-1.2
-0.4
0.4
1.2
2
2.8
W2
slab thickness
Wall Height (mm)
2,000
1,500
1,000
500
0
1 μ Δ
2 μ Δ
3 μ Δ
4 μ Δ
5 μ Δ
6 μ Δ
-60
-40
-20
0
20
40
60
Lateral Displacement (mm)

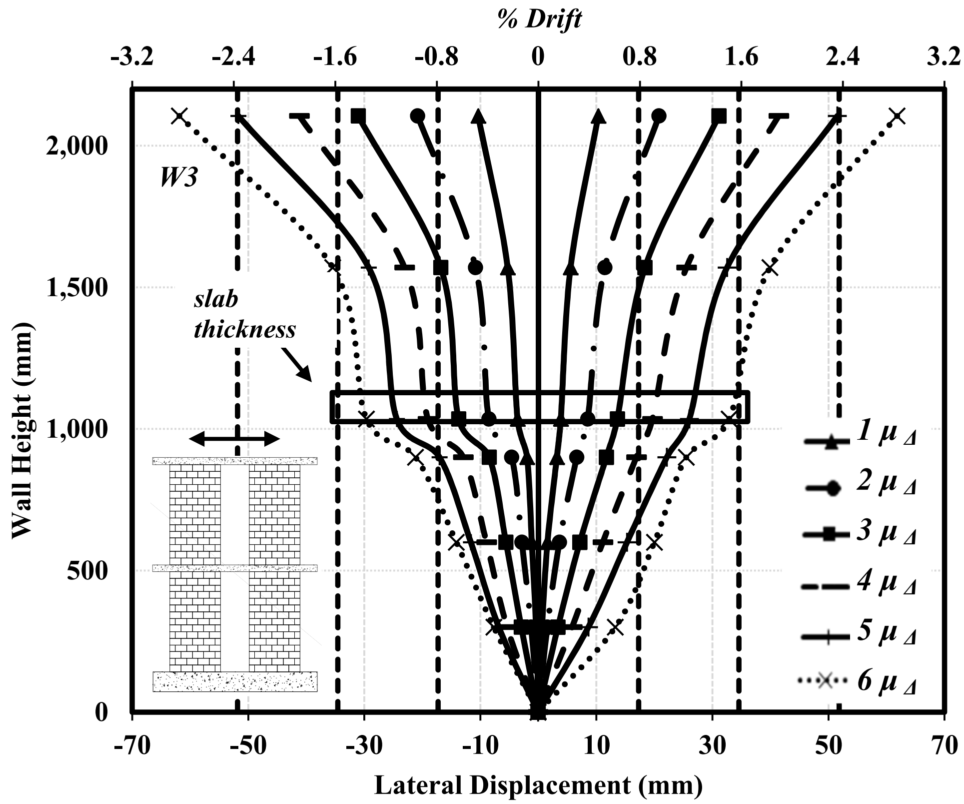
% Drift
-3.2
-2.4
-1.6
-0.8
0
0.8
1.6
2.4
3.2
W3
slab thickness
Wall Height (mm)
2,000
1,500
1,000
500
0
1 μ Δ
2 μ Δ
3 μ Δ
4 μ Δ
5 μ Δ
6 μ Δ
-70
-50
-30
-10
10
30
50
70
Lateral Displacement (mm)

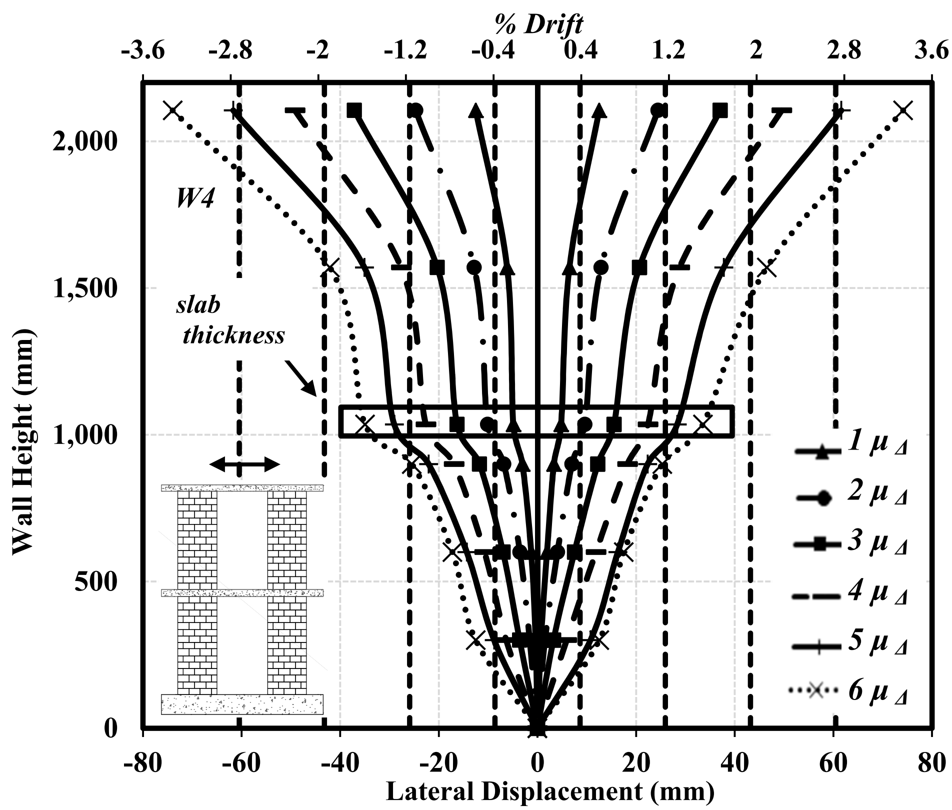
% Drift
-3.6
-2.8
-2
-1.2
-0.4
0.4
1.2
2
2.8
3.6
W4
slab thickness
Wall Height (mm)
2,000
1,500
1,000
500
0
1 μ Δ
2 μ Δ
3 μ Δ
4 μ Δ
5 μ Δ
6 μ Δ
-80
-60
-40
-20
0
20
40
60
80
Lateral Displacement (mm)

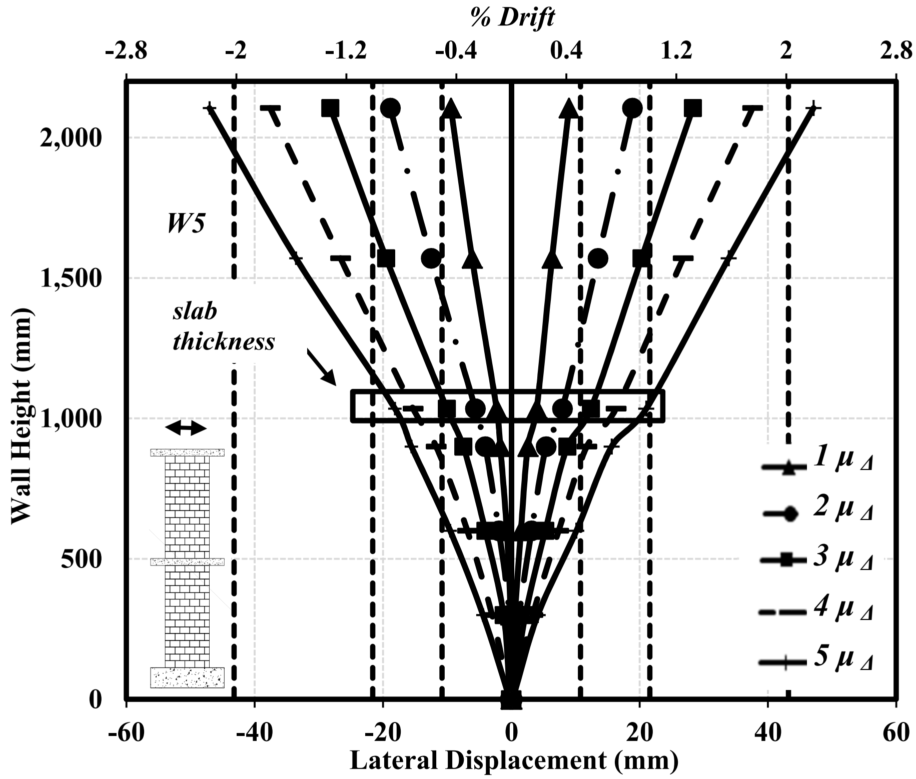

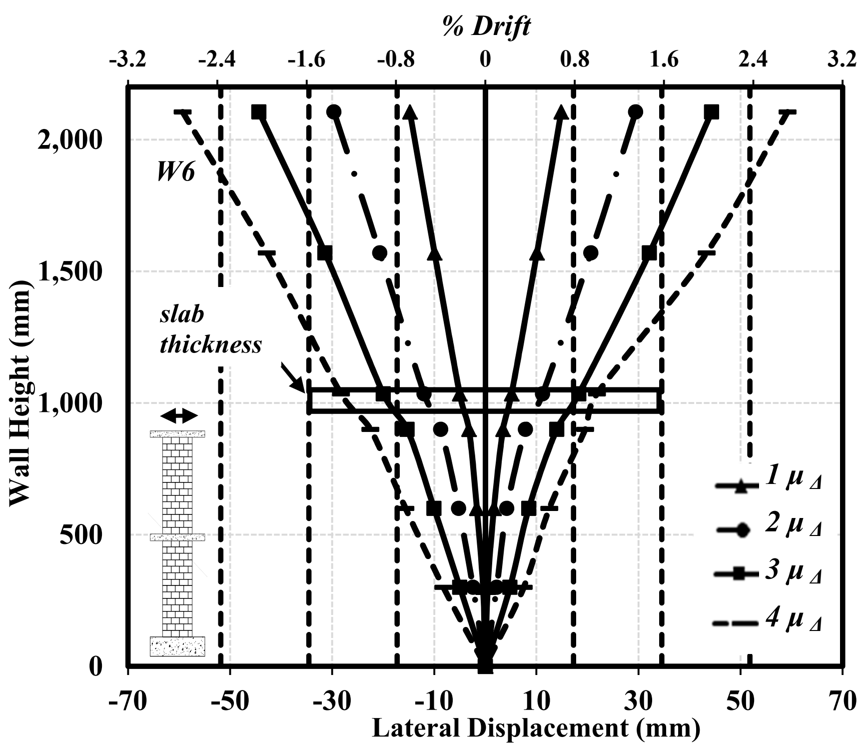

Fig. 3.9. Wall height against lateral displacements: (a) W1; (b) W2; (c) W3; (d) W4; (e) W5; (f) W6

CHAPTER 4: COLLAPSE FRAGILITY EVALUATION OF DUCTILE REINFORCED CONCRETE BLOCK WALL SYSTEMS FOR SEISMIC RISK ASSESSMENT

ABSTRACT: Seismic risk assessment is a critical first step towards mitigating the social and economic losses resulting from earthquakes. The FEMA P-58 document, prepared by the Applied Technology Council, provides a methodology for seismic performance assessment of buildings. The methodology consists of five main tasks: assembling the building performance model, defining earthquake hazards, analyzing building response, developing collapse fragility, and finally quantifying performance. Owing to the probabilistic nature of the methodology framework, each step incorporates uncertainty. After the 2011 Christchurch earthquake a significant number of reinforced masonry low-rise buildings were deemed unusable, although the damage was repairable. This raised a concern about investigating the seismic collapse performance of a Reinforced Masonry Shear Wall System (RMSWS) through the FEMA P-58 methodology to evaluate its seismic vulnerability. A typical reinforced concrete block office building designed according to the National Building Code of Canada (NBCC) 2010 and the Canadian Standards Association (CSA) S304-14 masonry design code provisions was used to examine the performance of such a system. In order to achieve the goal of the study to develop collapse fragility curves for RMSWS, an analytical model to predict the behaviour of a RMSWS was developed. The model was calibrated using experimental results presented earlier in Chapter 2 on the scaled RMSW. Subsequently, an incremental dynamic analysis (IDA) was performed to study the RMSWS system's performance under a suite of ground motions consistent with the NBCC 2010 design spectrum for a high seismicity site in Victoria, British Columbia. Results of IDA were used to develop collapse fragility curves for the RMSWS system in order to facilitate quantifying the risk of such building systems under different levels of seismic demand.

Keywords: Analytical model**,** Collapse, Fragility curves, Incremental dynamic analysis, Reinforced masonry, Structural walls, Seismic performance, FEMA P-58, FEMA P-695.

4.1 INTRODUCTION

Seismic risk assessment (SRA) is a critical first step towards mitigating the social and economic losses resulting from earthquakes. In the ongoing effort toward the development of next-generation performance-based seismic design (PBSD) criteria and guidelines, the Applied Technology Council (ATC) developed the FEMA P-58 (ATC 2012) methodology for seismic performance assessment of buildings. The methodology includes, assembling the building performance model, defining earthquake hazards, analyzing building response, developing collapse fragility, and finally quantitatively assessing the building performance. Such quantification of performance in terms of meaningful metrics, such as probable casualties, repair costs, and downtime, facilitates the decision-making process for stakeholders (building owners, government officials, users, etc.) (Hamburger 2014).

In this respect, a significant number of reinforced masonry (RM) structures were deemed unusable following the 2011 Christchurch earthquake, even after realizing that the damage was repairable. It was worth investigating the reason for such decisions because experimental and field studies have demonstrated the ductile performance of RM seismic force resisting systems (SFRS) under different levels of seismic demands. Haach et al. (2010) studied the seismic behaviour of RM walls tested using trussed vertical and horizontal reinforcement. The study showed that the presence of horizontal reinforcement improved the distribution of cracks, even if the increase in lateral strength was marginal. Shedid et al. (2010a and b) performed cyclic tests on scaled RM shear walls with various configurations and aspect ratios and analyzed the walls' seismic behaviour. Shedid et al. (2010a) concluded that higher ductility values than those currently adopted in the current North American codes should be used for walls with rectangular cross sections. Shedid et al. (2010b) also concluded that flanged and end confined RM walls can be cost-effective alternatives to enhance the seismic performance of midrise RM construction in North America. Banting and El-Dakhakhni (2012) reported on the performance of RM structural walls detailed with confined boundary elements and subjected to fully reversed cyclic loading. The study showed experimental evidence of the superior seismic performance of this type of RM SFRS category compared to RMSW with typical rectangular cross sections.

Heerema et al. (2014) studied the seismic response of an asymmetric RM-SFRS and how it compares with the component level behaviour. The study provided useful benchmarking data that contributes to the understanding of the relation between component- and system-level performance of RM SFRS respectively. Ahmadi et al. (2014) performed an experimental study to analyze the seismic behaviour of cantilever RM walls. The study concluded that similar behaviour exists between walls constructed with recycled units and ordinary units. Moreover, it showed that lap splices in the longitudinal reinforcement can negatively affect the RMSW performance and that walls with concentrated longitudinal reinforcement behaved similarly to walls with distributed reinforcement. The previous chapters evaluated force-, displacement- and performance-based seismic design parameters of RMSW classified as *ductile shear walls/special reinforced wall*s according to Canadian CSA S304-14 (CSA 2014) and the American MSJC-13 (TMS-402/ACI-530/ASCE-5) masonry design provisions. The chapters highlighted the fact that RMSW detailed following the same prescriptive code requirements for *ductile shear walls* SFRS can experience significantly different force-, displacement- and performance-based seismic design parameters at the component-level depending on the wall configuration.

Recent studies focused on collapse fragility assessment for different types of SFRS subjected to different earthquake effects. Azarbakht et al. (2012) investigated the effect of ground motion spectral shape parameters on collapse fragility curves. The study proposes a closed form formula to predict the collapse capacity of structures as a function of their structural behaviour parameters (i.e. spectral shape parameters). Li and Van De Lindt (2014) developed collapse fragility curves for a special moment-resisting steel frame with fully restrained reduced beam sections after being subjected to a level of damage from a main shock. This was done to investigate the effect of aftershocks on these types of structures. The study concludes that the structural collapse capacity may reduce significantly when the building is subjected to high intensity main shocks. Nazari et al. (2014) conducted a similar study on a two storey wood frame town house to investigate the effect of aftershocks on these types of structures. The study shows that the building model generated to represent the wooden structure does not suffer critical effects from the after-shocks if it has survived the main shock. This indicates that the effect of aftershocks on the collapse of low-midrise wood frame buildings is not as significant as perceived. Purba and Bruneau (2015) conducted collapse assessment of steel plate shear walls (SPSWs) having infill plates using two different design philosophies. They concluded that infill plates for SPSWs should be designed to resist the total specified storey shears and that SPSWs designed by sharing storey shears between the boundary frame and infill plates will undergo significantly larger drifts (Purba and Bruneau 2015).

As there is no current study that analyzes the seismic performance of RM SFRS using a well-defined methodology, the current study focused on performing a seismic performance assessment of RM SFRS, following the FEMA P-58 and P-695 procedures, to assess the RMSW system-level seismic vulnerability. This is thought to correlate better with the objectives of the next generation PBSD since the seismic performance of the whole building system is investigated. There is currently no performance-based methodology to evaluate the seismic performance of RM SFRS in Canada, the FEMA P-58 and P-695 procedures were followed using Canadian design spectrum-consistent records that have been used to generate seismic hazard curves (Assatourians and Atkinson 2010) for the NBCC (NRCC, 2010).

As building collapse is the principal cause of earthquake causalities, the FEMA P-58 (ATC 2012) presents a procedure for collapse fragility assessment and the development of collapse fragility curves, which describe the probability of incurring structural collapse as a function of ground motion intensity (ATC 2012). The procedure involves the selection and scaling of a suite of ground motions. In this study, a total of 15 simulated ground motion pairs were used and matched to the NBCC (2010) target design response spectrum, corresponding to a highly seismic site according to Canadian seismology in Victoria (Gonzales Heights), British Columbia, Canada. A considerable portion of the study focused on the development of an analytical model that was used to perform an incremental dynamic analysis (IDA) with the selected ground motions suite. The details of using IDA as a method for collapse assessment of structures are explained in details in Vamvatsikos and Cornell (2002). Results from the IDA were then used to generate collapse fragility curves for the RM SFRS. The following sections discuss the building design and configuration and give a brief summary of the experimental program and test results as presented in Chapter 2 and 3. The study also gives the details of the developed inelastic model characteristics and the relevant analysis methodologies utilized to evaluate the collapse fragility and adjusted collapse margin ratio of a typical RM structure.

4.2 BUILDING DESIGN CONFIGURATION

A typical RM SFRS, as shown in Fig. 4.1, was used in the study. The building plan shows that the SFRS consists of four different RMSW configurations: W1, W2, W5 and W6. For ease of cross-referencing, the same wall designation, presented in Chapter 2 was used herein. Walls W1, W5 and W6 have rectangular cross-sections, while W2 is flanged. The walls shown at the corners of the building are not connected to maintain consistency with the walls tested in the experimental program. Figure 4.1 shows that the SFRS in the N-S direction is made of Walls W1, W5 and W6a. Table 4.1 lists details pertaining to each wall where all walls are classified as *ductile* and *special* according to the CSA S304-14 (CSA, 2014) and the MSJC-13 (MSJC, 2013), respectively. As shown in Table 1, the horizontal reinforcement ratio for all walls is 0.26% at the first storey, and 0.14% at the second storey, following the capacity design philosophy. The walls are full scale versions of the walls tested in the experimental program, keeping the material properties the same to facilitate calibration of the analytical model discussed in the next sections. The seismic forces were transferred to the shear walls through a rigid diaphragm action via reinforced concrete (RC) floor slabs, 20 cm in thickness. The building was designed according to the NBCC 2010 (NRCC, 2010) and CSA S304-14 (CSA 2014) code requirements.

4.3 SUMMARY OF PREVIOUS WORK

The experimental program in Chapter 2 focused on evaluating the seismic response of six, fully-grouted, RM shear walls subjected to reversed cycles of quasi-static loading. The aspect ratios and steel reinforcement ratios of the third-scale model walls are the same compared to those of the prototype walls, presented in Table 4.1, in which the vertical and horizontal steel ratios, and the vertical and horizontal bar diameters, are denoted by, ρ_v, ρ_h, d_v and d_h, respectively. In general the experimental results showed that the *ductile*/*special* RMSW failed in a flexural manner reaching a displacement ductility level, at 20% strength degradation, between 5.4 and

7.6. The results also showed that RM shear walls detailed following the same *ductile*/*special* RMSW classification, and having the same overall aspect ratio and reinforcement ratio, could experience significantly different seismic design parameters and may have different ductility capacities depending on different wall configurations. Further details of the test program, the experimental results, and the evaluated seismic design parameters can be found in Chapters 2 and 3.

4.4 ANALYTICAL MODEL

4.4.1 Model Development and Modelling Process

A modelling process, shown in Appendix G was established to create the RM SFRS model representing the N-S SFRS of the building in Fig. 4.1. The process starts by development of scaled wall stick models using OpenSees (McKenna et al., 2000) platform to simulate the inelastic flexural behaviour of the walls. Details of the model are discussed in this section. In step 1, numerical models of the scaled walls are created in Opensees. In steps 2 and 3 calibration of the model is carried out by comparing the results of the numerical model for Wall W5 to the experimental hysteresis results for that wall. The parameters that are adjusted include some of the parameters in the material models, as well as the number of elements used in the numerical model. If the model compares well with the experimental results then the next step is to move on to model the other scaled walls. Otherwise the modeller has to return to step 1. In step 5, the wall models from step 1 are scaled up to represent full scale walls. Step 6 involves checking the flexural capacity of the wall by comparing full scale model pushover analysis with flexural analysis using simple mechanics. Once confirmed, one can proceed to step 7, otherwise the model is not appropriate and the modeller should return to step 1. Step 7 then involves assembling the RM SFRS model using full scale wall stick models to represent the RM building in Fig 4.1. During this step selection and scaling of ground motion can be completed concurrently. Once the SFRS model and estimation of ground motion are ready, one can proceed to step 8. This step includes conducting incremental dynamic analysis (IDA) to generate IDA curves. Step 9 involves post processing of results obtained from the IDA results. In order to make this process more efficient, a Matlab codes was developed to obtain the maximum inter-storey drift from each ground motion input and plot maximum inter-storey drift against the intensity measure chosen ($S_a(T_1)$). The plot is described in the following sections.

To begin with, the calibrated scaled model will be first described followed by a discussion regarding the RM SFRS model. The numerical model is a 1D fiber-based macro model developed by Ezzeledin et al. 2014 in collaboration with the author. Macro modelling was adopted because the study focuses on the global response of the SFRS, and because the model will be used in a computationally intensive nonlinear time history analysis (NLTHA). Moreover, macro-modelling of shear walls using fiber elements have shown considerable accuracy when modelling shear wall systems (Waugh and Sritharan 2010). Each fiber element is a displacement-based beam-column element. The element is based on the displacement formulation and therefore considers the spread of plasticity along the element (McKenna et al., 2000). Additionally, this formulation assumes a constant axial strain and a linear curvature distribution. Most fiber elements do not account for the effect of shear deformations that occur due to lateral load, although experimental research shows that the flexure and shear displacements are coupled for most of the walls, even for walls with relatively high aspect ratio (Massone and Wallace 2004). Subsequently, since such walls exist in the modelled building, it was necessary to account for shear deformations in the adopted model. Therefore, the shear deformations in the walls were aggregated using a uniaxial material model available in the OpenSees (McKenna et al., 2000) platform (Pinching 4 material) to facilitate accurate predictions of wall displacements. Pinching 4 is a one-dimensional hysteretic load deformation response model that involves a response envelope, an unload-reload path and three damage rules that control the evolution of these paths (Lowes et al. 2003). Global material response parameters describing the walls' load-displacement envelopes are estimated and used as input for the Pinching 4 material. The forces global parameters indicated in Fig H-1 (Appendix H) as ePf1, ePf2, ePf3 and ePf4 were estimated using mechanics based flexural analysis of shear walls including the self-weight of the walls. On the other hand, the displacements illustrated in the same figure as ePd1, ePd2, ePd3 and ePd4 were estimated using deflection calculation of cantilever walls with top load application taking into account flexural and shear displacements when calculating the gross stiffnesses of the walls.

As shown in Fig. 4.2, the system is discretized into six walls to represent the RM SFRS aligned along the building's N-S direction. Since the building is symmetrical, only half of the building was modelled. Each wall is discretized into seven elements in total, five elements are distributed along the first floor, one element represents the top storey, and a zero-length section element is added at the wall-foundation interface (see Fig. 4.2). The rationale for this discretization is to facilitate capturing the hinging mechanism that develops in the bottom storey and to model the tensile strain penetration that occurs below the wall base level. The model had a total of 48 nodes, 42 displacement beam-column elements, 10 elastic truss elements and 12 lumped masses. The masonry was modelled using the Concrete 7 model, which represents the simplified Chang and Manders (1994) material (Appendix H, Fig. H-2). The vertical reinforcement was modelled using the Steel 02 material model (refer to Appendix H, Fig. H-3), which represents uniaxial Giuffre-Menegotto-Pinto steel material (Menegotto and Pinto 1973). Bond_SP01 material was added to model the effect of tensile strain penetration of the vertical reinforcement. The parameters used in each material model are explained in the subsequent section.

The following assumptions were made in the development of the fiber-based element model:

1. The walls were fixed at their bases, assuming a rigid foundation system.

2. Floor masses were assumed to be lumped at each floor level at the center of the walls. Assuming a total area of the building of 750 m^2, the mass and axial load assigned to each wall at each node discretized was calculated and shown in Table 4.2.

3. The axial loads were calculated according to the tributary area method using the NBCC 2010 (NRCC, 2010) load factors and combination. Similarly, the masses were calculated where the highest masses were assigned to the stiffest wall because it will attract most of the seismic force. The mass of each wall relative to the mass of the first floor is depicted in Table 4.1. Summing the total ratios of the walls resisting half of the first floor's mass, result in a relative mass of 17%.

4. The floor-slab systems were modelled using rigid elastic truss elements with high axial stiffness. Table 4.2 shows that the elastic stiffness (E_{slab}) of the slabs is almost 20 times as stiff as the walls (E_m). Such floor-slab system will cause the walls to behave as cantilevers where all the nodes within the same floor level displacing equally; assuming displacements are small and occurs horizontally.

5. Only the horizontal ground motions were taken into consideration in modelling the RM SFRS using NLTHA.

4.4.2 Model Parameters Evaluation and Calibration

It is crucial to make the distinction between the strength parameters that were used in the scaled and full scale models respectively (steps 1 and 5 in Appendix G). In the scaled model, material parameters obtained from experimental testing of the masonry constituents were used. On the otherhand, for the full scale model, design values from Canadian code provisions were used to define the material parameters.

The Concrete 7 material model in OpenSees (McKenna et al., 2000) was used to define the masonry material with values of f'_m and strain at peak load, ε_m. Currently there is no material model developed to simulate the behaviour of masonry and therefore the Concrete 7 model in OpenSees was used for this purpose. There is a distinction that should be madIn this concrete model (Step 2 in Appendix G), the parameters *xp* and *xn* shown in Table 4.3 were calibrated to accurately model the masonry material. These two parameters define the strain at which the straight line descent begins in tension, and compression respectively (Appendix H). The *r* parameter accounts for the nonlinear descending branch in the curve. It is important to note that values of f'_m and ε_m in Table 4.3 correspond to the full scale wall model (Step 5 in Appendix G). These values were used in the design calculaitons of the RM building as discussed earlier. The vertical steel material parameters included the yield strength, f_y, and the strain hardening coefficient, *h*. The parameters *R0*, *cR1* and *cR2* were calibrated with values shown in Table 4.3 to best simulate the cyclic behaviour of the rebars. The parameters in Bond_SP01 material include, the yield and ultimate strengths, f_y and f_u, respectively, the rebar slip at member interface under yield stress, S_y, the rebar slip at the loaded end at the bar fracture strength, S_u, the initial hardening ratio in the monotonic slip vs bar stress response, *g*, and the pinching factor for the cyclic slip vs bar response, *R*. Parameters *g* and *R* which were calibrated.

The Pinching 4 material was also used to describe the load degradation behaviour past the peak load and the pinching behaviour within the hysteresis loops. Discrete load and displacement points were estimated in the Pinching 4 material to represent the limits of the backbone curve (Appendix H, Fig. H-1). As mentioned previously, the load estimations of the Pinching 4 material were calculated using flexural analysis of the walls while the displacement points were estimated using elastic deflections of the walls using the gross stiffness and accounting for flexural and shear deformations. Moreover the number of elements representing the first floor of the wall was calibrated to simulate the hinging mechanism at the bottom section of the walls. A total number of six elements (excluding zero length element) were sought sufficient after doing a sensitivity analysis for the choice of an optimum number of elements.

The calibrated numerical model was compared to the experimental results of the two-storey RMSW (hysteresis loops) presented in Chapter 2. This fiber-based model was used to generate hysteretic relationships for three rectangular scaled walls, W1, W5 and W6 of the test specimens presented in Chapter 2. The same loading protocol used for the experimental program was used to compare between the numerical and experimental models. Figure 4.3 shows comparisons between the experimental and the numerical model hysteresis loops for the walls. Moreover, Table 4.4 compares the model strength predictions with the corresponding experimental values at specified displacement cycles given as the input to the model. As shown in Fig. 4.3 and Table 4.4, the model captures the experimental response with excellent accuracy (10-30%) for Walls W5 and W6, which have high aspect ratios. The numerical result for Wall W1 matches the experimental ones for the first five cycles, and then the accuracy decreases for the last cycle (i.e. sixth). In general the model is able to capture the inelastic behaviour of the RM shear walls. As described earlier in the modelling process, after calibration, step 5 commenced where the walls were scaled up to represent full scale walls. Pushover analysis was performed on the full scale wall models and compared with theoretical calculation of flexural strength. The results were presented in Table 4.5 showing the agreement between the yield and ultimate lateral load capacities of the S304-14 code and the numerical model. Consequently step 7 from the process was performed, to assemble the full scale RM walls to form the building model shown in Fig. 4.2. At this stage, the selection and scaling of ground motions was performed concurrently which will be discussed in the next section.

4.5 METHODOLOGY AND DISCUSSIONS

4.5.1 Selection of Ground Motions Suite

A set of representative ground motion pairs were used to estimate the intensity measure, *IM*, adopted within the seismic fragility assessment, following the FEMA P-58 guidelines. Three sets of 45 simulated ground motions from Assatourians and Atkinson (2010) were used as a basis to obtain several Canadian design spectrum-consistent records for the region of interest located in Victoria (Gonzales Height), British Columbia. From a total of 135 simulated earthquakes, 30 earthquakes (15 pairs) denoted by west6c1, west6c2 and west7c2 (Table 4.6), respectively, were selected for the IDA. The characteristics of the selected earthquakes reflected the seismicity in the western Canada region (shallow crust or within the underlying subducting slab earthquakes) as described in Adams and Halchuk (2003) and Adams and Atkinson (2003).

In the current study, the *intensity-based performance assessment* procedure in FEMA P-58 (ATC 2012) was used for ground motion selection and scaling. This procedure involves evaluating the performance of the RM SFRS aligned along the N-S direction under an acceleration response spectrum. The procedure requires first the selection of a target response spectrum to which the response spectra of the simulated ground motions are to be matched. Subsequently, the candidate suite of 15 ground motion x-y pairs was obtained from those described in Assatourians and Atkinson (2010). The western Canada suite contains elastic response spectra with 5% damping and their corresponding time histories at magnitudes ranging between 6.5 and 7.5, for site class C and focal distance varying between 10 to 100 km. Then the geometric mean spectrum, S_{gm} given by Eq. 4.1 is computed for each ground motion pair over the period range between T_{min} = 0.04s and T_{max} = 0.54s (see Fig. 4.4), where S_x and S_y are orthogonal components of spectral acceleration at period T. S_{gm} is used since most of ground motion prediction equations provide geometric mean spectral response accelerations (ATC 2012).

$$S_{gm}(T) = \sqrt{S_x(T)\, S_y(T)} \tag{4.1}$$

The target response spectrum is shown in Fig. 4.4. The selected ground motion pairs had geometric mean response spectra with shapes similar to the target response spectrum over the range of interest ($T_{min} \leq T \leq T_{max}$). The average mean response spectrum (50th percentile) along with that for the 16th and 84th percentiles are also shown in Fig. 4.5. The final step involves scaling each ground motion pair by the ratio of $S_a(\overline{T})$ to the $S_{gm}(\overline{T})$, where $\overline{T}$ = 0.22s is the average fundamental period from the orthogonal directions (x and y) of the building. The scaled ground motions are then used in the IDA of the N-S RM SFRS.

4.5.2 Estimation of System Capacity: Pushover, Hysteretic Relationship

The system pushover curve for N-S RM SWS is plotted in Fig. 4.5(a). The curve was computed by subjecting the N-S SFRS to constant displacement increments of 6 mm imposed at the roof level (see Fig. 4.2). The graph also shows the pushover curve obtained from superimposing the pushover curves of the individual walls as shown in Fig. 4.5(b). The N-S SFRS have a higher ultimate load capacity (normalized base shear of 0.52) as compared to the summation of the lateral load capacities at the corresponding IDR_{max} of 0.47%. The hysteresis loops from cyclic analysis of the model is also shown in the Fig. 4.5(c) using the loading protocol illustrated in the same figure. The lateral load capacity from cyclic analysis was lower by 15.4% than the pushover curve of the RM SWS at the corresponding IDR_{max} of 0.47%, indicating more damage induced in the structure due to repeated cycles.

4.5.3 Incremental Dynamic Analysis for Building Collapse Capacity and Response Histories

Inelastic demands for the RM building used in this study were determined using IDA, an important component of the FEMA P-58 methodology. The method was first developed by Luco and Cornell (1998) and explained in detail by Vamvatsikos and Cornell (2002). The method adopts a parametric analysis approach to estimate structural performance under seismic loads (Vamvatsikos and Cornell 2002). It involves performing a series of NLTHA in which the ground motion *IM* selected for collapse investigation is incrementally increased until the collapse of the SFRS is realized. Although multiplication of a real ground motion by a scale factor does not necessarily result in a physically realizable earthquake motion, it facilitates a better understanding of the behaviour of inelastic systems over a range of intensities (Konstantinidis and Nikfar 2015). Incremental dynamic analysis is graphically expressed by plotting what is known as IDA curves, also known as dynamic pushover curves, which are relationships between *IM* and the damage measure (*DM*). Such curves are produced by subjecting the structure to multiple ground motions, each ground motion scaled to multiple levels of intensity (Vamvatsikos and Cornell 2002).

The *IM* chosen in this study is the spectral acceleration (5% damping) at the fundamental period of the structure (T_1 = 0.2 s) denoted as S_a (T_1, 5%). The code-defined empirical period of vibration for shear wall structures ($T_n = 0.05h_n^{0.75}$) provided in the NBCC 2010 (NRCC, 2010) was used to calculate T_1. Ten intensity scale factors, from 1.0 to 5.5, with 0.5 increments, were chosen to generate the IDA curves starting with S_a (T_1, 5%) = 0.7g. The maximum inter-storey drift ratio (IDR_{max}), was used as the *DM* in this study. The IDA curves for the 30 ground motions along with 16th, 50th and 84th percentile IDA curves are illustrated in Fig. 4.6. The results of the data are shown in Appendix I. The interpretations from the data are summarized as follows:

1. The curves show that the N-S RM SFRS remains linear elastic at *IM* = 0.7g, reaching a maximum IDR of approximately 0.2%.

2. Different levels of intensity cause different responses of the RM SFRS (Fig. 4.6) where in some cases, the structure may exhibit a severe softening behaviour where a small increase in the *IM* causes a large increase in the *DM* (i.e. maximum inter-storey drift). The SFRS also shows a severe hardening behaviour (due to increase in stiffness) causing the structure to have lower drift levels at increasing levels of intensity (Fig. 4.6).

3. The collapse median intensity, θ, can be quickly estimated by locating the intersection of 50th percentile IDA curve with the vertical line of the x-axis (IDR_{max}) that defines collapse. This is depicted in Fig. 4.6, where θ was estimated roughly to be 2.7g.

4. Results from IDA curves were used to generate collapse fragility curves after defining the specific collapse state of the structure.

Figure 4.7 shows the computed weight-normalized base shear against the IDR_{max} response for two ground motions (records 1 and 6 in Table 4.6) with increasing levels of intensity: 0.7g, 1.6g and 2.6g. The figure shows the transition of the structure into the inelastic range with increasing *IM*. At *IM* = 0.7g, the structure remains elastic, reaching maximum IDR of 0.2%. As the *IM* increases to 1.6g, the structure deforms inelastically past its maximum load capacity at IDR_{max} of 0.5%, resulting in significant residual drifts from this point on.

4.6 COLLAPSE FRAGILITY ASSESSMENT

Fragility curves can be generated using several approaches including field observations or experimental testing, static structural analysis or through expert judgment (Kennedy and Ravindra 1984, Kim and Shinozuka 2004, Calvi et al. 2006; Villaverde 2007, Porter et al. 2007, Shafei et al. 2011). This chapter focused on deriving analytical fragility curves called collapse fragilities which are developed from NTHLA. In general terms and based on FEMA 461 (ATC 2007) definition, fragility functions are mathematical functions that define the conditional probability that a system or a component will experience damage equal to or exceeding a specific damage state (*DS*) given that the component or system experiences certain level of demand normally expressed as damage measure (*DM*). They are used as tools to assess the performance of individual components, or systems containing these components when subjected to loading caused by earthquake ground motion (ATC 2007). Recently, collapse fragility curves obtained from IDA results have been becoming increasingly popular in structural assessment procedures (ATC 2012) since protection against collapse is a crucial objective in performance-based seismic design. A collapse fragility function can be described mathematically as (Baker 2014):

$$P(C \mid IM = x) = \Phi\left(\frac{\ln(x/\theta)}{\beta}\right) \tag{4.2}$$

Where P (C | IM =x) is the probability of collapse given an intensity measure, i.e., $IM = S_a(T_1, 5\%) = x$, Φ is the standard normal cumulative distribution function, θ is the collapse median intensity (i.e. the *IM* level with 50% probability of collapse), and β is the standard deviation of the *IM*. Equation 4.2 implies the assumption of log normality of the *IM* values of the ground motions causing collapse of a specific structure (Baker 2014). This assumption was considered a reasonable assumption according to a number of researchers (Ibarra and Krawinkler 2005, Porter et al. 2007, Bradley and Dhakal 2008, Ghafory-Ashtiany et al. 2010, Eads et al. 2013). Collapse fragility curves are used for collapse safety assessment of building structures. Using such curves, the probability of collapse at a specific level of earthquake hazard can be predicted. The next section outlines how to identify collapse from IDA.

4.6.1 Identifying Collapse State from IDA

Defining collapse of a SFRS is an essential step for creating collapse fragility curves. According to FEMA P-58 (ATC 2012), a SFRS collapse is defined as: sideway failure (lateral dynamic instability), or loss of vertical-load-carrying-capacity, or exceedance of non-simulated failure criteria. In this study, two methods were used to define the collapse state of the SFRS. The first method defines collapse to occur when a certain limit along the x-axis of the IDA curve, i.e. the *DM* (IDR_{max}), has exceeded and is referred to as the *DM-based rule* in Vamvatsikos and Cornell (2002). The other method defines collapse to occur when a certain limit along the y-axis of the IDA curve, i.e. the *IM* ($S_a(T_1, 5\%)$), has exceeded and is referred to as *IM-based rule*. The methods are described in details in Vamvatsikos and Cornell (2002) and are reviewed herein briefly.

Researchers have proposed several types of damage measures for wall components. Some involve displacement-based measures such as maximum drift ratio and maximum top displacement, while others prefer energy-based measures that quantify the hysteretic energy at a given level of damage. Currently, FEMA 58-1 adopts the maximum inter-storey drift ratio to assess the level of damage attained by structural elements and SFRS. To be consistent with FEMA 58-1 guidelines, the collapse point is set to C_{DM} = 2.5% IDR_{max} for *DM-based rule*. This value is chosen conforming to the NBCC (NRCC, 2010) IDR limit set for collapse prevention. Being on the conservative side, the lowest *IM* value reaching such value will be defined as collapse. Figure 4.8 shows that there is 50% probability that RM walls will reach DS3 level. The three damage states, DS1, DS2, DS3, are defined in the FEMA P-58/BD-3.8.10 document (ACT 2009) showing the different failure stages of flexural-critical masonry shear walls. The damage state descriptions for RM walls in Table 4.7 are based on FEMA P-58. Table 4.8 shows the identification criteria of each damage state from load-displacement relationships respectively. DS1, DS2 and DS3 characterize slight, moderate and severe flexure damage respectively.

Another collapse assessment approach is to use the *IM-based rule*, as it can be argued that the SFRS might not collapse at the 2.5% IDR limit. In this method, the intensity separates the IDA curve into a collapse and a non-collapse region. The rule state that if $IM >= C_{IM}$, then the limit state is exceeded and collapse occurs (Vamvatsikos and Cornell 2002). The capacity point is defined by the 20% tangent slope *IM-based rule,* where the last point on the curve with a tangent slope equal to 20% of the elastic slope is regarded as collapse. The flattening of the IDA curve is used as an indication that collapse has occurred. As suggested by FEMA 350 (FEMA

2000), an inelastic stiffness level of 20% of the corresponding elastic value marks the capacity point. These two collapse definitions were utilized to generate collapse fragility curves as explained in the next section.

4.6.2 Collapse Fragility Fitting

Using the aforementioned definitions of collapse, the collapse fragility curves from IDA were computed for the N-S RM SWS, as shown in Fig. 4.9. The first step involved the use of IDA data to estimate two statistical parameters, the collapse median intensity, $\hat{\theta}$, and the dispersion of the *IM*, $\hat{\beta}$ (also known as record to record uncertainty) which are required to fit the fragility function corresponding to the corresponding results from IDA. Figure 4.9(a) shows the collapse fragility curves where collapse is defined using the *DM-based rule*, whereas Fig 4.9(b) plots collapse fragility curves for the *IM-based rule*. As shown in the figure, three methods were used to estimate these parameters, namely the method of moments estimator, the maximum likelihood method, and the least squares regression (Baker 2014, Cornell et al. 2002).

Method of moments

The method of moments involves estimating $\hat{\theta}$ and $\hat{\beta}$ by taking the logarithm of each ground motion's *IM* value associated with onset of collapse, which can be either *DM*- or the *IM-based rules*. Equations 4.3 and 4.4 can be utilized to compute these values (Baker 2014).

$$\ln \hat{\theta} = \frac{1}{n}\sum_{i=1}^{n} \ln IM_i \tag{4.3}$$

$$\hat{\beta} = \sqrt{\frac{1}{n-1}\sum_{i=1}^{n}(\ln(IM_i / \hat{\theta}))^2} \tag{4.4}$$

where n is the number of ground motions considered, and IM_i defines the IM value associated with the onset of collapse for the i^{th} ground motion. This method basically represents the mean (which is equal to the median in the case of log normality) and standard deviation of normally distributed ln IM values (Baker 2014). In this study, the $\hat{\theta}$ values computed using the *DM*- and the *IM-based rules* are 2.71g and 2.31g, respectively. The corresponding $\hat{\beta}$ values are 0.20 and 0.26. The collapse fragility curves generated using this method were plotted with dashed lines in Fig. 4.9.

Maximum likelihood method

The maximum likelihood fitting method uses the theoretical fragility function (see Eq. 4.2) and the binominal distribution function,

$$P(z_j \text{ collapses in } n_j \text{ ground motions}) = \binom{n_j}{z_j} p_j^{z_j}(1-p_j)^{n_j-z_j} \tag{4.5}$$

to formulate the likelihood expression (Baker 2014),

$$\text{Likelihood} = \prod_{j=1}^{m} \binom{n_j}{z_j} \Phi\left(\frac{\ln(x_j/\theta)}{\beta}\right)^{z_j} \left(1-\Phi\left(\frac{\ln(x_j/\theta)}{\beta}\right)\right)^{n_j-z_j} \tag{4.6}$$

assuming interdependence of collapse data between ground motions. In Eqs. (4.5) and (4.6), n_j denotes the total number of ground motions (30 in the current study), z_j the number of collapse at a specific intensity IM, and p_j the probability that a ground motion with $IM = x_j$ will cause collapse. The goal is to identify the fragility function that estimates p_j which can be done using the maximum likelihood method. The method identifies the fragility function that gives the highest probability of collapse as obtained from the IDA (Baker 2014). Estimates of the fragility function parameters, θ and β are denoted by $\hat{\theta}$ and $\hat{\beta}$. Such values are obtained by maximizing the logarithmic likelihood function as depicted in Eq. 4.7 (Baker 2014) as it is numerically easier to perform.

$$\left\{\hat{\theta},\hat{\beta}\right\} = \underset{\theta,\beta}{\arg\max} \sum_{j=1}^{m} \left\{ \ln\begin{pmatrix} n_j \\ z_j \end{pmatrix} + z_j \ln\Phi\left(\frac{\ln(x_j/\theta)}{\beta}\right) + (n_j - z_j)\ln\left(1-\Phi\left(\frac{\ln(x_j/\theta)}{\beta}\right)\right)\right\} \tag{4.7}$$

Where the *arg max* function represents the point of $\hat{\theta}$ and $\hat{\beta}$ for which the whole expression above attains a maximum value. Equation 4.7 was evaluated using a nonlinear solver tool generating values of 2.81g and 0.21 for $\hat{\theta}$ and $\hat{\beta}$ following the *DM-based rule* (i.e. C_{DM} defined at 2.5%). Following the *IM-based rule*, the method gives values of 2.76g and 0.48 for the same corresponding parameters. The *IM-based rule* shows higher dispersion signifying more uncertainty in the $\hat{\theta}$ value. Nevertheless the collapse median intensity values are in excellent agreement using both collapse rules. The fragility curves generated using the maximum likelihood method were plotted with solid lines in Fig. 4.9.

Least squares regression method

The IDR_{max} is assumed to depend on the *IM* following a power law,

$$IDR_{\max} = aIM^{b} \tag{4.8}$$

From the IDA results, the *IM*- versus the DM log-log data is shown in Fig. 4.10. Least squares regression (*LSR*) provides estimates of the regression parameters *a* and *b* in Eq. 4.8 as

a = exp(-0.959) and b = 1.805. Subsequently, Eq. 4.8 can be rearranged into

$$\ln\hat{\theta} = \frac{1}{b}\ln\left(\frac{IDR_{\max}}{a}\right) \tag{4.9}$$

which, assuming $\mathrm{IDR}_{max} = C_{DM}$ (2.5%), yields $\hat{\theta}$=2.83g. The dispersion of demand conditioned on the *IM* can be estimated using

$$\hat{\beta} \cong \sqrt{\frac{\sum_{i=1}^{n}\left(\ln\left(\Delta_i - \ln\left(aIM^b\right)\right)^2\right)}{n-2}} \tag{4.10}$$

which gives $\hat{\beta} \cong$ 0.18. With these values for $\hat{\theta}$ and $\hat{\beta}$, the fragility curve based on the *LSR* method was plotted with a dotted line in Fig. 4.9(a). Only the *DM-based rule* can be used when performing *LSR* method since a fixed collapse value of IDR_{max} is needed to solve for $\hat{\theta}$. The curve gives very close approximation to the maximum likelihood method where the fragility parameters values differ by 0.7% and 11% respectively.

Using the *DM-based rule* collapse definition, $\hat{\theta}$ and $\hat{\beta}$ lie between 2.71g and 2.81g, and 0.20 and 0.21, respectively. On the other hand, following the *IM-based rule* collapse definition, $\hat{\theta}$ and $\hat{\beta}$ lie between 2.31g and 2.76g, and 0.26 and 0.48, respectively. The *DM-based rule* shows more robustness as compared to the *IM-based rule* for collapse definition, where there are minor variations between the fragility statistical parameters. Being on the conservative side the lowest collapse median intensity of 2.31g with highest dispersion value of 0.48 were used to evaluate the performance and base the decision of the seismic vulnerability of the RM SFRS using the adjusted collapse margin ratio, as will be discussed in the next section.

4.6.3 Evaluating Performance of RM SFRS

Now that the collapse median intensity, $\hat{\theta}$, is obtained from the fragility fitting curves, the performance of the RM SFRS can be evaluated using the performance criteria outlined in FEMA P-695 document (ATC 2009b). Performance evaluation was defined by the collapse median ratio, *CMR* which is a measure of the probability of collapse. The ratio is formulated by dividing the collapse median intensity by the ground motion spectral demand, S_{MT} which is equal to 1.2 g at the fundamental period of the structure.

$$CMR = \frac{\hat{\theta}}{S_{MT}} \tag{4.11}$$

To be more conservative, the collapse median intensity using *IM-based* rule ($\hat{\theta}$= 2.31g) was used to calculate the *CMR* (*CMR* = 1.93). Moreover, in order to account for the effects of the spectral shape (i.e. frequency content) on the collapse capacity of the structure, the collapse margin ratio was modified. This was done by multiplying into a factor known as spectral shape factor (*SSF*) to obtain the adjusted collapse margin ratio, *ACMR* [Eq. 4.12] (ATC 2009b). Spectral shape factors depends on the ductility of the system, μ_T (a value of 4.0 was obtained from pushover curve in Fig. 4.5, by dividing ultimate drift with effective yield drift) and the applicable seismic design category which was assumed to be D_{max} in this case. The value of SSF is 1.22 which was obtained directly from Appendix J.

$$ACMR = SSF \times CMR \tag{4.12}$$

Therefore *ACMR* = 2.35. This value was compared with an acceptable value of ACMR symbolized as $ACMR_{10\%}$. The $ACMR_{10\%}$ value was obtained by considering total system collapse uncertainty denoted as β_{TOT} (Eq. 4.13), which account for other sources of uncertainties in the performance assessment process. These sources of uncertainties include, design requirements, test data, non-linear models and record to record uncertainty.

$$\beta_{TOT} = \sqrt{\beta_{DR} + \beta_{TD} + \beta_{MDL} + \hat{\beta}} \tag{4.13}$$

Value of β_{TOT} was calculated to be 0.66 after assuming a value for uncertainties corresponding to different parameters, as shown in Table 4.9. Uncertainty parameters were derived from the range specified in FEMA P-695 (ATC 2009b). The adjusted collapse fragility curve was plotted in Fig. 4.11 after considering β_{TOT}. As shown in Fig 4.11, the same collapse median intensity is pivoted at 2.31g but the curve has more dispersion due to increase in the uncertainty. The calculated $ACMR_{10\%}$ value was 2.31. As defined in FEMA P-695 (ATC 2009b), the system is deemed acceptable if *ACMR* is greater than $ACMR_{10\%}$. Based on this criteria, the system passes (2.35 > 2.31) and therefore one can conclude that, the selected RM SFRS which was designed to meet the prescriptive requirements of the ductile masonry walls classification of the CSA S304 (CSA 2014), shows potential capacity against collapse under high intensity earthquakes in one of the highest seismic zones in western Canada.

4.7 CONCLUSIONS

This chapter presented a collapse fragility assessment of a two-storey RMSW building located in the region of Victoria (Gonzales Heights), British Columbia. The seismic performance assessment process presented in the FEMA P-58 document (ATC 2012) was followed. The process involves selection and scaling of ground motions, the development of an analytical model that is used to perform incremental dynamic analysis, and the development of fragility curves to describe the probability of collapse of the structural system at a given seismic intensity measure, *IM.*

The analytical model developed is based on a 1D fiber based macro model simulating the inelastic flexural behaviour of the walls (Ezzeledin et al. 2014). Shear deformations in the walls were aggregated using a uniaxial material model available in the OpenSees platform (Pinching 4 material) to prevent underestimation of top displacement. The calibrated numerical model was compared to the experimental results (hysteresis loops) presented in Chapter 2. The calibrated model captures the inelastic response of RM shear walls with very good accuracy corresponding to walls W5 and W6, which have high aspect ratio.

The intensity-based assessment was the selected procedure for ground motion selection and scaling, following the FEMA P-58 (ATC 2012) procedure. The procedure requires a target response spectrum to match the response spectra to. In this study, the NBCC design spectrum for Victoria, BC, was used. From a total of 135 simulated ground motions (Assatourians and Atkinson 2010), a suite of 30 (15 pairs) was selected. Inelastic demands for a model masonry building were determined using IDA procedure. The study generated a wealth of information about the nonlinear behaviour of the RM-SFRS under different seismic intensities. Collapse fragility assessment of the RM SFRS by different methods (method of moments, maximum likelihood method, and least squares regression method) was then conducted using IDA data for *DM*-based and *IM*-based collapse rules.

The *DM*-based rule shows more robustness in the fragility parameters as compared to the *IM*-based rule for collapse definition criteria. Being on the conservative side the lowest collapse median intensity of approximately 2.31g with highest dispersion value of 0.48 were used to evaluate the performance and base the decision of the seismic vulnerability of the RM SFRS using the adjusted collapse margin ratio. The system were deemed acceptable since the *ACMR* was greater than $ACMR_{10\%}$ (2.35 > 2.31). Therefore one can conclude that, the selected RM SFRS which was designed to meet the prescriptive requirements of the *ductile masonry walls* classification of the CSA S304 (CSA 2014), shows potential capacity against collapse under high intensity earthquakes in one of the highest seismic zones in western Canada and it should be considered as a viable SFRS used in seismic design. The procedure described in the chapter can be adopted to investigate the collapse fragility of other SFRS in different seismic regions through careful selection and scaling of the ground motion records associated with such region's seismicity.

4.8 CHAPTER 4 NOTATION

The following notations are used in this chapter:
a, b = least squares regression parameters;
$ACMR$ = adjusted collapse margin ratio;
$ACMR_{10\%}$ = adjusted collapse margin ratio at 10% probability of collapse using β_{TOT};
C_{DM} = value of damage measure at which collapse occurs;
C_{IM} = value of intensity measure at which collapse occurs;
CMR = collapse margin ratio;
DS1 = slight flexural damage state;
DS2 = moderate flexural damage state;
DS3 = severe flexural damage state;
E = Young's modulus of the wall's material (MPa);
E_m = Young's modulus of masonry (MPa);
E_s = Young's modulus of steel (MPa);
f'_m = compressive strength of masonry prism (MPa);
f_u = ultimate stress of vertical reinforcement (MPa);
f_y = yield stress of vertical reinforcement (MPa);
f_t = tensile stress of masonry(MPa);
g = Initial hardening ratio in the monotonic slip vs. bar stress response;
h = strain hardening ratio;
IDR_{max} = maximum inter-storey drift;
IM = intensity measure;
$P(C|IM=x)$ = Probability of collapse given that the intensity measure is equal to x;
n_i = ground motion i;
n_j = total number of ground motion j;
p_j = probability that ground motion $IM= x_j$ will cause collapse to the structure;
$R, R0, cR1, cR2$ = parameters to control transition from elastic to plastic branch in Steel 02;
r = parameter that controls the non-linear descending branch;
$S_a(T_1, 5\%)$ = spectral acceleration at fundamental period of structure for 5% damping;
$S_{gm}(T)$ = geometric mean spectral acceleration at period T (g);
$S_x(T)$ = x-direction component spectral acceleration (g);
$S_y(T)$ = y-direction component spectral acceleration (g);
SSF = spectral shape factor;
T = period of vibration (s);
T_1 = fundamental period of vibration (s);
z_j = number of collapses at a specific intensity;

xp = Non-dimensional term that defines the strain at which the straight line descent begins in tension;
xr = Non-dimensional term that defines the strain at which the straight line descent begins in compression;
θ = collapse median intensity (g);
$\hat{\theta}$ = estimated collapse median intensity (g);
β = dispersion of seismic demand conditioned on the *IM;*
$\hat{\beta}$ = estimated dispersion of seismic demand conditioned on the *IM*;
β_{DR} = design requirements-related collapse uncertainty;
β_{TD} = test data-related collapse uncertainty;
β_{MDL} = modelling related collapse uncertainty;
β_{TOT} = total system collapse uncertainty;
ε_m = ultimate compressive strain of masonry;
ε_t = ultimate tensile strain of masonry;
μ_T = period-based ductility of index archetype model;
Φ = standard normal cumulative distribution function, CDF;

4.9 Chapter 4 References

Adams, J. and Atkinson, G. (2003). "Development of seismic hazard maps for the 2003 National Building Code of Canada." *Canadian Journal of Civil Engineering*, 30, 255-271.

Adams, J., and Halchuk, S. (2003). "Fourth generation seismic hazard maps of Canada: Values for over 650 Canadian localities intended for the 2005 National Building Code of Canada." *Geological Survey of Canada* Open File 4459 150 pp.

Ahmadi, F.,Hernandez, J.,Sherman, J.,Kapoi, C.,Klingner, R., and McLean, D. (2014). "Seismic Performance of Cantilever-Reinforced Concrete Masonry Shear Walls." *J. Struct. Eng*.,140(9), 04014051.

Applied Technology Council. (ATC). (2007). "Interim Testing Protocols for Determining the Seismic Performance Characteristics of Structural and Non-structural Components." *Federal Emergency Management Agency* (*FEMA) 461*, Washington D.C.

Applied Technology Council (ATC). (2009a). "Background Document: Damage States and Fragility Curves for Reinforced Masonry Shear Walls." Federal Emergency Management Agency (FEMA) 58-1/BD-3.8.10, Washington, DC.

Applied Technology Council (ATC). (2009b). "Quantification of Building Seismic Performance Factors." *Federal Emergency Management Agency (FEMA)* P-695, Washington, DC.

Applied Technology Council.(ATC). (2012). "Seismic Performance Assessment of Buildings: Volume 1- Methodology" *Federal Emergency Management Agency* (*FEMA) P-58-1*, Washington D.C., USA.

Assatourians, K., and G. Atkinson (2010). "Database of processed time series and response spectra for Canada: An example application to study of the 2005 MN5.4 Riviere du Loup," *Quebec earthquake. Seism. Res. L.*, 81, in press.

Azarbakht, A., Mousavi, G., and Ghafory-Ashtiany, M. (2012). “Adjustment of Seismic Collapse Fragility Curves of Structures by Considering the Ground Motion Spectral Shape Effects” *Journal of Earthquake Engineering*, 16(8), 1095-1112.

Bai, J., Hueste, M.B., “Deterministic and Probabilistic Evaluation of Retrofit Alternatives for a Five-Story Flat-Slab RC Building” Texas A&M University, Zachry Dept. of Civil Engineering, Texas, January 2007.

Baker, J., W. (2014). “Efficient analytical fragility fitting using dynamic structural analysis” *EERI Technical Note*.

Banting, B. R. and El-Dakhakhni, W. W. (2012). “Force‐ and Displacement‐ Based Seismic Performance Parameters for Reinforced Masonry Structural Walls with Boundary Elements.” *J. Struct. Eng.*, 10.1061/(ASCE)ST.1943-541X.0000572, 1477-1491.

Bradley, B. A., and Dhakal, R. P. (2008). “Error estimation of closed-form solution for annual rate of structural collapse.” *Earthquake Engineering & Structural Dynamics*, 37(15), 1721–1737.

Calvi, G. M., Pinho, R., Magenes, G., Bommer, J. J., Restrepo-Vélez, L. F., and Crowley, H. (2006). “Development of seismic vulnerability assessment methodologies over the past 30 years.” *ISET journal of Earthquake Technology*, 43(3), 75–104.

Canadian Standards Association (CSA). (2014) “Design of masonry structures.” CSA S304-14, Mississauga, Canada.

Chang, G.A., and Mander, J.B. (1994) “Seismic Energy Based Fatigue Damage Analysis of Bridge Columns:Part 1 – Evaluation of Seismic Capacity.” *NCEER Technical Report No. NCEER-94-0006*, State University of New York, Buffalo, N.

Cornell, A. C., Jalayer, F., Hamburger, R. O., and Foutch, D. A., 2002. Probabilistic basis for 2000 SAC Federal Emergency Management Agency steel moment frame guidelines, *J. Struct. Eng.* 128, 526–532.

Eads, L., Miranda, E., Krawinkler, H., and Lignos, D. G. (2013). “An efficient method for estimating the collapse risk of structures in seismic regions.” *Earthquake Engineering & Structural Dynamics*, 42(1), 25–41.

Ezzeledin, M., Lydell, W., Shedid, M., El-Dakhakhni, W. (2014) “Numerical modelling of reinforced concrete block structural walls under seismic loading”, *9th International Masonry Conference*, Guimarães, Portugal.

FEMA. Recommended seismic design criteria for new steel moment frame buildings. *Report No. FEMA-350*, SAC Joint Venture, Federal Emergency Management Agency, Washington, DC, 2000.

Filippou, F. C., Popov, E. P., Bertero, V. V. (1983). "Effects of Bond Deterioration on Hysteretic Behaviour of Reinforced Concrete Joints". Report EERC 83-19, *Earthquake Engineering Research Center*, University of California, Berkeley.

Ghafory-Ashtiany, M., Mousavi, M., and Azarbakht, A. (2010). “Strong ground motion record selection for the reliable prediction of the mean seismic collapse capacity of a structure group.” *Earthquake Engineering & Structural Dynamics*, n/a–n/a.

Haach, V.,Vasconcelos, G., and Lourenço, P.(2010).“Experimental Analysis of Reinforced Concrete Block Masonry Walls Subjected to In-Plane Cyclic Loading.” *J. Struct. Eng.*,136(4), 452–462.

Hamburger, R.O. (2014). “FEMA P-58 Seismic Performance Assessment of Buildings.” Proc. 10th National Conference in Earthquake Engineering, Earthquake Engineering Research Institute, Anchorage, Alaska, 2014.

Heerema, P., Shedid, M., and El-Dakhakhni, W. (2014). "Seismic Response Analysis of a Reinforced Concrete Block Shear Wall Asymmetric Building." *J. Struct. Eng.* , 10.1061/(ASCE)ST.1943-541X.0001140 , 04014178.

Ibarra, L. F., and Krawinkler, H. (2005). *Global collapse of frame structures under seismic excitations*. John A. Blume Earthquake Engineering Center, Stanford, CA, 324.

Kennedy, R. P., and Ravindra, M. K. (1984). “Seismic Fragilities for Nuclear Power Plant Risk Studies.” *Nuclear engineering and design: an international journal devoted to the thermal, mechanical and structural problems of nuclear energy*, 79, 47–68.

Khalfan M. “Fragility Curves for Residential building in developing countries: A case study on non-engineered unreinforced masonry homes in Bantul, Indonesia” (2013), Master of Applied Science, Open Access Dissertations and Theses, Paper 7691.

Khalfan, M., Tait, M., and El-Dakhakhni, W. (2014). "Seismic Risk Assessment of Non-engineered Residential Buildings: State of the Practice." *Nat. Hazards Rev*., 10.1061/(ASCE)NH.1527-6996.0000164, 04014027.

Kim, S.-H., and Shinozuka, M. (2004). “Development of fragility curves of bridges retrofitted by column jacketing.” *Probabilistic Engineering Mechanics*, 19(1–2), 105–112.

Konstantinidis, D. and Nikfar, F. (2015), “Seismic Response of Sliding Equipment and Contents in Base-Isolated Buildings Subjected to Broadband Ground Motions.” *Earthquake Engineering and Structural Dynamics*, 44(6): 865–887.

Krawinkler H., Zareian F. (2007) “Prediction of Collapse – How realistic and practical is it, and what can we learn from it”, *Struct. Design Tall building*, (16), 633-653.

Li, Y., Song, R., and Van De Lindt, J. (2014). “Collapse Fragility of Steel Structures Subjected to Earthquake Mainshock-Aftershock Sequences.” *J. Struct. Eng.,* 140(12), 04014095.

Lowes, L. L., Mitra, N., and Altoontash A. (2003). “A Beam-Column Joint Model for Simulating the Earthquake Response of Reinforced Concrete Frames.”.” *Pacific Earthquake Engineering Research Report*, PEER 2003/10. Berkeley: University of California.

Masonry Standards Joint Committee of the American Concrete Institute, American Society of Civil Engineers, and The Masonry Society (MSJC). (2013). “Building code requirements for Masonry Structures.” TMS 402-13/ASCE 5-13/ACI 530-13, Detroit, MI, New York, and Boulder, CO.

Massone, L. and Wallace, J. (2004). “Load-Deformation Responses of Slender Reinforced Concrete Walls.” *ACI Struct. J.*, Vol. 101, No. 1, pp. 103-113.

McKenna, F., Fenves, G. L., Scott, M. H., and Jeremic, B., (2000). Open System for Earthquake Engineering Simulation (OpenSees). Pacific Earthquake Engineering Research Center, University of California, Berkeley, CA.

Menegotto, M., and Pinto, P.E. (1973). “Method of analysis of cyclically loaded RC plane frames including changes in geometry and non-elastic behaviour of elements under normal force and bending.” *Preliminary Report IABSE*, vol 13.

Mojiri, S., El-Dakhakhni, W., and Tait, M. (2014). "Seismic Fragility Evaluation of Lightly Reinforced Concrete-Block Shear Walls for Probabilistic Risk Assessment." *J. Struct. Eng*., 10.1061/(ASCE)ST.1943-541X.0001055, 04014116.

National Building Code of Canada (NBCC). (2010). "National Building Code of Canada 2010." *NRCC-10*, Ottawa, Canada.

Nazari, N., van de Lindt, J., and Li, Y. (2015). "Effect of Mainshock-Aftershock Sequences on Wood frame Building Damage Fragilities." *J. Perform. Constr. Facil.*, 29(1), 04014036.

Orakcal, K., Massone, L. M. and Wallace, J. (2006). "Analytical Modelling of Reinforced Concrete Walls for Predicting Flexural and Coupled-Shear-Flexural Responses" *PEER Report, Pacific Engineering Research Centre*, College of Engineering, University of California, Berkeley.

Park J., Towashiraporn P., Craig I. J., Goodno J. B. (2009) "Seismic Fragility Analysis of Low-rise Unreinforced Masonry Structures" *Eng. Struct.* pp 125-137.

Porter, K., Kennedy, R., and Bachman, R. (2007). "Creating Fragility Functions for Performance-Based Earthquake Engineering." *Earthquake Spectra*, 23(2), 471–489.

Purba, R. and Bruneau, M. (2015). "Seismic Performance of Steel Plate Shear Walls Considering Two Different Design Philosophies of Infill Plates. II: Assessment of Collapse Potential." *J. Struct. Eng.*, 141(6), 04014161.

Rota M., Penna A., Magenes G. (2010). " A methodology for deriving analytical fragility curves for masonry building based on stochastic nonlinear analyses" *Eng. Struct*, 1312-1323.

Shafei, B., Zareian, F., and Lignos, D. G. (2011). "A simplified method for collapse capacity assessment of moment-resisting frame and shear wall structural systems." *Engineering Structures*, 33(4), 1107–1116.

Shedid, M. (2009), "Ductility of Concrete Block Shear Wall Structures" Ph.D. Thesis, Department of Civil Engineering, McMaster University, Ontario, Canada.

Shedid, M., El-Dakhakhni, W., and Drysdale, R.(2010a)."Alternative Strategies to Enhance the Seismic Performance of Reinforced Concrete-Block Shear Wall Systems." *J. Struct. Eng.*, 136(6), 676–689.

Shedid, M., El-Dakhakhni, W. and Drysdale, R. (2010b). "Characteristics of Rectangular, Flanged and End- Confined Reinforced Concrete Masonry Shear Walls for Seismic Design." *J. Struct. Eng.* 136 (12), 1471-1482.

Shinozuka M., Feng M.Q., Kim H., Uzawa T., Ueda T., "Statistical Analysis of Fragility Curves", Dept. of Civil Engineering, University of South Carolina, California, Technical Report MCEER, 2001.

Siyam, M., El-Dakhakhni, W., Shedid, M., and Drysdale, R. (2015a). "Seismic Response Evaluation of Ductile Reinforced Concrete Block Structural Walls. I: Experimental Results and Force-Based Design Parameters." *J. Perform. Constr. Facil.*, 10.1061/(ASCE)CF.1943-5509.0000794 , 04015066.

Siyam, M., El-Dakhakhni, W., Banting, B., and Drysdale, R. (2015b). "Seismic Response Evaluation of Ductile Reinforced Concrete Block Structural Walls. II: Displacement and Performance–Based Design Parameters." *J. Perform. Constr. Facil.*, 10.1061/(ASCE)CF.1943-5509.0000804, 04015067.

Vamvatsikos, D., and Cornell, C. A. (2002). "Incremental dynamic analysis." *Earthquake Eng. Struct. Dynam.,* 31(3), 491–514.

Villaverde, R. (2007). "Methods to Assess the Seismic Collapse Capacity of Building Structures: State of the Art." *Journal of Structural Engineering*, 133(1), 57–66.

Waugh, Jonathan D., and Sritharan, Sri (2010) "Lessons Learned from Seismic Analysis of a Seven-Story Concrete Test Building" *Journal of Earthquake Engineering*, 14: 3, pp 448-469.

Table 4.1: Wall Details and Specifications

Wall	Type	Height (mm)	Length (mm)	Aspect ratio	$Mass_{wall}$ / $Mass_{1st\ floor}$	Vertical reinforcement	Horizontal reinforcement		CSA shear wall Classification
						ρ_v (%)	ρ_{h1} (%)	ρ_{h2} (%)	
W1	Rectangular	6400	4590	1.4	0.059	0.6	0.26	0.14	Ductile
W2	Flanged	6400	4590	1.4	0.062	0.6	0.26	0.14	Ductile
W5	Rectangular	6400	1790	3.6	0.023	0.6	0.26	0.14	Ductile
W6	Rectangular	6400	1390	4.6	0.018	0.6	0.26	0.14	Ductile
W6a	Rectangular	6400	1590	4.6	0.021	1.2	0.26	0.14	Ductile

Table 4.2 Mass and Axial Load Assigned to Walls at Each Floor Level

	Mass #	**Area$_{mass}$ (m^2)**	**Area$_{axial}$ (m^2)**	**Weight (kN)**	**Mass (tonnes)**	**Axial load (kN)**	**Nodes in OpenSees**
First floor	m1	19.64	12.63	80.01	8.16	109.38	6
	m2	20.66	18.82	84.14	8.58	145.97	13
	m3	20.66	18.82	84.14	8.58	145.97	20
	m4	19.64	12.63	80.01	8.16	109.38	27
	m5	266.75	53.67	1086.40	110.74	341.27	34
	m6	13.83	0.00	56.35	5.74	45.00	41
Roof level	m7	19.64	12.63	75.79	7.73	82.65	7
	m8	20.66	18.82	79.71	8.13	115.25	14
	m9	20.66	18.82	79.71	8.13	115.25	21
	m10	19.64	12.63	75.79	7.73	82.65	28
	m11	266.75	53.67	1029.19	104.91	294.32	35
	m12	13.83	0.00	53.38	5.44	45.00	42

Table 4.3: Material Properties as Defined in OpenSees (McKenna et al., 2000)

Concrete masonry (Concrete07)	**Values**
f'_m **(MPa)**	13.5
ε_m***(mm/mm)***	0.002
f_t***(MPa)***	0.5
ε_t***(mm/mm)***	0.00011
E_m **(MPa)**	11475
xp	2
xn	2.3
r	2.3
E_{slab} **(MPa)**	200000
Vertical reinforcement (Steel02)	
f_y***(MPa)***	500
E_s	200000
h	0.0025
R0	10
cR1	0.925
cR2	0.15
Bond Steel (Bond_SP01)	
f_u **(MPa)**	600
S_y	0.35
S_u	13.2
g	0.4
R	0.6

Table 4.4 Experimental and Numerical Model Comparison (Cyclic Analysis)

Cycle	**1**	**2**	**3**	**4**	**5**	**6**
Wall W1						
Displacement (mm) (Input)						
Experimental	6.4	12.8	19.4	25.6	32	38.5
Numerical	6.4	12.8	19.4	25.6	32	38.5
Lateral load (kN) (Output)						
Experimental	68.4	90.7	89.8	85.7	78.1	53.1
Numerical	78.8	95.5	85.5	79.9	77.0	75.0
Exp./Numerical	0.9	0.9	1.1	1.1	1.0	0.7
Wall W5						
Displacement (mm) (Input)						
Experimental	9.5	18.9	28.3	37.6	47.1	56.4
Numerical	9.5	18.9	28.3	37.6	47.1	56.4
Lateral load (kN) (Output)						
Experimental	9.9	15.6	14	13.95	13.7	12
Numerical	10.8	14.4	13.2	11.32	10.8	11.2
Exp./Numerical	0.9	1.1	1.1	1.2	1.3	1.1
Wall W6						
Displacement (mm) (Input)						
Experimental	14.9	29.5	44.3	59.2	73.8	-

Numerical	14.9	29.5	44.3	59.2	73.8	-
Lateral load (kN) (Output)						
Experimental	6.8	9.9	8.4	7.56	7.21	-
Numerical	7.7	9.34	7.97	7.65	7.65	-
Exp./Numerical	0.9	1.1	1.1	1.0	0.9	-

Table 4.5: Wall Capacities using CSA S304-14 Code Provisions and Full Scale Numerical Model

Wall	Length	Thickness	Area	Lateral load capacity CSA S304-14		Lateral load capacity Numerical Model	
				Yield (kN)	Ultimate (kN)	Yield (kN)	Ultimate (kN)
W1	4590	190	872100	772	966	798.1	967.1
W5	1790	190	340100	118	148	119.3	144.5
W6	1390	190	264100	77	93	76.7	92.2

Table 4.6 Ground Motion Records Used in IDA

Record #	**Record Designation**	**Earthquake # as per Assatourians & Atkinson (2010)**	**Spectral ordinates**	**Magnitude**	**Soil Class**	**Fault Distance (km)**	**$S_{gm}(T_1)$ (g)**	**Scale factor**
1	west6c1	22	x	6.5	C	11.2	0.73	0.89
2	west6c1	23	y	6.5	C	11.2	0.73	0.89
3	west6c1	25	x	6.5	C	11.2	0.67	0.98
4	west6c1	26	y	6.5	C	11.2	0.67	0.98
5	west6c1	37	x	6.5	C	13.0	0.53	1.22
6	west6c1	38	y	6.5	C	13.0	0.53	1.22
7	west6c1	43	x	6.5	C	13.0	0.52	1.25
8	west6c1	44	y	6.5	C	13.0	0.52	1.25
9	west6c2	1	x	6.5	C	19.7	0.52	1.24
10	west6c2	2	y	6.5	C	19.7	0.52	1.24
11	west6c2	10	x	6.5	C	21.6	0.34	1.90
12	west6c2	11	y	6.5	C	21.6	0.34	1.90
13	west6c2	13	x	6.5	C	21.6	0.39	1.66
14	west6c2	14	y	6.5	C	21.6	0.39	1.66
15	west6c2	19	x	6.5	C	14.6	0.62	1.05
16	west6c2	20	y	6.5	C	14.6	0.62	1.05
17	west6c2	22	x	6.5	C	25.8	0.47	1.39
18	west6c2	23	y	6.5	C	25.8	0.47	1.39
19	west6c2	25	x	6.5	C	26.3	0.49	1.32
20	west6c2	26	y	6.5	C	26.3	0.49	1.32
21	west6c2	31	x	6.5	C	30.0	0.38	1.73
22	west6c2	32	y	6.5	C	30.0	0.38	1.73
23	west6c2	34	x	6.5	C	31.1	0.29	2.25
24	west6c2	35	y	6.5	C	31.1	0.29	2.25
25	west7c2	1	x	7.5	C	47.4	0.45	1.43
26	west7c2	2	y	7.5	C	47.4	0.45	1.43
27	west7c2	7	x	7.5	C	48.8	0.43	1.52
28	west7c2	8	y	7.5	C	48.8	0.43	1.52
29	west7c2	10	x	7.5	C	50.7	0.29	2.25
30	west7c2	11	y	7.5	C	50.7	0.29	2.25

Table 4.7 Damage State Description for Reinforced Masonry Walls (ATC 2012)

Damage State	**Description**	**Repair Measure Fully grouted**
DS1 Slight damage flexure	1. few flexural and shear cracks with hardly noticeable residual crack widths. 2. Slight yielding of extreme vertical reinforcement. 3. No spalling 4. No fracture or buckling of vertical reinforcement. 5. No structural significant damage.	1. Cosmetic repair. 2. Patch cracks and paint each side.
DS2 Moderate damage flexure	1. Numerous flexural and diagonal cracks. 2. Mild toe crushing with vertical cracks or light spalling at wall toes. 3. No fracture or buckling of reinforcement. 4. Small residual deformation.	1. Epoxy injection to repair cracks. 2. Remove loose masonry. 3. Patch spalls with non-shrink grout. 4. Paint each side.
DS3 Severe damage flexure	1.Severe flexural cracks. 2. Severe toe crushing and spalling. 3. Fracture or buckling of vertical reinforcement. 4. Significant residual deformation.	1. Shore. 2. Demolish existing wall. 3. Construct new wall.

Table 4.8 FEMA 58-1 Damage State Identification Criteria from Load-Displacement Curves (ATC 2012)

Damage State	**Identification Criteria**
DS1 Slight Flexural Damage	When a flexural-critical wall has been loaded to 80% of its peak in plane lateral resistance
DS2 Moderate Flexural Damage	When a flexural-critical wall has been loaded to its peak in plane lateral resistance
DS3 Severe Flexural Damage	When a flexural-critical wall has been loaded beyond its peak resistance and exhibited a load drop of 20% with respect to its peak

Table 4.9 Uncertainty Dispersion Values from Different Sources

Uncertainty parameter	**Value**
β_{DR}	0.3
β_{TD}	0.3
β_{MDL}	0.3
β_{RTR}	0.4
β_{TOT}	**0.66**

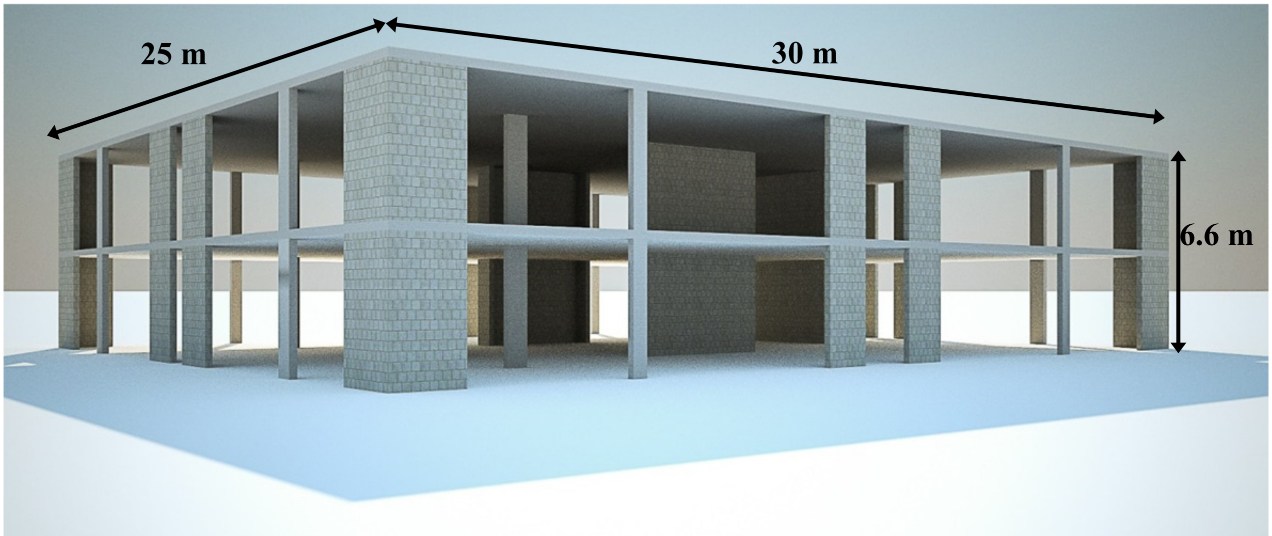

(a)

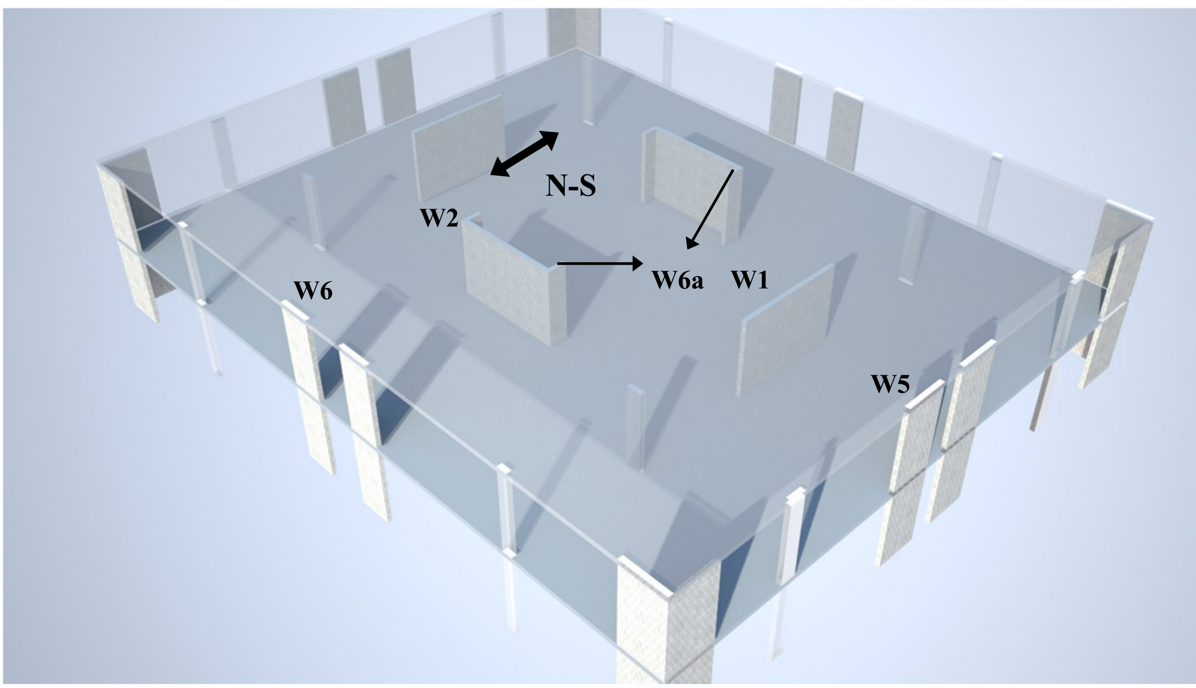

(b)

Fig. 4.1. (a) Archetype full-scale masonry; (b) 3D Top view

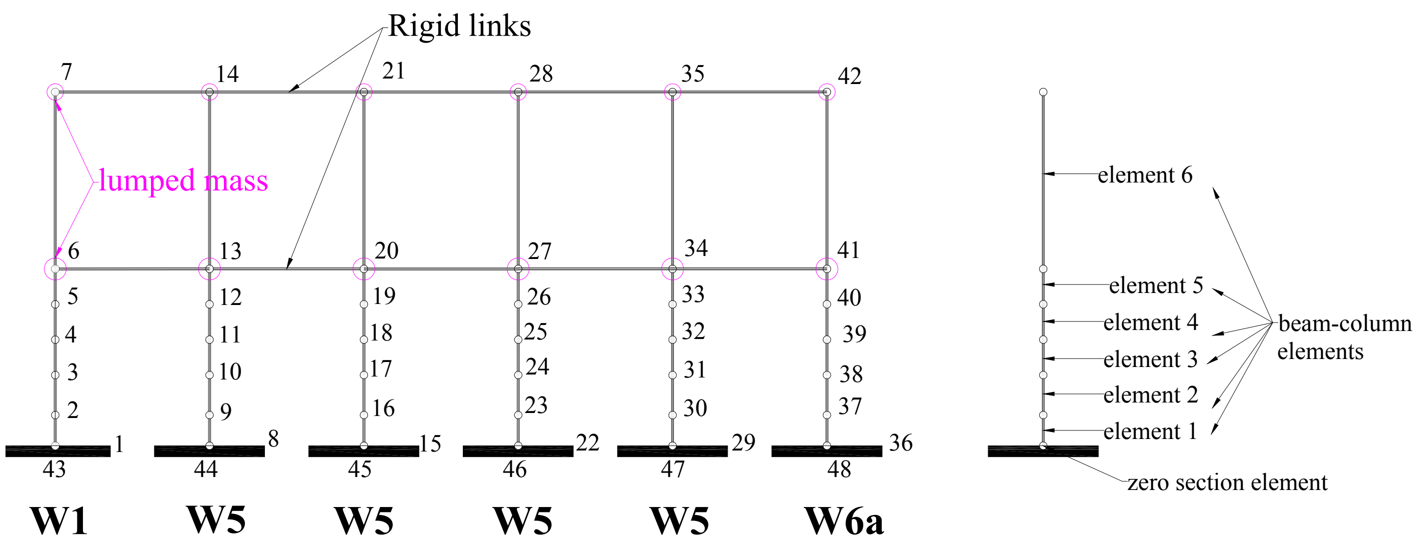

Fig. 4.2. Model discretization in OpenSees: (a) N-S SFRS model; (b) Wall model

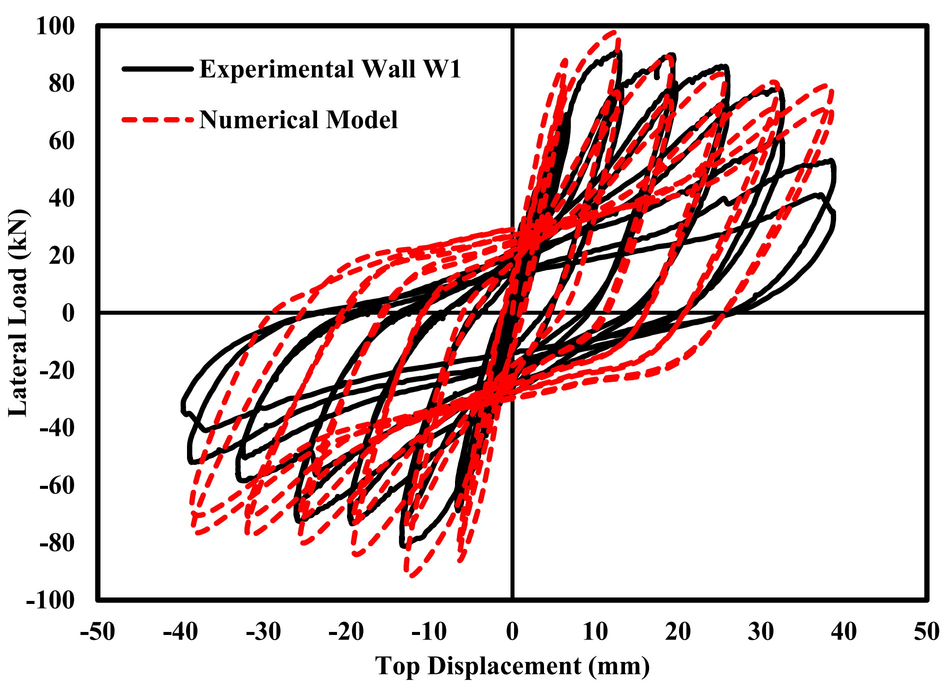

(a)

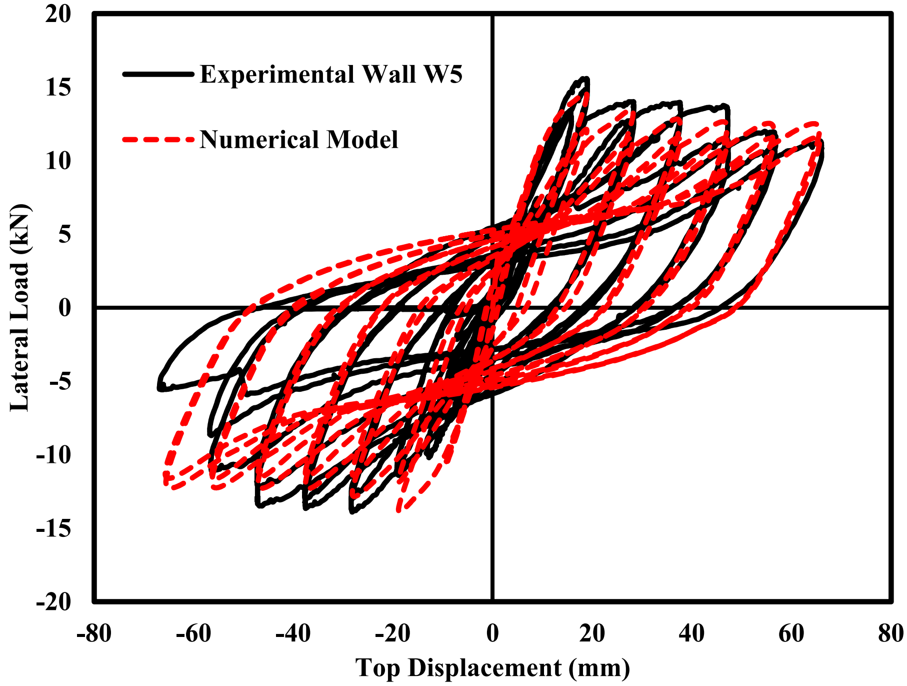

(b)

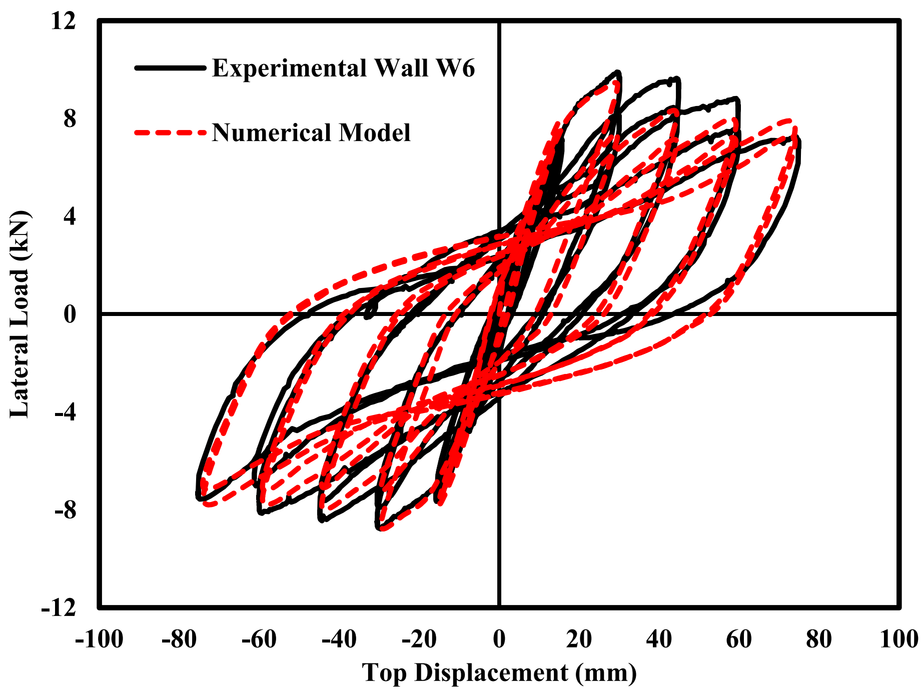

(c)

Fig. 4.3. Numerical model validation of force-displacement relationships: (a) W1; (b) W5; (c) W6

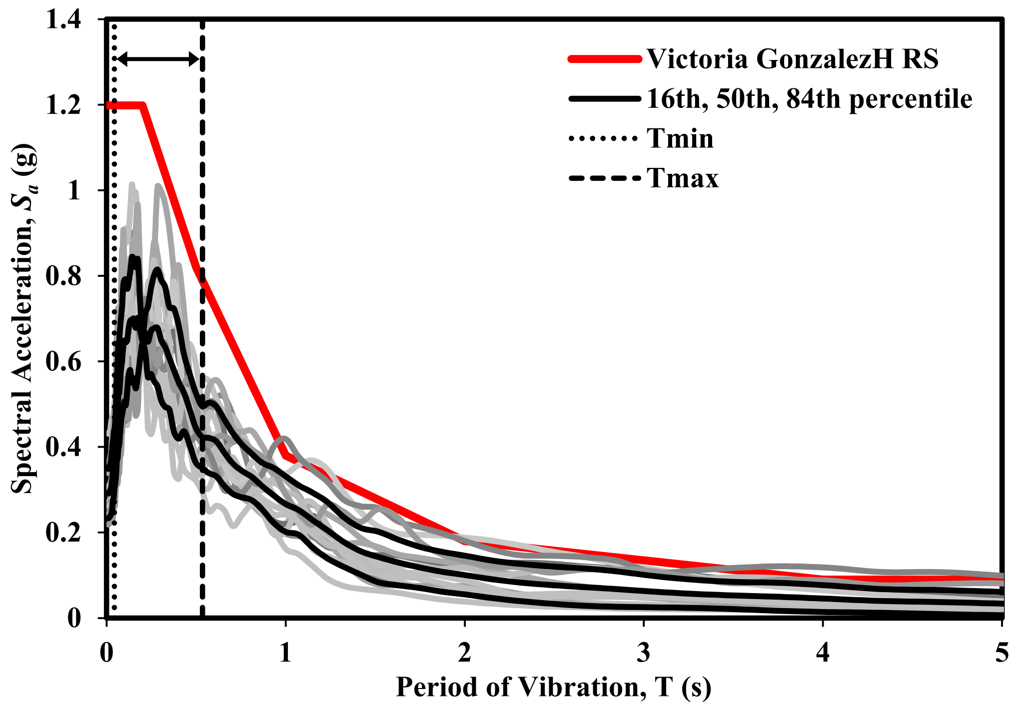

Fig. 4.4. Scaled response spectra pairs from simulated western earthquakes (Assatourians and Atkinson 2010)

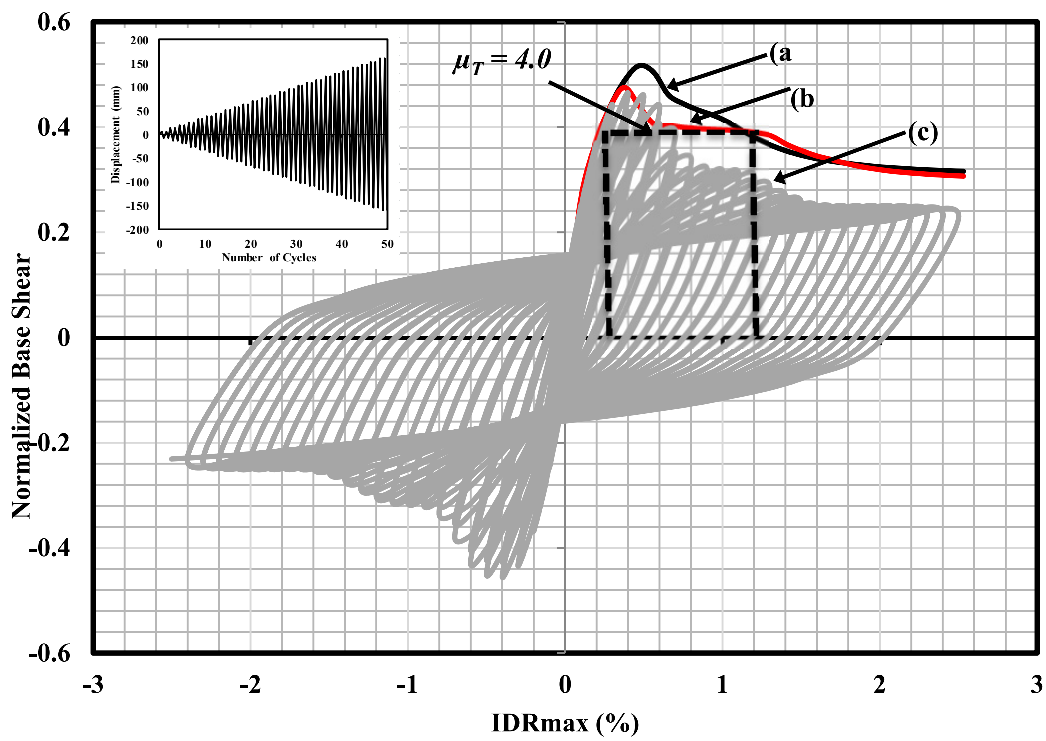

Fig. 4.5. Force-Displacement relationships (a) Pushover curve of system; (b) Pushover curve of individual walls superimposed; (c) Cyclic hysteresis loops

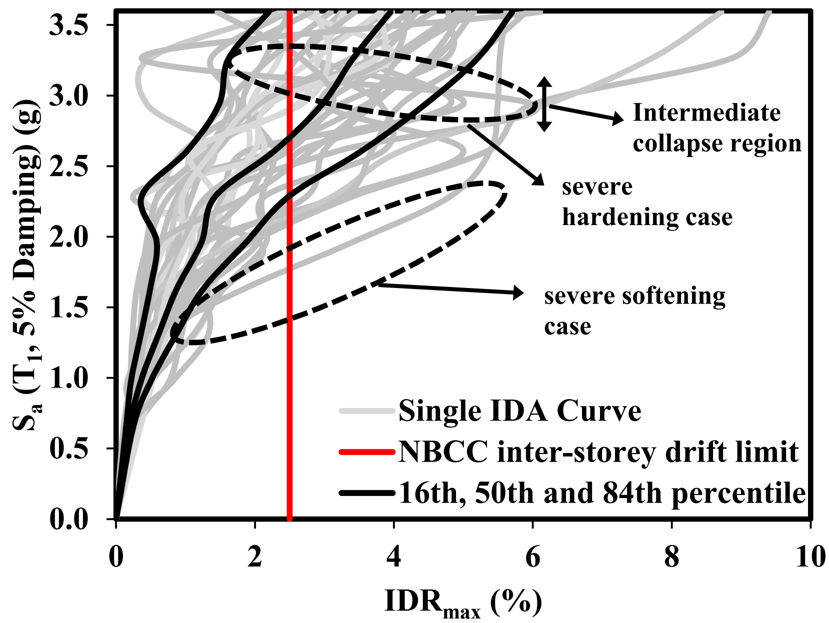

Fig. 4.6. Incremental dynamic analysis (IDA) curves for N-S SFRS

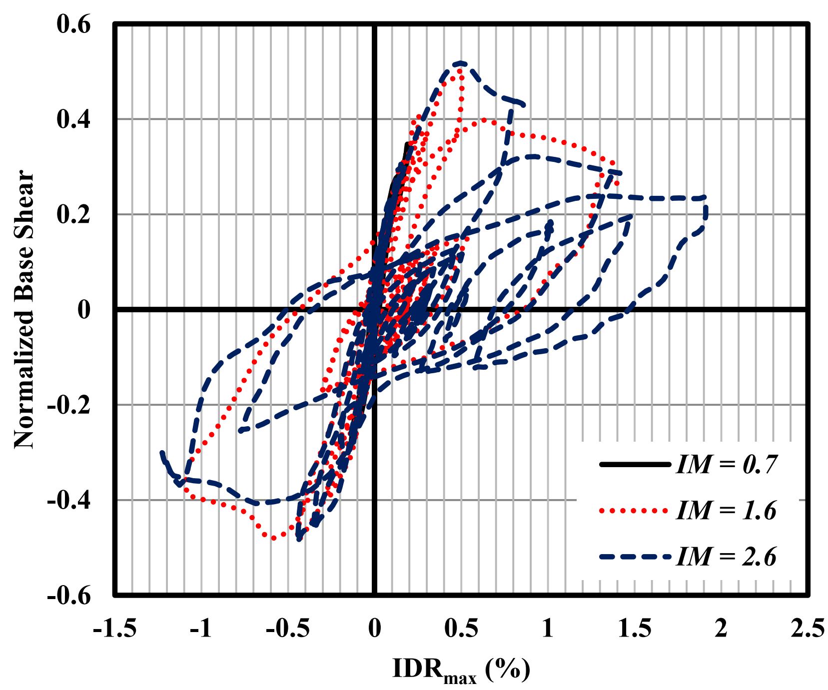

(a)

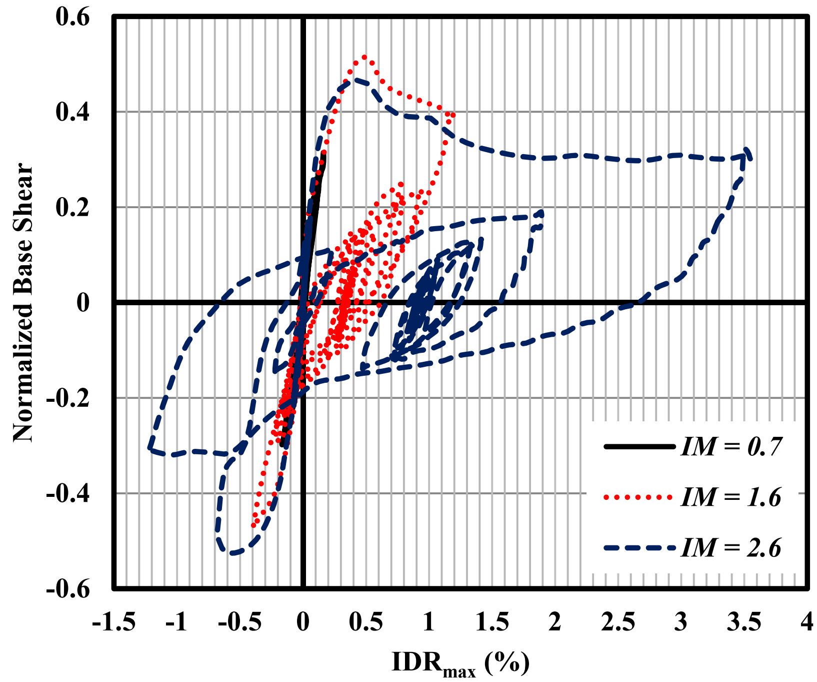

(b)

Fig. 4.7. N-S RM SWS load-displacement relationships for sample ground motions: (a) Record 1; (b) Record 6

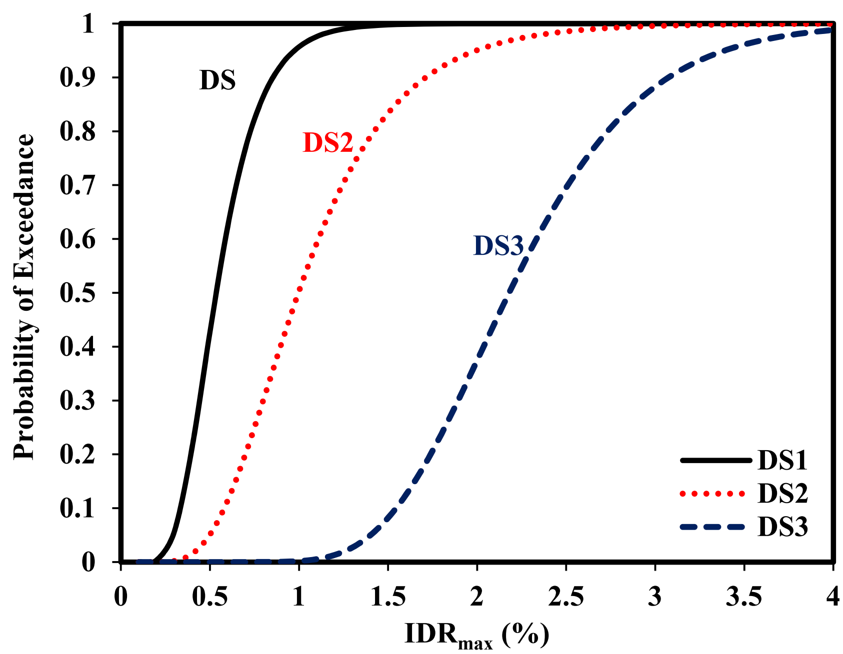

Fig. 4.8. Actual data fragility curves

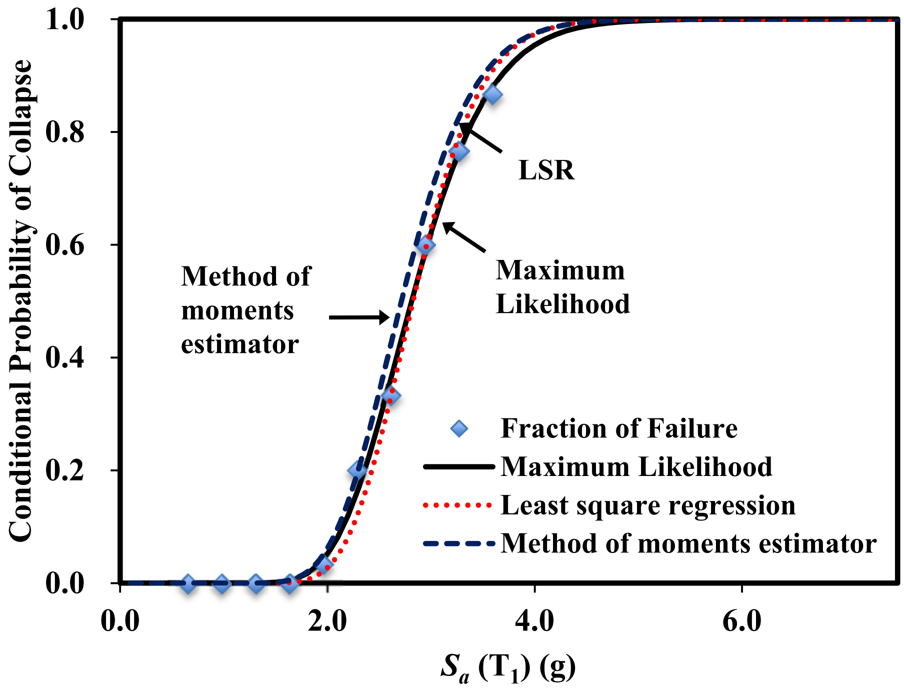

(a)

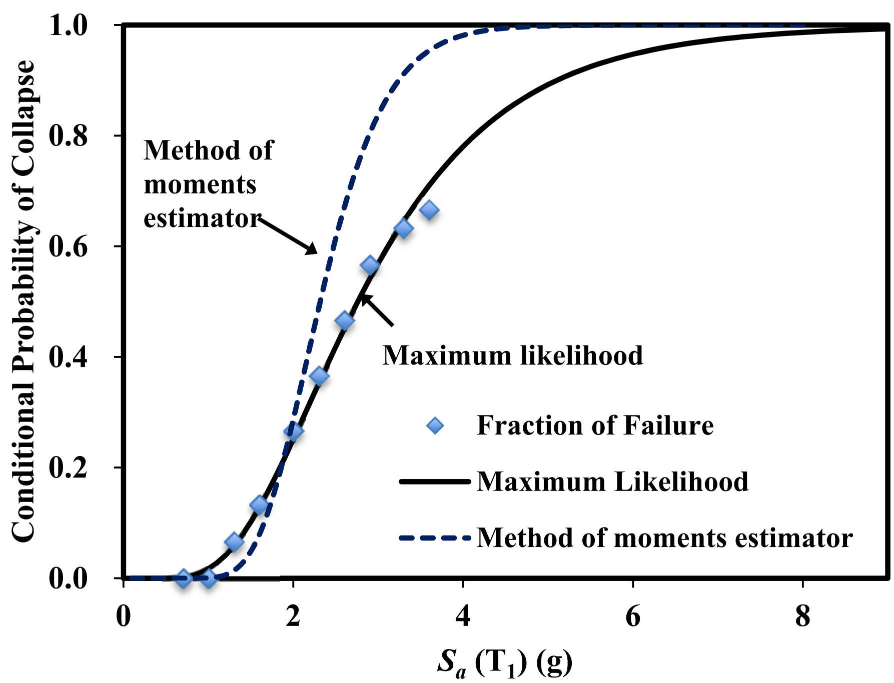

(b)

Fig. 4.9. Collapse fragility curves for N-S RM SFRS using different fragility fitting methods: (a) *DM* based rule; (b) *IM* based rule

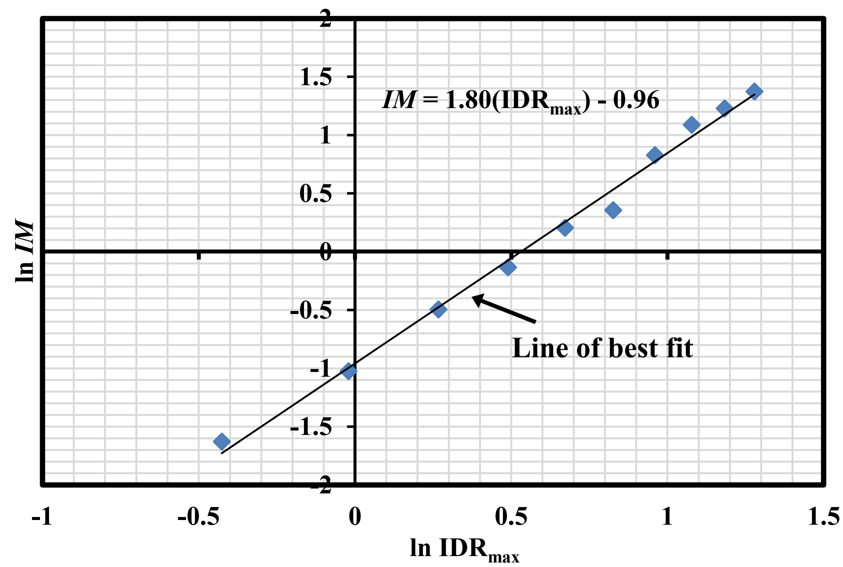

Fig. 4.10. Log-log relationship between seismic demand, IDR_{max} and *IM*

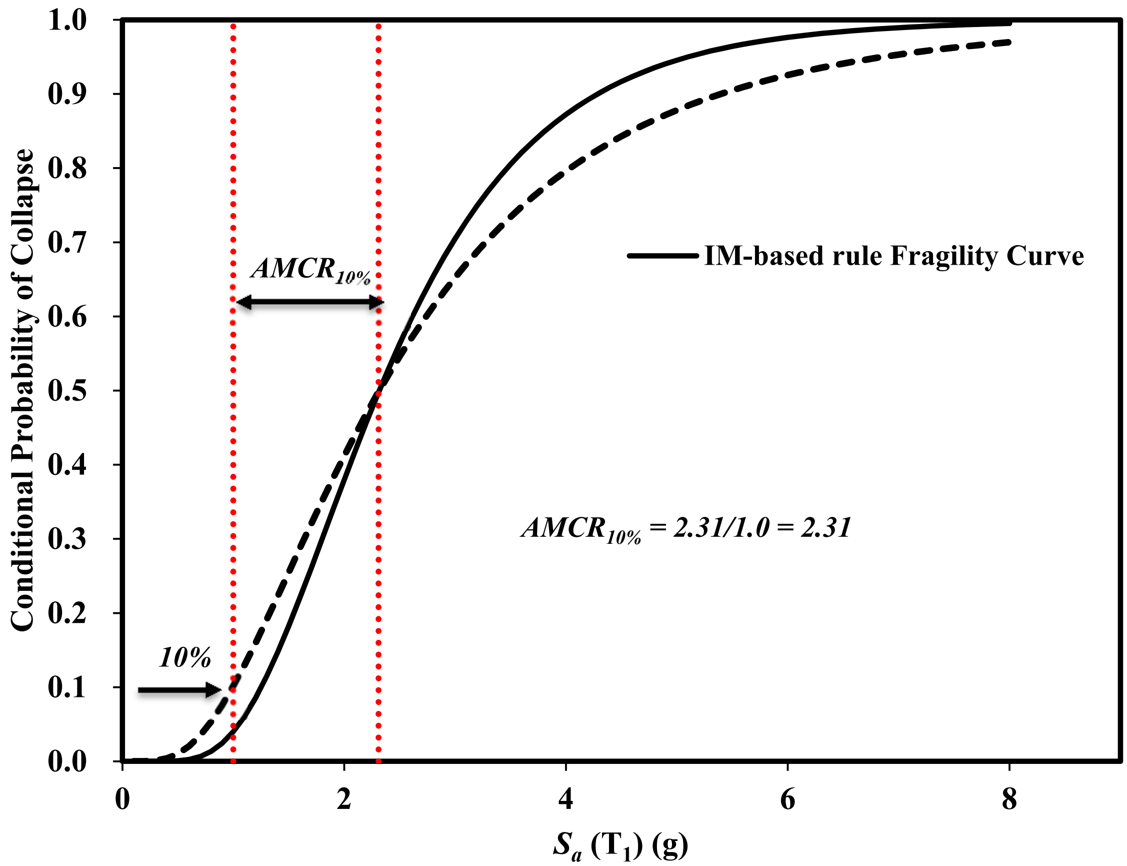

Fig. 4.11. Adjusted collapse fragility curve

CHAPTER 5: CONCLUSIONS AND RECOMMENDATIONS

5.1 CONCLUSIONS

In an effort to understand the seismic performance of RM buildings designed as the main seismic force resisting system (SFRS) comprising of walls detailed to a specific shear wall classification group, a research program was established at McMaster University to meet this objective. Realizing the complex seismic behaviour of RM, the research study was split into three phases to reach the final goal. The first phase focused on evaluating the seismic performance of shear wall components with cross-sectional configurations that exist in RM buildings design. The second phase investigated the seismic performance of a shear wall building with no wall-slab coupling and finally in the third phase, the seismic performance of a shear wall building with wall-slab coupling was examined. This sheds some light on understanding system performance of RM SFRS and its relation to component level seismic behaviour.

The scope of this dissertation covered the first phase of the research study's objective. This was done by conducting an experimental study on ductile shear walls/special reinforced masonry walls SFRS shear wall classification as per CSA S304-14 (CSA 2014-a) and MSJC (2013) standards, respectively. In general, all walls showed a ductile behaviour and failed in flexure. However due to the variation in their cross section configurations, crack patterns were different, with the rectangular and flanged walls showing a combination of flexure and shear cracks. The slab-coupled walls failed by forming plastic hinges at the bottom of the two walls in addition to hinges at the wall/slab interface of the walls. The slender rectangular walls exhibited a dominating flexural failure characterized by bed and head joint cracking, toe crushing and bar fracture at the end of the test. The following sections discuss main conclusions as they pertain to force-based and displacement-based design philosophies. Both design methodologies assisted in formulating a numerical model that was used to assess the seismic vulnerability of a ductile shear wall RM SFRS through what is known as collapse fragility assessment.

5.1.1 Force-based Seismic Design Parameters

The main objective of Chapter 2 was to evaluate key force based seismic design (FBSD) parameters of flexural dominant individual and slab-coupled RM shear walls. Quantifying such FBSD parameters would facilitate assessing whether walls with different cross-sectional configurations, but with the same overall aspect ratio and detailed following the same prescriptive SFRS classification requirements, would develop similar response under seismic events in the context of a code-defined FB methodology. Based on the FBSD parameter quantification of the test walls, the following conclusions can be made:

Displacement ductility capacities corresponding to different wall response levels varied when considering different wall configurations. Using elasto-plastic idealization, on average the idealized displacement ductility capacities, $\mu_{\Delta 0.8Vu}{}^{ep}$ are higher than the theoretical, $\mu_{\Delta}{}^{th}$ by at least 200% for most of the walls. The values ranged from 3.4 to 5.4, indicating the variability in the ductility capacity within the walls. Moreover, utilizing the idealized load-displacement relationships, walls with the same overall aspect ratio showed different idealized equivalent plastic hinge lengths ranging between 0.05 to 0.32 of the wall's length. The slender rectangular walls had a $l_{p,ideal}$ value ranging between 0.26 l_w and 0.36 l_w.

The prediction results of the three different approaches presented in Chapter 2 overestimated the idealized plastic hinge length for the rectangular and flanged walls. The high μ_ϕ values for such walls result in lower values for the idealized plastic hinge lengths. Overall, the results show that Priestley's et al. (2007) prediction is the best estimate for the plastic hinge length where the percentage difference lies between 1 to 40%. It can be inferred that the strain hardening parameter which is only provided in Priestley's expression can be strongly correlated to the plastic hinge length. Axial compression effect which is only included in Bohl and Adebar (2011) expression does not seem to have a major effect on l_p.

The experimental results presented in this study showed that RM walls designed within the same SFRS shear wall classification level could show significant difference in their load-displacement relationship characteristics and displacement ductility capacities. The seismic design process has to incorporate the difference in configuration even for walls within the same SFRS classification level to accurately predict the behaviour of walls designed and detailed for such level. Moreover, North American masonry code seismic design subcommittees might find it beneficial to consider incorporating RM slab-coupled walls, as a separate SFRS classification (similar to their corresponding RC wall counterparts), as they showed better performance than similar walls with the same overall aspect ratio. Further research is encouraged to explore this area.

5.1.2 Displacement-based and Performance –based Seismic Design Parameters

Chapter 3 of the dissertation focused on evaluating the displacement and performance-based seismic parameters for walls designed to the same SFRS classification and having the same overall aspect ratio to assess if such walls can be assigned the same DBSD and PBSD parameters. Moreover, the chapter presented preliminary analysis that may be used towards the adoption of slab-coupled masonry shear wall structures. The DBSD parameters studied here included wall curvatures, wall displacements at yield and at the post-yield stages, stiffness degradation, period elongation and equivalent viscous damping. PBSD parameters included damage states identification and linkage to drift level, extent of plasticity and crack patterns at the corresponding damage states. The values obtained for each parameter showed different ductile capabilities for the different walls configurations of RM shear walls. After thorough analysis of such values the following conclusions can be made:

1. Experimental curvature ductility values for 100 mm wall segments ranged between 8.2 to 30.2. The experimental values for curvature ductility were at least double the theoretical values for most of the walls.

2. Moment curvature idealization is a good method for predicting ultimate displacements for slender walls but not for the stiffer walls. The rationale lies in the fact that the idealization in Priestley's method might not account for coupled shear displacements that arise in stiffer walls. Using the effective stiffness and stiffness at ultimate load can accurately predict the yield displacement for slender walls and ultimate displacement for the stiffer walls respectively. Moreover, accurate estimation of yield and ultimate displacements depend on accurate estimation of the wall lateral stiffness and the slenderness of the wall.

3. The stiffness degradations curves show a similar decreasing trend for all the walls but with variations in the amount of degradation with respect to the wall configuration and aspect ratio.

4. The period elongation for walls with the same SFRS classification level while having different configurations and aspect ratios is slightly different. The slab-coupled walls shows almost nine times lengthening from the initial period, $T_{initial}$ at 3.4% top drift signifying more cracking due to formation of plastic hinges at wall-slab interfaces.

5. The walls on average attain 17% damping ratio at $3\Delta_y$. Equivalent viscous damping plots illustrate the variability that exists between damping ratios at different displacement cycles for

walls having equal overall aspect ratio and different configurations designed to the same SFRS classification.

6. The change in configuration even for walls of equal overall aspect ratio within the same SFRS classification, slightly affected L_p while keeping wall reinforcement ratios the same.

Walls having the same overall aspect ratio and reinforcement ratios will possess different displacement- and performance-based seismic design (DBSD and PBSD) parameters therefore may have different ultimate drift capacities. Slab coupled walls show better performance in terms of the ultimate drift capacities reached, period elongation and equivalent viscous damping when compared to rectangular and flanged walls.

5.1.3 Collapse Fragility Assessment of RM SFRS

Using results from Chapters 2 and 3, the vulnerability of RM SFRS was examined in Chapter 4 by conducting collapse fragility assessment of a two-storey RMSW building located in the region of Victoria (Gonzales Heights), British Columbia. The seismic performance assessment process presented in the FEMA P-58 document (ATC 2012) was followed. The process involves selection and scaling of ground motions, the development of an analytical model that is used to perform incremental dynamic analysis, IDA, and the development of fragility curves to describe the probability of collapse of the structural system at a given seismic intensity measure, *IM*.

The analytical model developed in the study is based on a 1D fiber macro model simulating the inelastic flexural behaviour of the walls (Ezzeledin et al. 2014). Shear deformations in the walls were aggregated using a uniaxial material model available in the OpenSees platform (Pinching 4 material) to prevent underestimation of top displacement. The calibrated numerical model was compared to the experimental results (hysteresis loops) presented in Chapter 2. The calibrated model captured the inelastic response of RM shear walls with very good accuracy (on average ≤ 11%) corresponding to walls W5 and W6, which have high aspect ratio.

The intensity-based assessment was the selected procedure for ground motion selection and scaling, following the FEMA P-58 (ATC 2012) procedure. The procedure requires selection of a target response spectrum (i.e. design spectrum) and then matching several response spectra to the target one. In this study, the NBCC design spectrum for Victoria, BC, was used. From a total of 135 simulated ground motions (Assatourians and Atkinson 2010), a suite of 30 ground motions (15 pairs) was selected. Inelastic demands for a model masonry building were determined using the IDA procedure. The study generated a wealth of information about the nonlinear behaviour of the RM SFRS under different seismic intensities. Collapse fragility assessment of the RM SFRS was then conducted using IDA for the damage measure, *DM*-based and the intensity measure, *IM*-based collapse rules. There were various methods used to fit the collapse fragility curves which were the method of moments, maximum likelihood, and least squares regression.

The *DM*-based rule shows more robustness in the fragility parameters as compared to the *IM*-based rule for collapse definition criteria. Being on the conservative side, the lowest collapse median intensity of approximately 2.31g with highest dispersion value of 0.48 in this case, should be used to base the decision of the seismic vulnerability of the RM SFRS. The system were deemed acceptable since the *ACMR* was greater than $ACMR_{10\%}$ (2.35 > 2.31). Therefore one can conclude that, the selected RM SFRS which were designed to meet the prescriptive requirements of the *ductile masonry walls* classification of the CSA S304 (CSA 2014), shows potential capacity against collapse under high intensity earthquakes in one of the highest seismic zones in western Canada. Therefore such systems should be considered as a viable SFRS in seismic design of structures. The procedure described in the chapter can be adopted to investigate the collapse fragility of other SFRS in different seismic regions through careful selection and scaling of the ground motion records associated with such region's seismicity.

Overall, the dissertation presented a thorough analysis of a specific class of SFRS shear walls (i.e. ductile/special reinforced walls) using traditional and new methodologies highlighting the difference in ductility capacities that exist between walls detailed to be in the same SFRS classification group but having different cross-sectional configurations. The current code provisions do not recognize that difference in shear wall configurations will have a significant effect on the seismic performance of the walls and there is a need to differentiate between walls within the same SFRS classification group. This might change the way the current design code provisions are prescribed. Therefore, the need for collaborating component/system level performance to understand how RM SFRS behave or to quantify key seismic parameters to such systems will be prevalent.

Added to this, the study went further in showing the seismic enhancement that can be gained by considering the wall coupling which develops through the slabs, in the analysis/design of RM slab-coupled shear walls. Such coupling effect are not recognized in the CSA S304-14 while the MSJC only consider RM walls that are coupled by masonry beams which is not within the scope of this dissertation. As for the rectangular and flanged walls, the experimental results agree with the conclusions reached by other researchers in the field. Moreover the seismic risk assessment study goes further in validating statistically the excellent performance of RM SFRS designed according to CSA S304-14 code provisions, making it a viable SFRS in high seismic regions in Canada.

5.2 RECOMMENDATIONS FOR FUTURE RESEARCH

In the light of the experimental test data, analysis results, numerical model and IDA results, the following steps toward better seismic performance assessment of RM shear walls and systems are proposed:

1. RM slab-coupled walls showed better seismic performance in terms of force-, displacement- and performance-based design parameters. It is recommended that slab-coupled walls with different coupling distances and different slab reinforcement ratios should be investigated. Furthermore different testing schemes (i.e. shake table testing) can be used to further establish the dynamic seismic performance of such walls and compare it to the results of this study. Such experiments will help in creating a database for slab-coupled RM shear walls which will further assist in the adoption of this wall type as a separate SFRS classification (similar to their corresponding RC wall counterparts) in the most current masonry design provisions.
2. The results of the research can be further used in the calibration of numerical models for masonry shear walls with different configurations i.e. flanged and slab coupled.
3. Phases 2 and 3 of the research objective will be used to compare component –level performance with system's level performance. Such comparison will assist in better quantifying the accuracy of using scaled-model (as compared to full scale prototypes) in the experimental testing of masonry components and systems.
4. Creating simplified SFRS 1D stick models by incorporating the effect of wall/slab coupling in the slab-coupled walls and comparing it with results of the created model (i.e. within this dissertation) to analyze the effect of coupling in the dynamic response of masonry SFRS. Moreover, a more complicated 3D model of the same prototype masonry building used in

Chapter 4 can be created to analyze the validity of using such models as compared to simplified 1D model.

5. Using collapse fragility curves along with the adjusted collapse margin ratio (*ACMR*) quantification, as part of seismic risk assessment, SRA is an excellent way to evaluate the seismic vulnerability of RM SFRS. It is also a crucial step towards creating loss functions which is the ultimate goal in the seismic performance and risk assessment process outlined in FEMA P-58 (ACT 2012) document.

5.3 CHAPTER 5 REFERENCES

Applied Technology Council.(ATC). (2012). “Seismic Performance Assessment of Buildings: Volume 1- Methodology” *Federal Emergency Management Agency* (*FEMA) P-58-1*, Washington D.C., USA.

Assatourians, K., and G. Atkinson (2010). “Database of processed time series and response spectra for Canada: An example application to study of the 2005 MN5.4 Riviere du Loup,” *Quebec earthquake. Seism. Res. L.*, 81, in press.

Canadian Standards Association (CSA). (2014) “Design of masonry structures.” CSA S304-14, Mississauga, Canada.

Ezzeledin, M., Lydell, W., Shedid, M., El-Dakhakhni, W. (2014) “Numerical modelling of reinforced concrete block structural walls under seismic loading”, *9th International Masonry Conference*, Guimarães, Portugal.

Masonry Standards Joint Committee of the American Concrete Institute, American Society of Civil Engineers, and The Masonry Society (MSJC). (2013). “Building code requirements for Masonry Structures.” TMS 402-13/ASCE 5-13/ACI 530-13, Detroit, MI, New York, and Boulder, CO.

McKenna, F., Fenves, G. L., Scott, M. H., and Jeremic, B., (2000). Open System for Earthquake Engineering Simulation (OpenSees). Pacific Earthquake Engineering Research Center, University of California, Berkeley, CA.

National Building Code of Canada (NBCC). (2010). “National Building Code of Canada 2010.” *NRCC-10*, Ottawa, Canada.

Priestley, M.J.N., and Kowalsky, M.J. (1998). “Aspects of drift and ductility capacity of rectangular structural walls.” *Bulletin of the New Zealand Society for Earthquake Engineering*, 31: 73–85.

Priestley, N., Calvi, G., and Kowalsky, M. (2007). *Displacement-based seismic design of structures*, IUSS Press, Pavia, Italy.

Paulay T., and Priestly, M. (1992). *Seismic design of reinforced concrete and masonry buildings*, Wiley, New York.

APPENDIX A: MATERIAL CHARACTERISTICS

Table A-1 Material Constituents Strength Values

Property	Standard	Average Value (MPa)
Block Strength	ASTM C140-08 (ASTM 2008)	25.6
Masonry Unit compressive Strength (f'_m)	CSA S304-14 (CSA 2014)	19.3
Grout Cylinder Strength	ASTM C1019-05 (ASTM 2005b)	18.5
Mortar cube strength	CSA A179-14 (CSA 2014-c)	19.0
Young's Modulus of Masonry (E_m)	ASTM E111-04 (ASTM 2004)	10305.2
Shear Reinforcement Yield strength	CSA A165 (CSA 2014-b)	670.0

MORTAR SPECIMENS

Table A-2 Mortar Specimens

Specimen	Failure load (N)	f'_{mo} (MPa)	SD	C.O.V (%)
1	37600	14.5		
2	44600	17.1		
3	40300	15.5		
Average	40833	15.7	1.4	8.6
4	37800	14.5		
5	42300	16.3		
6	42500	16.3		
Average	40867	15.7	1.0	6.5
7	48700	18.7		
8	47200	18.1		
9	50300	19.3		
Average	48733	18.7	0.6	3.2
10	37900	14.6		
11	41200	15.8		

12	41800	16.1		
Average	40300	15.5	0.8	5.2
13	44100	17.0		
14	44300	17.0		
15	42600	16.4		
Average	43667	16.8	0.4	2.1
16	58000	22.3		
17	63400	24.4		
18	59300	22.8		
Average	60233	23.2	1.1	4.7
19	60600	23.3		
20	60200	23.1		
21	59900	23.0		
Average	60233	23.2	0.1	0.6
22	60300	23.2		
23	58900	22.6		
24	64900	25.0		
Average	61367	23.6	1.2	5.1
25	72700	28.0		
26	62400	24.0		
27	68900	26.5		
Average	68000	26.1	2.0	7.7
28	41800	16.1		
29	42300	16.3		
30	40500	15.6		
Average	41533	16.0	0.4	2.2
31	43100	16.6		
32	42600	16.4		
33	50500	19.4		
Average	45400	17.5	1.7	9.7
34	34900	13.4		
35	36600	14.1		
36	38400	14.8		

Average	36633	14.1	0.7	4.8
37	41700	16.0		
38	26000	10.0		
39	40400	15.5		
Average	36033	13.9	3.4	24.2
40	54200	20.8		
41	55500	21.3		
42	59600	22.9		
Average	56433	21.7	1.1	5.0

GROUT SPECIMENS

Table A-3 Grout Specimens

Specimen	Failure load (N)	Diameter (mm)	Area (mm^2)	f_g (MPa)	SD	C.O.V (%)
1	189040.0	102.5	8251.6	22.9		
2	182368.0	101.5	8091.4	22.5		
3	184564.0	102.0	8171.3	22.6		
Average	185324.0			22.7	0.20	0.89
4	155680.0	102.0	8171.3	19.1		
5	144560.0	101.5	8091.4	17.9		
6	147880.0	101.5	8091.4	18.3		
Average	149373.3			18.4	0.60	3.27
7	184592.0	102.5	8251.6	22.4		
8	177920.0	102.0	8171.3	21.8		
9	195712.0	102.5	8251.6	23.7		
Average	186074.7			22.6	1.00	4.40
10	137888.0	102.5	8251.6	16.7		
11	128992.0	102.0	8171.3	15.8		
12	130104.0	102.5	8251.6	15.8		
Average	132328.0			16.1	0.54	3.35
13	106752.0	102.5	8251.6	12.9		
14	98968.0	102.5	8251.6	12.0		
15	108976.0	102.5	8251.6	13.2		

Average	104898.7			12.7	0.64	5.01
16	139000.0	102.0	8171.3	17.0		
17	131216.0	102.0	8171.3	16.1		
18	122320.0	102.0	8171.3	15.0		
Average	130845.3			16.0	1.02	6.38
19	125656.0	102.5	8251.6	15.2		
20	118984.0	102.0	8171.3	14.6		
21	117872.0	102.0	8171.3	14.4		
Average	120837.3			14.7	0.43	2.92
22	142500.0	102.5	8251.6	17.3		
23	140750.0	102.0	8171.3	17.2		
24	133750.0	102.0	8171.3	16.4		
Average	139000.0			17.0	0.51	3.00
25	273000.0	151.0	17907.9	15.2		
26	259500.0	151.0	17907.9	14.5		
27	260500.0	151.0	17907.9	14.5		
Average	264333.3			14.8	0.42	2.85
28	131259.0	102.5	8251.6	15.9		
29	137500.0	102.0	8171.3	16.8		
30	129250.0	102.0	8171.3	15.8		
Average	132669.7			16.2	0.56	3.45

CONCRETE SLAB SPECIMENS

Table A-4 Concrete Slab Specimens

Specimen	Failure load (N)	Diameter (mm)	Area (mm^2)	f'_c (MPa)	SD	C.O.V (%)
1	369184.0	102.0	8171.3	45.2		
2	338048.0	102.0	8171.3	41.4		
3	346944.0	102.0	8171.3	42.5		
Average	351392.0			43.0	2.0	4.6
4	349168.0	100.5	7932.7	44.0		
52	333600.0	102.5	8251.6	40.4		

6	338048.0	102.0	8171.3	41.4		
Average	340272.0			41.9	1.9	4.4
7	326928.0	102.0	8171.3	40.0		
82	366960.0	102.0	8171.3	44.9		
9	345740.0	102.0	8171.3	42.3		
Average	346542.7			42.4	2.5	5.8
10	326928.0	102.0	8171.3	40.0		
11	366960.0	102.0	8171.3	44.9		
12	345740.0	102.0	8171.3	42.3		
Average	346542.7			42.4	2.5	5.8
13	394000.0	102.5	8251.6	47.7		
14	309000.0	102.5	8251.6	37.4		
15	403000.0	102.5	8251.6	48.8		
Average	368666.7			44.7	6.3	14.1
16	411000.0	102.0	8171.3	50.3		
17	391000.0	102.0	8171.3	47.9		
18	382000.0	102.5	8251.6	46.3		
Average	394666.7			48.1	2.0	4.2

CONCRETE FOUNDATION SPECIMENS

Table A-5 Concrete Foundation Specimens

Specimen	Failure load (N)	Diameter (mm)	Area (mm^2)	f'_c (MPa)	SD	C.O.V(%)
1	682768	151.5	18026.7	37.9		
2	762832	151.5	18026.7	42.3		
3	711680	151.5	18026.7	39.5		
Average	719093.3			39.9	2.2	5.6
4	333600	102.5	8251.6	40.4		
5	273552	102.0	8171.3	33.5		
6	366960	102.5	8251.6	44.5		
Average	324704			39.5	5.6	14.1
7	331376	102.0	8171.3	40.6		
8	329152	101.0	8011.8	41.1		

9	331376	102.5	8251.6	40.2		
Average	330634.7			40.6	0.5	1.1

MASONRY PRISM SPECIMENS

Table A-6 Masonry Prism Specimens

Prism	**f'_m (MPa)**	**Strain at Ultimate f'_m**	**E'_m (MPa)**
1a	21.40	1.97E-03	9489.91
1b	23.04	2.01E-03	11236.62
1c	21.83	2.00E-03	9769.90
Average	22.09	1.99E-03	10165.48
SD	0.85	2.08E-05	938.14
C.O.V (%)	3.85	1.04	9.23
Calculated f'_m	15.78		
2a	21.30	2.21E-03	8783.53
2b	24.50	2.29E-03	9765.12
2c	13.40	2.79E-03	4324.07
Average	19.73	2.43E-03	7624.24
SD	5.71	3.14E-04	2899.86
C.O.V (%)	29.0	12.94	38.03
Calculated f'_m	19.26		
3a	13.00	1.75E-03	8067.98
3b	20.80	2.05E-03	10319.27
3c	20.50	2.23E-03	8757.91
Average	18.10	2.01E-03	9048.39
SD	4.42	2.42E-04	1153.41
C.O.V (%)	24.4	12.06	12.75
Calculated f'_m	17.70		
4a	22.46	2.22E-03	8607.42
4b	19.62	2.00E-03	11477.35
4c	NA	NA	NA
Average	21.04	2.11E-03	10042.38
SD	2.01	1.56E-04	2029.35
C.O.V (%)	9.5	7.37	20.21

Calculated f'_m	20.89		
5a	20.30	2.08E-03	12668.94
5b	22.65	2.08E-03	12644.21
5c	21.82	1.96E-03	12662.31
Average	21.59	2.04E-03	12658.49
SD	1.19	6.93E-05	12.80
C.O.V (%)	5.5	3.40	0.10
Calculated f'_m	21.50		
6a	15.72	1.94E-03	6727.94
6b	15.73	1.89E-03	7444.05
6c	8.33	3.83E-03	8562.34
Average	13.26	2.55E-03	7578.11
SD	4.27	1.11E-03	924.52
C.O.V (%)	32.2	43.31	12.20
Calculated f'_m	12.73		
7a	20.22	2.10E-03	9752.88
7b	18.90	1.90E-03	11940.48
7c	21.23	2.10E-03	17288.23
Average	20.12	2.03E-03	12993.86
SD	1.17	1.15E-04	3876.55
C.O.V (%)	5.8	5.68	29.83
Calculated f'_m	20.02		
8a	16.90	1.84E-03	11366.21
8b	18.98	2.10E-03	11398.08
8c	20.30	2.00E-03	13964.95
Average	18.73	1.98E-03	12243.08
SD	1.72	1.31E-04	1491.27
C.O.V (%)	9.2	6.62	12.18
Calculated f'_m	18.58		

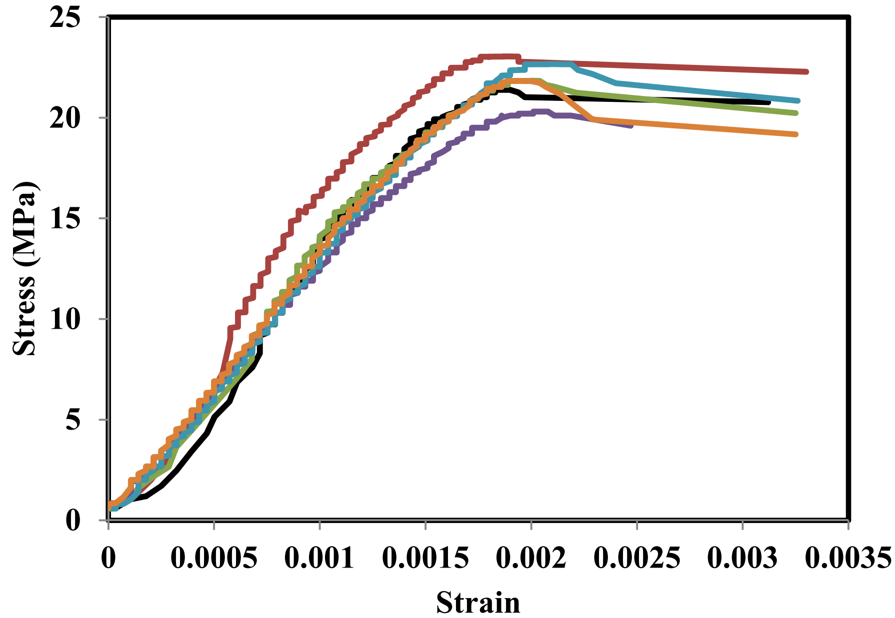

Fig. A-1. Stress-strain relationship for masonry prism samples

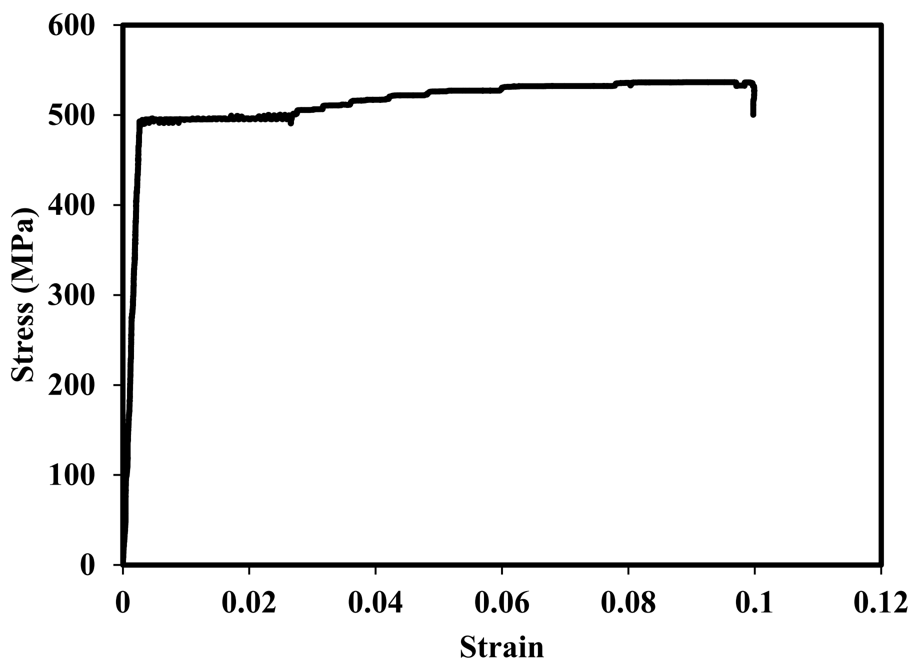

Fig. A-2. Stress-strain relationship for D7 reinforcement

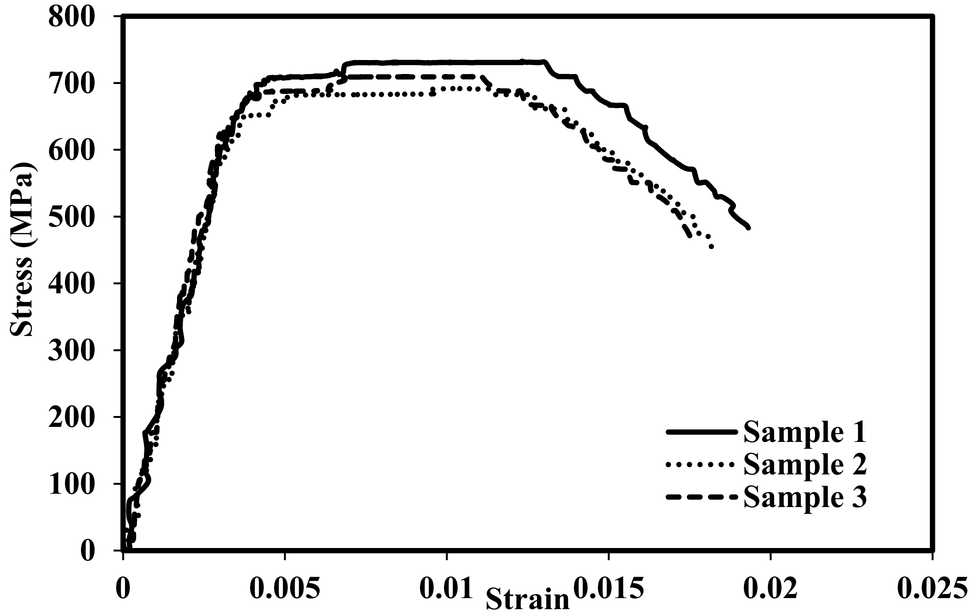

Fig. A-3. Stress-strain relationship for W1.7 smooth bars

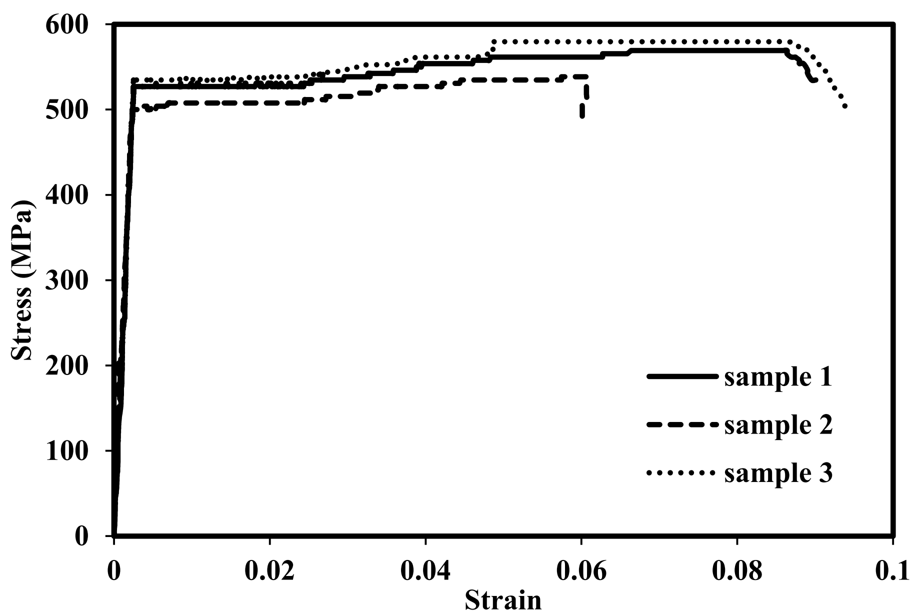

Fig. A-4. Stress-strain relationship for D4 deformed bars

APPENDIX B: WALL REINFORCEMENT DETAILS

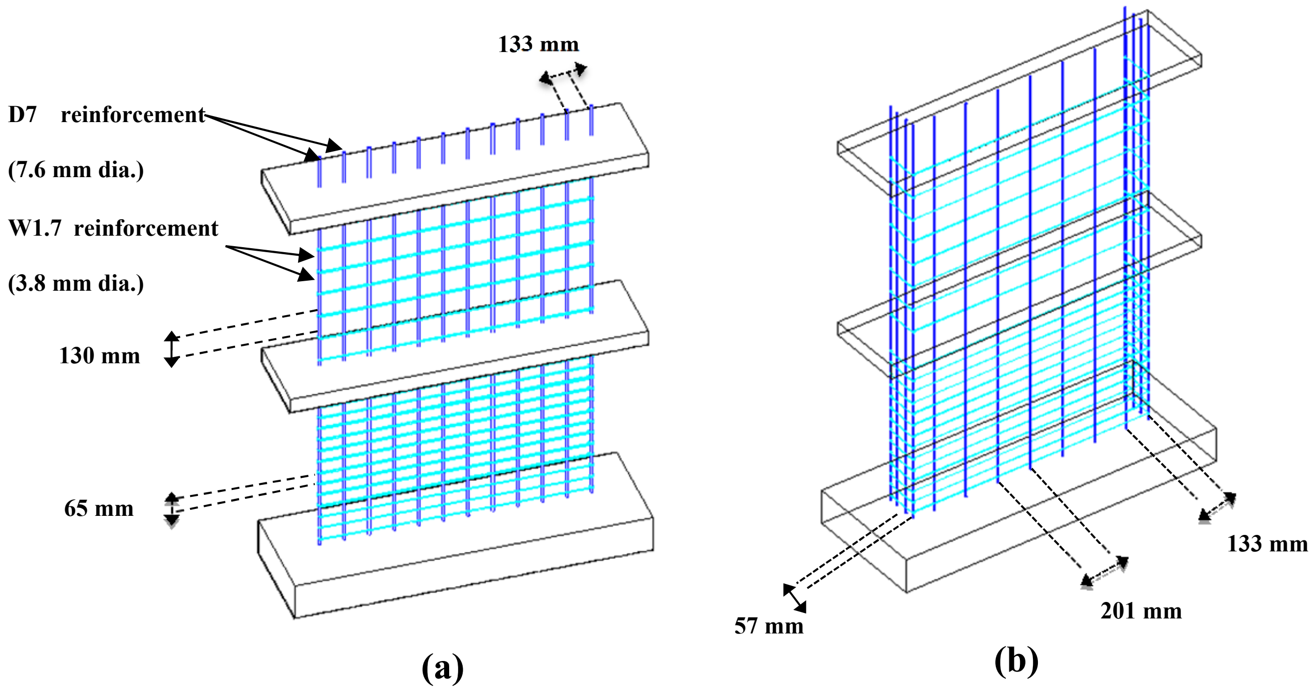

Fig. B-1 Reinforcement details: (a) Rectangular and slab-coupled walls; (b) Flanged wall

APPENDIX C: SLAB REINFORCEMENT DETAILS

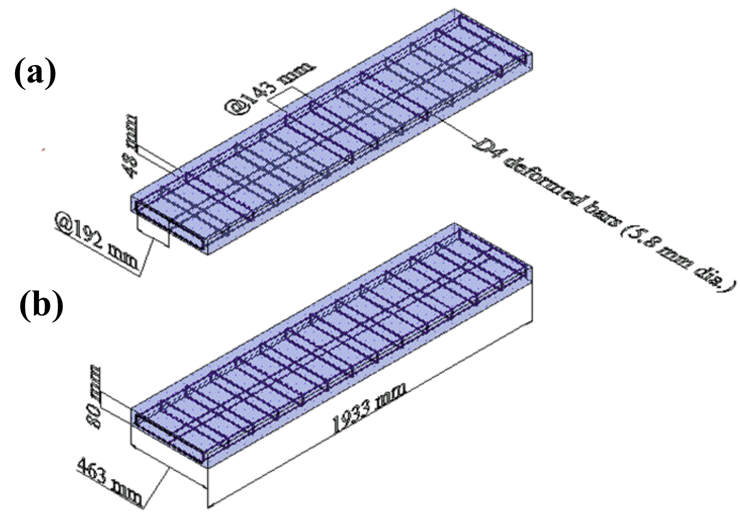

Fig. C-1 Slab detailing: reinforcement spacing; (b) slab dimensions

APPENDIX D: TEST SETUP MODIFICATION FOR SLAB-COUPLED WALLS

Slight modifications were done for testing slab-coupled walls. Specifically, a special fabricated loading beam was designed to allow rotation of the walls without imposing additional capacity into it (See Fig. D-1a,b,c). Moreover, as shown in Fig. D-1d, more instrumentation was provided in these walls because of their nature.

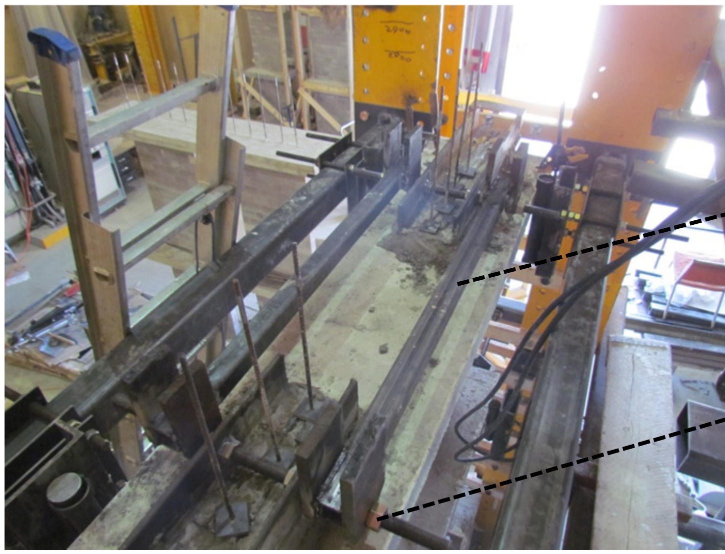

(a)

(b)

(c)

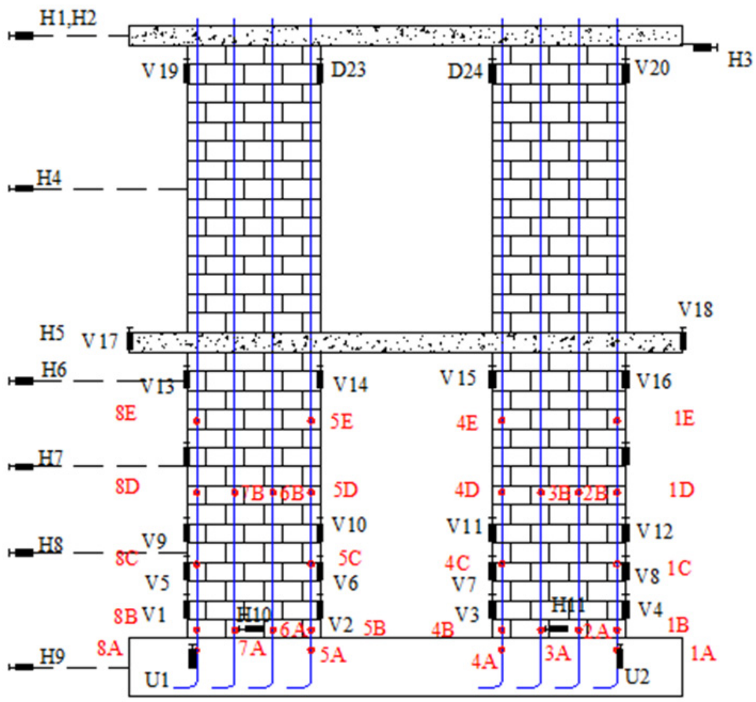

(d)

Fig. D-1 Special consideration for slab-coupled Walls: Fabricated loading beam for slab-coupled walls; (a) Isometric view; (b) Top view; (c) loading beam only (d) Internal and external instrumentation

APPENDIX E: MOMENT CAPACITY CALCULATIONS FOR THE WALLS

Formulation used to predict the walls' yield strengths:

$$P = C_m + C_s + T$$

$$C_m = 0.5\varepsilon_m E_m tc$$

$$C_s = \sum A_s' f_s$$

$$T = \sum A_s f_s$$

$$\varepsilon_m = \frac{\varepsilon_y \times c}{d - c}$$

$$M_y = C_m\left(0.5l_w - \frac{1}{3}c\right) + \sum A_s f_s \left(d_i - 0.5l_w\right) + \sum A_s' f_s \left(0.5l_w - d_i\right)$$

$$V_y = \frac{M_y}{h_w}$$

P = axial load on the wall (kN)
C_m = compressive force of masonry (kN)
C_s = compressive force of compressive steel (kN)
T = tensile force of tension steel (kN)
ε_m = masonry strain
ε_y = yield strain of tensile reinforcement
E_m = elastic modulus of masonry taken as 850 f'_m (MPa)
t = thickness of shear wall (mm)
c = neutral axis depth from compression face (mm)
d_i = distance of corresponding bars i from compression face (mm)
A_s = cross-sectional area of tensile reinforcement (mm^2)
A'_s = cross-sectional area of compression reinforcement (mm^2)
f_s = yield strength of steel reinforcement (MPa)
M_y = yield moment capacity of the wall (kN.m)
V_y = yield lateral load capacity (kN)

Formulation used to predict the walls' ultimate strengths:

$$P = C_m + T$$

$$C_m = 0.85 f_m^{'} t \beta_1 c$$

$$T = \sum A_s f_s$$

$$M_u = C_m \left(0.5 l_w - 0.5 \beta_1 c\right) + \sum A_s f_s \left(d_i - 0.5 l_w\right)$$

$$V_u = \frac{M_u}{h_w}$$

f'_m = compressive strength of masonry (MPa)
β_1 = ratio of depth of compression to depth of neutral axis
M_u = ultimate moment capacity of the wall (kN.m)
V_u = ultimate lateral load capacity (kN)

APPENDIX F: SAMPLE CALCULATION S FOR YIELD AND ULTIMATE CURVATURES

Wall W1 (Rectangular):

Yield curvature:

$$\phi_{y,th1} = \varepsilon_{sy} \big/ (d - c_y)$$

$$\phi_{y,th1} = \frac{0.0025}{1501.23 - 230.91}$$

$$\phi_{y,th1} = 2.147 \times 10^{-6} \text{ rad/mm}$$

Ultimate curvature:

$$\phi_{u,th1} = \varepsilon_u \big/ c_u$$

$$\phi_{u,th1} = \frac{0.0025}{230.91}$$

$$\phi_{u,th1} = 10.82 \times 10^{-6} \text{ rad/mm}$$

Wall W3 (Slab-coupled):

$$\phi_{th1,cw} = \frac{\phi_{y,u}}{1 - DOC}$$

Where $\phi_{y,u}$ denotes yield and ultimate curvatures of individual walls W5 as calculated above, respectively.

Yield curvature:

$$\phi_{yth1,cw} = \frac{5.85 \times 10^{-6}}{1 - 0.51}$$

$$\phi_{yth1,cw} = 11.93 \times 10^{-6} \text{ rad/mm}$$

Ultimate curvature:

$$\phi_{uth1,cw} = \frac{28.2\times10^{-6}}{1-0.51}$$

$$\phi_{uth1,cw} = 57.6\times10^{-6}\ \text{rad/mm}$$

Appendix G: Flow Chart Of Modelling Process To Conduct IDA

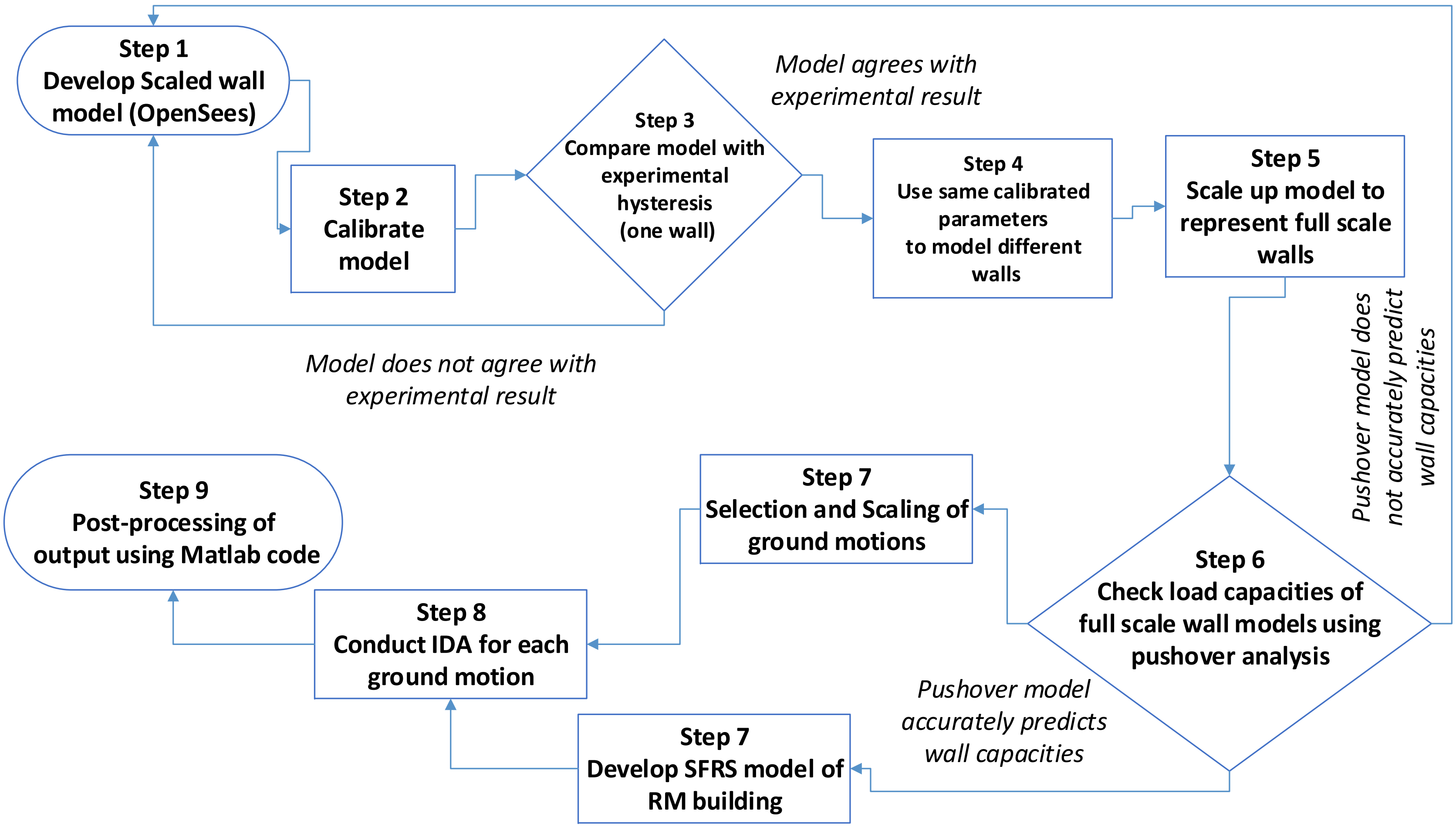

APPENDIX H: MATERIAL MODELS USED TO CALIBRATE SCALED WALL MODELS:

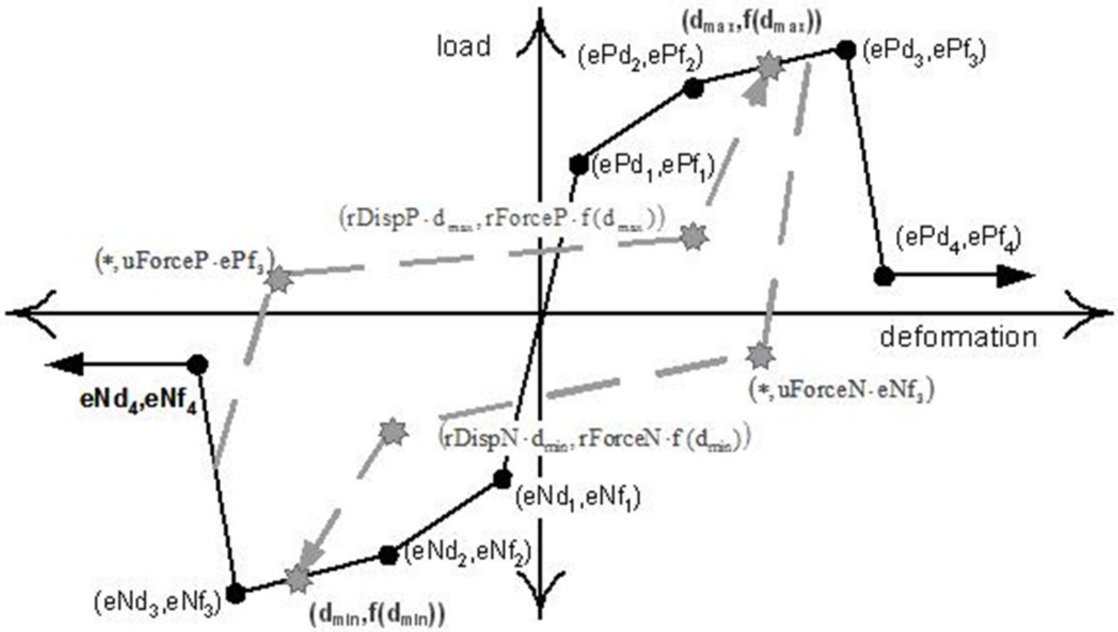

Fig. H-1 Pinching 4 material model (McKenna et al. 2000)

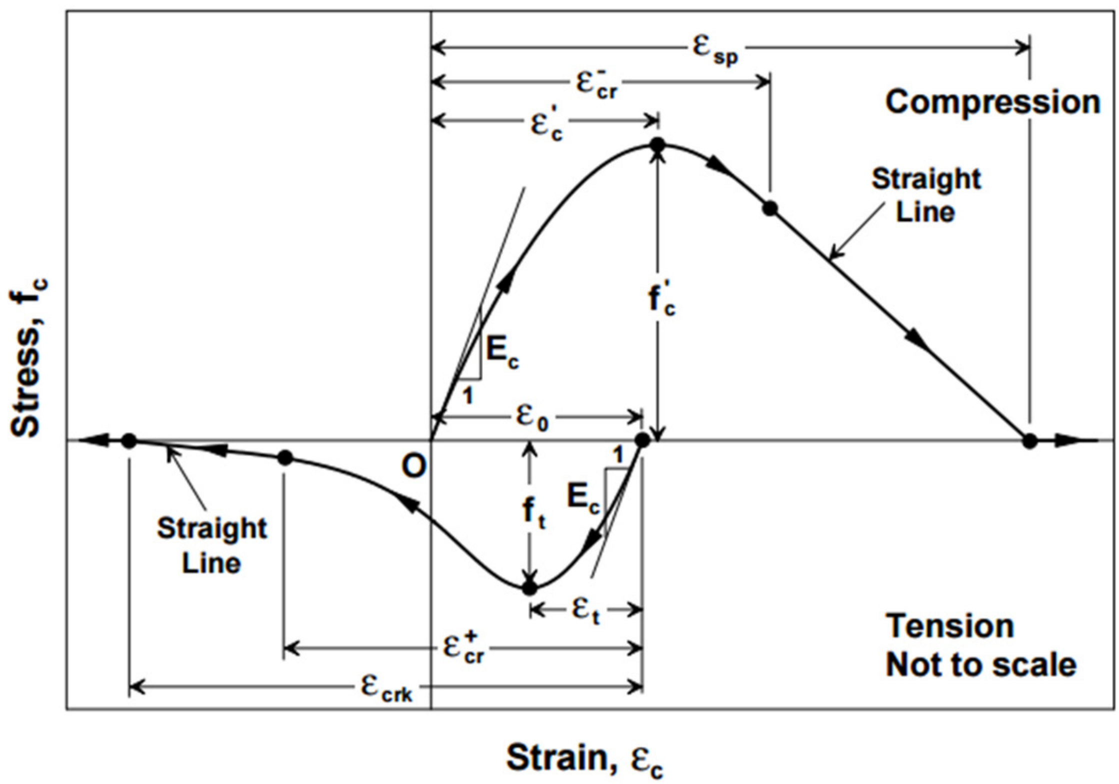

Fig. H-2 Compression and tension envelopes of Chang and Mander 1994 model (Orakcal et al. 2006)

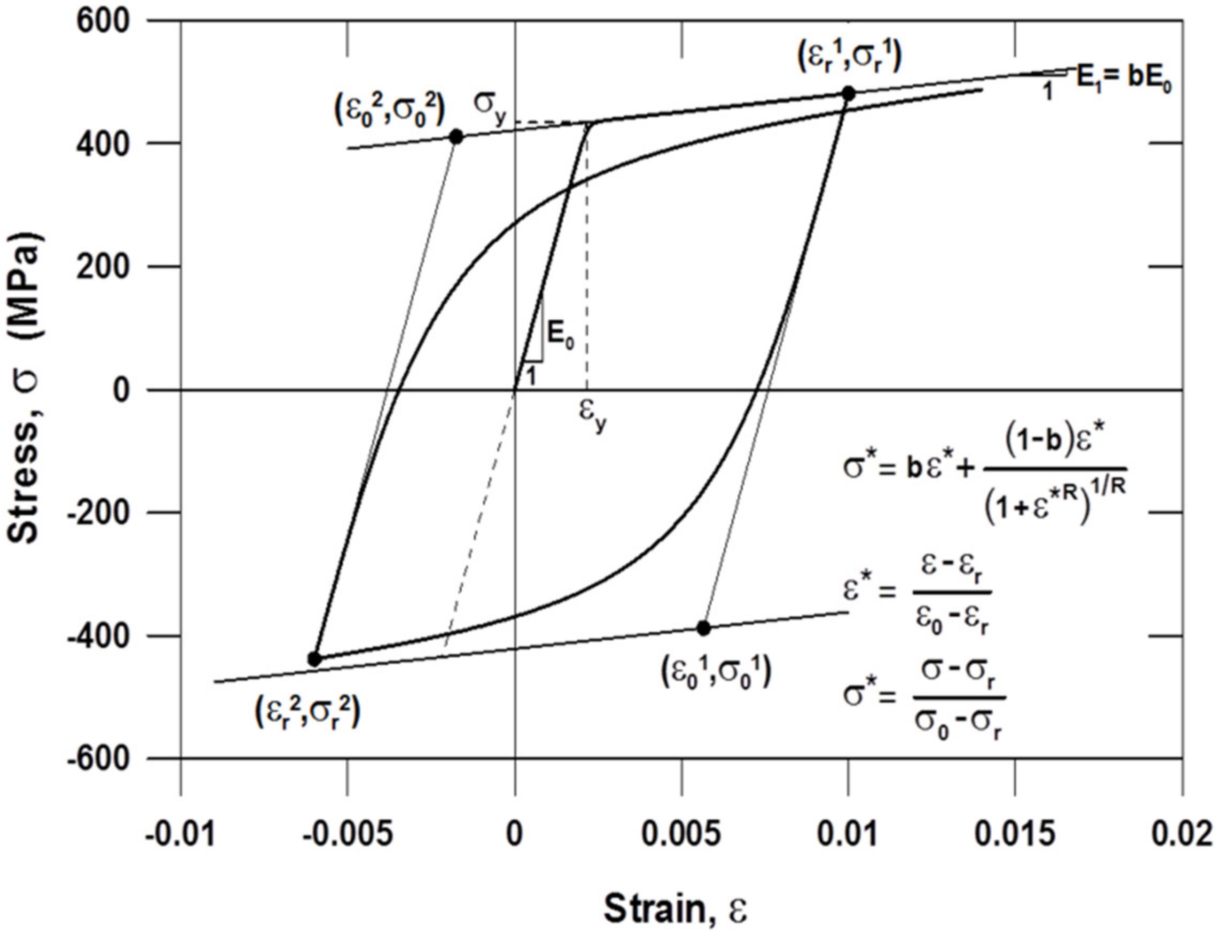

Fig. H-3 Constitutive model of steel (Menegotto and Pinto, 1973)

APPENDIX I: INCREMENTAL DYNAMIC ANALYSIS RESULTS

Table I-1 Incremental Dynamic Analysis Result for 30 Ground Motions

***IM* (g)**	**SF**	**West Vancouver Earthquakes**																										
		West 1	**West 2**	**West 4**	**West 5**	**West 7**	**West 8**	**West 10**	**West 11**	**West 13**	**West 14**	**West 16**	**West 17**	**West 19**	**West 20**	**West 22**	**West 23**	**West 25**	**West 26**	**west 28**	**west 29**	**West 31**	**West 32**	**West 34**	**West 35**	**West 37**	**West 38**	**We 40**
0.0	0.0	0.0	0.0	0.0	0.0	0.0	0.0	0.0	0.0	0.0	0.0	0.0	0.0	0.0	0.0	0.0	0.0	0.0	0.0	0.0	0.0	0.0	0.0	0.0	0.0	0.0	0.0	0.
0.7	1.0	0.2	0.2	0.3	0.3	0.2	0.2	0.3	0.2	0.2	0.2	0.4	0.2	0.3	0.2	0.2	0.2	0.1	0.2	0.1	0.2	0.2	0.2	0.2	0.2	0.2	0.2	0.
1.0	1.5	0.4	0.3	0.4	0.4	0.5	0.2	0.8	0.4	0.3	0.4	0.5	0.8	0.4	0.4	0.5	0.3	0.2	0.3	0.2	0.3	0.4	0.3	0.5	0.4	0.4	0.3	0.
1.3	2.0	1.1	0.4	0.5	0.8	1.1	0.6	0.9	0.7	0.6	0.7	0.7	1.3	0.6	0.6	0.7	0.4	0.2	0.7	0.3	0.3	0.4	0.4	0.6	0.4	0.3	0.4	0.
1.6	2.5	1.4	0.4	0.7	1.5	1.5	1.8	1.1	0.9	0.9	1.3	0.9	1.3	0.8	0.9	1.1	0.5	0.3	0.7	0.6	0.4	0.5	0.6	0.9	1.0	0.7	0.6	0.
2.0	3.0	1.6	0.4	0.9	2.1	2.2	3.4	1.9	1.2	1.1	2.0	1.6	1.5	1.3	1.2	1.3	0.6	0.5	0.8	0.9	0.5	0.7	1.0	1.9	1.5	1.0	1.7	1.
2.3	3.5	1.7	0.6	1.0	0.2	2.1	4.8	2.5	1.5	0.9	2.1	0.4	2.7	1.6	1.3	3.2	0.9	0.8	0.9	1.1	0.6	1.4	1.0	3.4	1.4	1.3	3.1	1.
2.6	4.0	1.9	1.0	1.1	2.3	3.9	5.4	2.7	1.9	1.2	2.3	2.4	3.0	2.1	2.5	5.0	1.4	1.5	1.4	1.3	1.4	1.1	1.4	5.4	3.2	2.3	4.1	2.
2.9	4.5	1.9	2.0	1.6	3.0	3.8	5.5	4.8	5.0	2.6	1.8	3.0	3.7	2.1	3.2	3.0	1.8	2.0	0.4	1.7	2.2	2.7	2.0	6.0	6.0	3.6	6.2	2.
3.3	5.0	2.3	3.7	2.2	4.0	2.9	5.5	3.6	2.8	2.9	2.1	3.4	4.5	4.0	4.7	4.0	1.4	3.4	0.5	1.6	2.6	3.1	2.9	8.9	0.4	4.6	7.7	3.
3.6	5.5	2.5	4.3	3.1	4.2	3.9	5.6	4.2	3.2	3.3	2.5	4.0	6.0	2.6	4.8	4.9	2.5	4.6	2.4	2.8	3.4	2.9	3.8	9.4	6.1	5.2	8.7	3.

APPENDIX J: SPECTRAL SHAPE FACTOR TABLE FROM FEMA P-695 (ATC 2009B)

Table J-1 SSF Factors for Different Ductility levels and Fundamental Period, *T*

T (seconds)	Period-Based Ductility (μ_T)							
	1	1.1	1.5	2	3	4	6	≥ 8
≤ 0.5	1.00	1.05	1.1	1.13	1.18	1.22	1.28	1.33
0.6	1.00	1.05	1.11	1.14	1.2	1.24	1.3	1.36
0.7	1.00	1.06	1.11	1.15	1.21	1.25	1.32	1.38
0.8	1.00	1.06	1.12	1.16	1.22	1.27	1.35	1.41
0.9	1.00	1.06	1.13	1.17	1.24	1.29	1.37	1.44
1	1.00	1.07	1.13	1.18	1.25	1.31	1.39	1.46
1.1	1.00	1.07	1.14	1.19	1.27	1.32	1.41	1.49
1.2	1.00	1.07	1.15	1.2	1.28	1.34	1.44	1.52
1.3	1.00	1.08	1.16	1.21	1.29	1.36	1.46	1.55
1.4	1.00	1.08	1.16	1.22	1.31	1.38	1.49	1.58
≥ 1.5	1.00	1.08	1.17	1.23	1.32	1.4	1.51	1.61